Numerical simulation of three-dimensional viscous flow around marine structures

Kjetil K. Heggernes

Dr.ing.-thesis

NTNU
Department of Marine Technology

Trondheim, September 2005

Contents

Acknowledgements

This thesis is submitted as one of the requirements for the *Doktor ingeniør* degree at The Norwegian University of Science and Technology (NTNU) in Trondheim. The work has been carried out as part of the Strategic University Program in Computational Science and Engineering (CSE) at NTNU, financed by The Research Council of Norway (NFR).

First, I would like to thank my supervisors, professor Bjørnar Pettersen (Department of Marine Technology, NTNU) and senior scientists Trond Kvamsdal and Karstein Sørli (SINTEF Applied Mathematics), for their guidance and support throughout this work. Their technical know-how and experience have been great assets in this doctoral project.

Next, I want to thank dr.ing. Jens Holmen for his technical support on the VISTA code. Without his help, the completion of this thesis would not have been possible. Also, thanks to Vegard Eide and the people at ITEA for their help with various supercomputing issues.

Further, it should be mentioned that Norsk Hydro Production provided access to experimental data, which are crucial to the thesis work. Their cooperation is highly appreciated.

Last but not least, I would like to thank my wife Mona for all her encouragement and unconditional support, and for always believing in me. I could not have carried it through without her.

Introduction

0.1 Background and motivation

Computational marine hydrodynamics is a multidisciplinary field of research. It resides at the intersection between marine engineering, fluid dynamics, numerical analysis and computer science. Researchers from many different communities are involved, all bringing their special knowledge, language, traditions and biases to the scene. Each of the afore-mentioned disciplines have their own major conferences, journals and text books. Consequently, it can be a challenging task to get an updated overview of all relevant sources of information. With that in mind, a logical starting point for the current study is to look into recent proceedings of the most important conferences in marine engineering and hydrodynamics. One of them is the biennial *Symposium on Naval Hydrodynamics*, headed by the *Office of Naval Reseach* (ONR). Here we get an indication of what's state of the art in marine hydrodynamics, and a flavour of the wide variety of topics covered. Another example is the annual *International Conference on Offshore Mechanics and Arctic Engineering* (OMAE), headed by *The American Society of Mechanical Engineers* (ASME). Studying the proceedings of cornerstone conferences gives a good overview of the research activity within different areas.

The challenges in the field of computational marine hydrodynamics may be divided into two main categories: (1): Ship flow problems, (2): Offshore flow problems. Two main features set ship flow problems apart from other marine flow problems: (1) The geometry, and (2) the forward speed. The forward speed creates a complex wave system which puts special demands on the computational method. Also, the Reynolds number is generally very high. Flow around a ship without forward speed (subject to waves and/or current), may be viewed as an offshore problem according to the previous definition.

A short review of the two main types of problems will be given in the following.

0.1.1 Ship flow problems

Within the field of computational marine hydrodynamics, ship flow problems have always been an important driving force, putting heavy demand on both numerical methods and hardware resources. A recent, comprehensive treatment of viscous ship flow problems can be found in the proceedings of the *Gothenburg 2000 workshop on numerical ship hydrodynamics* [1]. At this workshop, three different ship models of displacement type were used as test cases, each with a particular focus area: Stern flow prediction of a full ship form, propeller/hull interaction, and the wave field of a transom stern hull, respectively. Apart from the usual discussion of methods and results, a major issue at the workshop was verification and validation of computer codes, demonstrating the need for good quality experimental data when doing pioneering flow calculations. All in all, the Gothenburg 2000 workshop gives a good picture of the CFD (Computational Fluid Dynamics) capabilities of the ship hydrodynamics community, as well as revealing some of the weaknesses.

Accurate prediction of a ship's power requirement is of great importance when planning a new vessel. Shipbuilders, shipowners and military governments have always depended on time consuming and expensive towing tank experiments in order to get their resistance and propulsion data. As a consequence, the calm water forward speed case is by far the most studied in ship hydrodynamics. The possibility of getting accurate resistance predictions quickly and at a low cost using computers has been a strong driving force behind numerical ship hydrodynamics research since the beginning. The "numerical towing tank" concept clearly illustrates the vision of replacing real towing tanks by virtual ones. However, the view of CFD as complementing rather than replacing traditional experiments is more realistic in the foreseeable future. The numerical towing tank has a long way to go before it can predict a ship's resistance with the same accuracy as the world's leading experimental facilities. On the other hand, CFD can provide detailed information about the flow field which can't be measured in experiments.

Some detailed historical reviews, analyses of the present state and future prospects in numerical ship hydrodynamics can be found in [2], [3] and [4]. The development of numerical methods for solving the ship resistance problem is greatly influenced by experimental traditions. The pioneers in numerical ship hydrodynamics realized that the well established practice of subdividing a ship's resistance in a viscous and a wavemaking part lent itself well to a new computational approach. One of the first to solve the ship wave problem by means of a numerical computer code was C. Dawson in 1977 [5]. He modeled the flow with the assumption of inviscid (or ideal) fluid, using potential theory with a linear free surface boundary condition.

His solution is a modification of a source technique developed for arbitrary 3D bodies in infinite ideal fluid by Hess and Smith in 1962 [6]. Still, the viscous part had to be computed by means of empirical formulae, such as the ITTC-57 correlation line. Dawsons method has later been improved with exact, nonlinear boundary conditions. Similar methods are also extended to include ship motions. Computer programs based on potential flow are widely used in industry today. The methods generally give good results for surface elevation, wave resistance and seakeeping characteristics, and many other flow problem in which viscous effects are small. They are very computationally efficient compared to codes solving the full Navier-Stokes equation. Used with some care, a potential flow code is a powerful tool in ship design optimization problems, e.g. when studying details like the bow shape's influence on the wavemaking. However, potential theory fails to predict the flow near the stern, where strong vorticity and massive separation are important flow features. So, in order to get detailed information about the flow into the propeller plane, calculate viscous resistance, determine the manoeuvering characteristics, or solve a whole range of other marine engineering problems, we have to include viscosity in our physical model.

0.1.2 Offshore flow problems

Any case of flow around a marine structure which isn't a ship can be categorized as an offshore flow problem. This collective term covers a wide variety of cases. Oil drilling platforms, fixed or floating, are common examples. As mentioned above, a ship without forward speed may also fall into the same category. A review of the diversity of challenges within the field of both ship and offshore flow problems can be found in Faltinsen [7].

The main objective in computational marine hydrodynamics is to determine the motions and structural response caused by the hydrodynamic forces. The information provided from computations is invaluable when evaluating new designs with regards to safety and operability in different conditions. In many flow problems, viscous effects are small or negligible. A common example is the flow around a large structure in waves at zero forward speed. In such cases, computational methods based on potential theory give good results. Three-dimensional source techniques originally developed for the aerospace industry (e.g Hess & Smith [6]) are combined with complex Green's functions which account for the surface waves (similar to Dawson's ship wave solution [5]). Such methods have been used since the early 1970s. Today, computer codes based on these methods are industry standard for solving wave response problems. An early example of the application of the 3D source technique can be found in a paper due to Faltinsen and Michelsen [8].

The grand challenges of present day computational marine hydrodynamics are found in problems where viscous effects play an important role. A problem in this category which receives a lot of attention is vortex induced vibrations (VIV) of slender marine structures. Examples of slender marine structures are flexible risers, tendons of tension leg platforms and free spanning pipelines. Steady current past the cylindrical structures causes vortex shedding, which leads to oscillating pressure forces on the structures. These forces can cause resonance, which may in turn lead to large motions. In the case of systems of flexible risers, the motions can result in collisions between individual risers, often causing structural damage or failure. The dynamic behaviour of slender structures subject to VIV is very complicated, and is not yet fully understood. In order to reproduce this behaviour in numerical simulations, the fluid flow problem and the structural response problem must be solved simultaneously. This approach is known as FSI, or Fluid-Structure Interaction. Three-dimensional numerical simulations of flow around very high aspect ratio cylinders at realistic Reynolds numbers are not feasible even on today's most powerful computers. Consequently, two-dimensional approximations have been employed to calculate the response of risers in cross flow, such as the strip theory (Herfjord et al [9]). Also, "quasi-3D" extensions to the strip theory have been used, to account for spanwise variation (shearing) of the current velocity profile (Willden & Graham [10]). However, the true three-dimensionality of the flow around the cylinder may be an important factor influencing the VIV dynamics. Also, turbulence come into play at realistic Reynolds numbers. In conclusion, VIV of slender marine structures is a challenging area of research with many unsolved problems, some of which are addressed in the present study.

0.2 Outline of the present work

The present study is part of the Strategic University Program in Computational Science and Engineering (CSE) at NTNU, as one of nine doctoral projects. The objectives of the CSE program are threefold:

1. To improve the national level of competence to utilise mathematics and computer science in engineering.

2. To improve the competitiveness of Norwegian marine related industry.

3. To improve NTNU's role and position in a national collaboration on scientific computing.

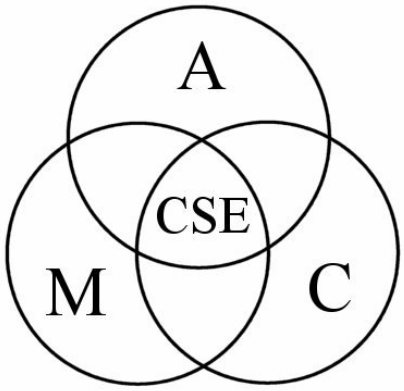

Figure 1: The MAC model

The CSE program uses the so-called MAC model as a conceptual framework, see figure 1. The three circles represent Mathematical modeling, Application and Computer science, respectively. Computational science and engineering resides in the centre. In the present study, main emphasis is put on the application part of the MAC model.

The first part of the thesis covers the theoretical backgrond for computational fluid dynamics; specifically, the incompressible Navier-Stokes equations. Some general solution methods are reviewed, as well as the most common discretization techniques, which form the basis of modern CFD codes.

The second part is a report of a series of numerical experiments, including a short description of the computational method applied in the Navier-Stokes solver. The following flow cases are computed:

- Laminar flow around a fixed, three-dimensional circular cylinder at a Reynolds number $Re = u_\infty d/\nu = 265$. Different cylinder lengths are tested. The onset of three-dimensionality in the wake flow is given particular attention. The sensitivity to time step and grid refinement is investigated.

- Subcritical turbulent flow around a cylinder at $Re = 3900$. The turbulence is modelled using large-eddy simulation (LES). The effects of using wall damping and different time integration schemes are investigated.

- Turbulent flow around two fixed circular cylinders arranged in tandem at $Re = 21600$. This test case is a model problem for flow around

marine risers. Drag and lift on the two cylinders are compared with experimental data; both mean values and standard deviation.

- Laminar cross flow around a 6:1 ellipsoid at $Re = 100$. An initial calculation of this case is presented, showing the potential of the numerical method for other marine applications. The 6:1 ellipsoid is a standard model problem for a submarine.

- Laminar flow around a sphere at $Re = 300$. This is a generalized case of flow around bluff bodies, studied by many researchers. An initial calculation is performed.

The three first cases can be seen as steps towards the VIV problem, taking a bottom-up approach. A logical next step could be, for example, adding forced motion to the downstream cylinder in the tandem case. In all the flow simulations performed in this thesis work, we have aimed for *high fidelity*, obtaining a higher level of accuracy than in most engineering calculations. Computational tools currently under development at SINTEF Applied Mathematics in collaboration with NTNU have been used. These tools include a Navier-Stokes solver (VISTA, ref. chapter 3) and a grid generator (Griddler, ref. section 4.2.2).

The simulations are performed using NTNU's High Performance Computing (HPC) facilities [11], two SGI Origin 3800 machines with 896 processors combined, a total memory of 816 GB and a total peak performance of 998 Gflops. Most of the simulations are run on 32-96 processors, depending on the problem size. The total time needed to simulate a sufficiently long time series range from 1-3 days for the laminar cases to a couple of weeks in the largest turbulent cases. Here, the "total time" also incudes periods when the jobs are pending or suspended due to higher priority jobs. The figures are included to give an indication of the quite substantial computational work involved.

Part I

Theoretical background

Chapter 1

Incompressible Navier-Stokes Equation

The equations which today are known as *Navier-Stokes relations* were in fact derived by 5 different 19th century mathematicians: The four Frenchmen *Navier* (1822), *Cauchy* (1828), *Poisson* (1829) and *Saint-Venant* (1843); and the Englishman *Stokes* in 1845. This was generally done by modifying the equations of frictionless fluid motion, derived by *Leonard Euler* in 1755. The first one, *C.M.L.H. Navier*, arrived at the correct form of the equations, however, his physical reasoning was not quite accurate. This may be why the equations was not generally accepted by other scientists at that time. According to Anderson [17], *A.J.C.B de Saint-Venant* was the first one who correctly modeled the physics, identifying the internal viscous stresses and their relation to the velocity gradients. He also introduced the coefficient of viscosity for the first time. Curiously, his name never became associated with these equations, even if he published his results two years before *G.H. Stokes*.

This chapter is intended as a brief introduction to the theory of computational fluid dynamics (CFD), so the actual derivation of the Navier-Stokes equations will not be shown here. Focus will be on the physical interpretation of the equations. Details of the deduction of the Navier-Stokes equations as we know them today can be found in many text books, e.g. White [12] [13] and Schlichting [14].

1.1 Conservation laws. Governing equations

The traditional way of describing fluid flow is by *laws of conservation*. Such laws are fundamental, and apply to all physical systems. The number of con-

servation laws needed to describe a particular flow situation depend upon the physical and/or chemical complexity of the flow. In that respect, hydrodynamic flow is quite simple: We only consider (sea-)water, a newtonian fluid (linear relation between stress and rate of strain) of uniform, homogeneous composition, without any diffusion of species, chemical reactions or electromagnetic effects. This class of flows can be described by the three most basic conservation laws:

1. Conservation of mass (continuity)

2. Conservation of momentum (Newton's second law)

3. Conservation of energy (first law of thermodynamics)

In order to obtain the governing equations, we apply these conservation laws to an enclosed region of the flow, called a *control volume* (*CV*). The CV may be of finite size or infinitesimally small; it may be fixed in space or moving with the fluid. An infinitesimally small control volume becomes a *differential volume* dV in the mathematical sense. The choice of control volume determines the form of the governing equations: integral or differential, conservative or non-conservative form. The four combinations are shown in table 1.1.

Physically and mathematically, the different forms of the equations are equivalent. Through manipulation of the equations, one form may be obtained from the other. However, when solving the equations numerically, the choice of form becomes important. To illustrate the basic concepts of CFD, the differential form of the equations is chosen as the starting point. Both the conservative (fixed CV) and non-conservative (moving CV) forms are stated. The integral form will be discussed briefly in relation to the finite volume method (see section 2.2.2).

The law of *mass conservation* assures *continuity* of fluid. We cannot have fluid accumulation, nor can there be voids anywhere in the fluid. The resulting *continuity equation* on differential, non-conservative form can be

CV size	Fixed in space	Moving with fluid
Finite sized	IE, conservative	IE, non-conservative
Infinitesimally small	PDE, conservative	PDE, non-conservative

Table 1.1: Four different versions of the control volume give different forms of the governing equations. (IE: integral equation, PDE: partial differential equation).

written as follows (in vector notation):

$$\frac{D\rho}{Dt} + \rho\boldsymbol{\nabla}\cdot\mathbf{u} = 0 \tag{1.1}$$

where ρ is the fluid density. The particle or substantial derivative is defined as

$$\frac{D}{Dt}() = \frac{\partial}{\partial t}() + (\mathbf{u}\cdot\boldsymbol{\nabla})() \tag{1.2}$$

Here, $\mathbf{u} = (u,v,w)$ is the velocity vector, and $\boldsymbol{\nabla}$ the vector differential operator. The substantial derivative is used when we follow a fluid element moving with the flow. Replacing the substantial derivative in equation 1.1 with the r.h.s of 1.2 gives the conservative form of the continuity equation:

$$\frac{\partial\rho}{\partial t} + \boldsymbol{\nabla}\cdot(\rho\mathbf{u}) = 0 \tag{1.3}$$

For the hydrodynamic flows of interest here, the *Mach number* $M = u/c$ is small, i.e. the flow velocities u are small compared to the speed of sound in water, c. According to White [13], we can assume the flow to be *incompressible* when $M < 0.3$, which is certainly the case in most marine applications (*slamming* being an important exception). Incompressibility implies that the density is constant. Consequently, $\frac{D\rho}{Dt} = 0$, and the continuity equation may be written

$$\boldsymbol{\nabla}\cdot\mathbf{u} = 0 \tag{1.4}$$

This simplification has important implications both physically and numerically, as we shall see later. A thorough treatment of incompressible flow as well as fluid dynamics in general can be found in Panton [19].

Conservation of momentum expresses the relation between applied force and resulting acceleration of a particle system, which is the same as applying Newton's second law to a fluid particle (or volume). The mathematical statement of Newtons second law in fluid dynamics constitutes *Navier-Stokes equation*:

$$\frac{D\mathbf{u}}{Dt} = \boldsymbol{\nabla}\cdot\boldsymbol{\sigma} + \mathbf{f} \quad\Longleftrightarrow\quad \frac{\partial\mathbf{u}}{\partial t} + (\mathbf{u}\cdot\boldsymbol{\nabla})\mathbf{u} = \boldsymbol{\nabla}\cdot\boldsymbol{\sigma} + \mathbf{f} \tag{1.5}$$

Equation 1.5 is the *stress-strain formulation* of the Navier-Stokes equation. In marine hydrodynamics, the external body force $\mathbf{f}$ commonly accounts for gravity, but may also include other forces, e.g inertia forces due to a rotating coordinate system. The stress tensor $\boldsymbol{\sigma}$ is given by

$$\sigma_{ij} = -p\delta_{ij} + 2\nu S_{ij} \tag{1.6}$$

where p is the kinematic pressure (i.e. pressure divided by density), δ_{ij} the Kronecker delta function, and $\nu = \mu/\rho$ the kinematic viscosity. (The kinematic pressure will be used in the following, unless stated otherwise). The components of the rate of strain tensor $\mathbf{S}$ is commonly written as

$$S_{ij} = \frac{1}{2}(\frac{\partial u_i}{\partial x_j} + \frac{\partial u_j}{\partial x_i}) \tag{1.7}$$

Note that only the shear deformations is present in $\mathbf{S}$, because the terms related to normal deformation (through the *bulk viscosity* λ) vanish when we use the incompressibility assumption. Equation 1.5 is also referred to as the *momentum transport equation* or the *unsteady advection-diffusion equation* in literature, among other terms.

Conservation of energy is also known as the *first law of thermodynamics*. It implies that the increase of energy of a system equals the sum of work and heat added to the system. The energy equation can be written:

$$\frac{D(\rho c_p T)}{Dt} = \varepsilon + \boldsymbol{\nabla} \cdot (k \boldsymbol{\nabla} T) \tag{1.8}$$

Here, T is the temperature, c_p the heat capacity, ε the viscous dissipation and k the heat conductivity. The viscous dissipation is usually small compared to the heat conduction, and may be neglected in most cases. In reality, both c_p, k and the viscosity μ vary with temperature. However, when temperature variations are small, as in marine hydrodynamic flows, these properties are assumed constant throughout the fluid.

The unknown quantities we obtain from equations 1.4, 1.5 and 1.8 are the three velocity components, pressure and (absolute) temperature. But, in most marine flow problems, only velocity and pressure are of interest. We observe that equations 1.4 and 1.5 can be solved for $\mathbf{u}$ and p without knowing T, and this is generally what's done in numerical marine hydrodynamics. Having found the velocity field, the temperature distribution can easily be obtained from equation 1.8.

Assuming incompressible flow and constant viscosity, Navier-Stokes equation 1.5 can be rewritten as follows:

$$\frac{\partial \mathbf{u}}{\partial t} + (\mathbf{u} \cdot \boldsymbol{\nabla})\mathbf{u} = -\boldsymbol{\nabla} p + \nu \boldsymbol{\nabla}^2 \mathbf{u} + \mathbf{f} \tag{1.9}$$

Equation 1.9 is often referred to as the *Laplacian form* of Navier-Stokes equation. It is a system of nonlinear partial differential equations (PDEs), generally parabolic in nature. With proper initial and boundary conditions for the unknown variables, we can close the system of equations 1.4 and 1.9,

and get a well-posed problem. "Well-posed" means that a solution to the problem must exist, be unique, and depend continuously upon the initial or boundary data. The initial condition is simply a start-up field; a known solution in the whole domain (including the bondaries) at $t = 0$, i.e

$$\mathbf{u} = \mathbf{u}_0 \quad \text{and} \quad p = p_0 \quad \text{at} \quad t = 0 \tag{1.10}$$

The boundary conditions for a PDE generally fall into two categories:

1. *Dirichlet* condition: Variable values are given at the boundaries.
2. *Neumann* condition: Derivatives of the variables are given at the boundaries.

Denoting the solution domain Ω, the boundary $\partial\Omega$ consists of the parts Γ^D and Γ^N with Dirichlet and Neumann conditions, respectively. In the case of the incompressible Navier-Stokes equation, the Dirichlet condition is given by

$$\mathbf{u} = \mathbf{r}_D \quad \text{on} \quad \Gamma^D \tag{1.11}$$

The Neumann condition for the stress-strain formulation 1.5 is given as

$$\boldsymbol{\sigma} \cdot \mathbf{n} = \mathbf{r}_N \quad \text{on} \quad \Gamma^N \tag{1.12}$$

whereas for the Laplacian formulation 1.9, the condition reads

$$-p\mathbf{n} + \nu \frac{\partial \mathbf{u}}{\partial \mathbf{n}} = \mathbf{r}_N \quad \text{on} \quad \Gamma^N \tag{1.13}$$

where $\mathbf{n}$ is the outward normal vector. The expressions in 1.12 and 1.13 give the same exact solution, but the discrete solutions can be different. Equation 1.12 corresponds to prescribing an external force on Γ^N, while this is generally not the case for equation 1.13 (Melbø & Kvamsdal [16]). This can influence the computation of drag and lift forces on bodies.

Unique analytical solutions of the incompressible Navier-Stokes equation have been found only for a few laminar flow cases (i.e. low Reynolds number) with simple geometries (e.g. channel or pipe flow). For higher Reynolds numbers (Re), the equation becomes non-unique, and impossible to solve analytically. Physically, the flow becomes unstable, and undergoes a transition from laminar to turbulent as Re increases. So, in most real-life flow situations, we need to seek for a numerical solution.

Chapter 2

Computational fluid dynamics

Computational fluid dynamics, CFD, has roots in many disciplines. The interpretations of what CFD "really is" may differ considerably from, say, a mathematician to an engineer or a computer scientist. In the present work, focus will be on the numerical solution methods. In a broad sense, CFD is the art of finding a numerical solution to one or more flow equations in a given fluid domain by the use of computers. In our case, the flow equations are the incompressible Navier-Stokes equations. Solving these equations numerically is an area of intensive research. A large number of methods have been developed, and are constantly being improved. It's beyond the scope of this work to cover every aspect of such solution methods in great detail. However, some key concepts which are crucial in all CFD will be dealt with in the following sections.

2.1 General solution of Navier-Stokes equation

2.1.1 Two-dimensional solution approach

For many applications, solving the incompressible Navier-Stokes equation in two dimensions (2D) can be an attractive modeling approach. In marine hydrodynamics, roll damping of ships is a good example. In this case, the water is mostly flowing within cross-sectional planes perpendicular to the ship's longitudinal axis. We only have three-dimensional (3D) effects near the bow and stern, and these effects are not very pronounced. Thus, a 2D analysis may be expected to give reasonable results. In industry today, 2D modeling is also applied to cases where the simplification is less valid, perhaps due to limited hardware or software resources, or a lack of knowledge. Either

way, 2D methods are still used even if 3D calculations may be regarded as "state-of-the-art" in CFD as a whole.

A popular method restricted to 2D is the *vorticity-stream function approach*. Here, a change of variables is made in order to eliminate the pressure from Navier-Stokes equations. The *vorticity vector* $\boldsymbol{\zeta}$ is defined as

$$\boldsymbol{\zeta} = \boldsymbol{\nabla} \times \mathbf{u} \tag{2.1}$$

where $\mathbf{u} = (u,v)$ is the two-dimensional velocity vector. The scalar value of the vorticity is

$$\zeta = \frac{\partial v}{\partial x} - \frac{\partial u}{\partial y} \tag{2.2}$$

A transport equation for the scalar value of vorticity can be obtained by manipulation of the x- and y-momentum equations, thereby eliminating the pressure:

$$\frac{D\zeta}{Dt} = \nu \boldsymbol{\nabla}^2 \zeta \tag{2.3}$$

In two dimensions, the *stream function* ψ is defined by

$$\frac{\partial \psi}{\partial y} = u \tag{2.4}$$

$$\frac{\partial \psi}{\partial x} = -v \tag{2.5}$$

Inserting equatons 2.4 and 2.5 into 2.2 gives a Poisson equation for ψ:

$$\boldsymbol{\nabla}^2 \psi = -\zeta \tag{2.6}$$

Equations 2.3-2.6 can be solved using a time-marching procedure. Having found u and v, the (kinematic) pressure can be obtained from the following equation:

$$\boldsymbol{\nabla}^2 p = 2\left(\frac{\partial u}{\partial x}\frac{\partial v}{\partial y} - \frac{\partial u}{\partial y}\frac{\partial v}{\partial x}\right) \tag{2.7}$$

So, in this approach, pressure and velocity are *decoupled* in an exact way. This greatly reduces the computational work compared to solving the original Navier-Stokes equations.

2.1.2 Three-dimensional approaches

In three space dimensions, the stream function does not exist. Consequently, the vorticity-stream function approach cannot be used in the way described above. Three-dimensional generalizations of the method have been developed, but much of the advantage present in 2D is lost in the process. So, in

3D the incompressible Navier-Stokes equations are most often solved directly for velocity and pressure, the *primitive variables* of the flow problem. The incompressibility assumption does however lead to some difficulties, because the time derivative of density is removed from the continuity equation. As a consequence, pressure waves propagate at infinite speed through the fluid, and not with the (finite) speed of sound, which is the correct physical behaviour. From a purely physical point of view, this is not a big problem, since we operate with flow velocities far below the speed of sound. (This is exactly the argument for assuming incompressibility in the first place, as previously mentioned). The real problem lies in the mathematical behaviour of the new equation system. The presence of a density time derivative is the mechanism which prevents the problem from becoming singular for low Mach numbers. In compressible flow, velocity and density are related in the continuity equation, and pressure is in turn linked to density through the equations of state. But in the *in*compressible system of equations, this relation is missing, so there is no obvious way of linking pressure with velocity. Numerically, this may lead to a singular system of algebraic equations.

Many methods have been proposed for solving the incompressible Navier-Stokes equations over the last three decades. The main challenge has been to find a consistent way of linking pressure with velocity, as described above. Most of the solution methods fall into two broad categories; *coupled* or *uncoupled*.

In the *coupled approaches*, all dependent variables (u, v, w and p) are treated as simultaneous unknowns. An important group of coupled methods are based on a technique proposed by *A.J. Chorin* [20] in 1967, the *artificial compressibility method*. Here, the incompressible continuity equation 1.4 is given a perturbation of the form $\partial\rho^*/\partial t^*$, where ρ^* is an artificial density. This is done to stabilize the system, and get a nonsingular behaviour. The fictitious time scale t^* is analogous to real time in compressible flow. When the solution converges to steady state, the artificial compressibility term vanishes. The artificial density is related to the pressure through $p = \rho^*/\epsilon$, an artificial equation of state. The compressibility factor ϵ is chosen to facilitate fast convergence. The optimal value of ϵ can be problem dependent. Since we're looking for a time independent solution, the physical time scale t in the momentum equation can be substituted by t^*. Thus, we get the following system of equations:

$$\frac{\partial \mathbf{u}}{\partial t^*} + (\mathbf{u}\cdot\boldsymbol{\nabla})\mathbf{u} = -\boldsymbol{\nabla}p + \nu\boldsymbol{\nabla}^2\mathbf{u} + \mathbf{f} \tag{2.8}$$

$$\boldsymbol{\nabla}\cdot\mathbf{u} + \epsilon\frac{\partial p}{\partial t^*} = 0 \tag{2.9}$$

This problem can be solved by using standard time-dependent techniques developed for compressible flow. A major drawback is obviously that this method can only be used for steady flow problems. A slightly different method proposed by *Hughes et al* [21] also uses a modified continuity equation, but in this case, the added term is of the form ϵp, with ϵ as a small *penalty parameter*:

$$\boldsymbol{\nabla} \cdot \mathbf{u} + \epsilon p = 0 \tag{2.10}$$

Equation 2.10 is inserted into the momentum equation in order to eliminate the pressure:

$$\frac{\partial \mathbf{u}}{\partial t} + (\mathbf{u} \cdot \boldsymbol{\nabla})\mathbf{u} = \frac{1}{\epsilon}\boldsymbol{\nabla}(\boldsymbol{\nabla} \cdot \mathbf{u}) + \nu \boldsymbol{\nabla}^2 \mathbf{u} \tag{2.11}$$

This equation can be solved directly for the velocity, and the pressure can subsequently be found from 2.10. This strategy, referred to as the *penalty method*, can also be used for unsteady problems, unlike the artificial compressibility method. However, it's not obvious how to choose ϵ. A too small ϵ will lead to a numerical ill conditioning. Chosen too large, ϵ may cause unacceptable errors in the continuity equation, which amount to a net loss or gain of fluid. This error can bee seen as the "penalty" of the method.

The *uncoupled approaches* represent a different strategy to solving the incompressible Navier-Stokes equations. These methods are also referred to as pressure correction, sequential or segregated methods. Here, the momentum equation 1.9 is solved componentwise for the velocity, using the best pressure estimate available, typically the pressure distribution from the previous time step. However, the new velocity field will generally not satisfy the continuity equation. Consequently, a separate equation for the pressure is solved, which satisfies the incompressibility constraint. The velocity field is then corrected with the new and improved pressure distribution.

An early example of this approach is the *projection method,* proposed by A.J. Chorin [22] in 1968. This method is applied in the Navier-Stokes solver used in the present study (see also chapter 3). The method is also known as the *fractional step* or *operator splitting* method, and is quite prototypical of the uncoupled solution strategies. (The term *splitting* reflects that the velocity field is split into a divergence free and a curl free part.) As a first step, the momentum equations are advanced in time, neglecting the pressure gradient term, in order to obtain an intermediate velocity $\widetilde{\mathbf{u}}$. If we use the backward Euler time discretization scheme (see section 2.3), this step will read**:**

$$\frac{\widetilde{\mathbf{u}} - \mathbf{u}^n}{\delta t} = -(\widetilde{\mathbf{u}} \cdot \boldsymbol{\nabla})\widetilde{\mathbf{u}} + \nu \boldsymbol{\nabla}^2 \widetilde{\mathbf{u}} + \mathbf{f}^{n+1} \tag{2.12}$$

where superscript n denotes the time step. The velocity $\widetilde{\mathbf{u}}$ does not satisfy

the continuity equation. The updated pressure field is calculated from

$$\frac{\mathbf{u}^{n+1} - \widetilde{\mathbf{u}}}{\delta t} = -\boldsymbol{\nabla} p^{n+1} \tag{2.13}$$

By taking the divergence of equation 2.13, and imposing the incompressibility constraint $\boldsymbol{\nabla}\mathbf{u}^{n+1} = 0$, we obtain a Poisson equation for the pressure:

$$\boldsymbol{\nabla}^2 p^{n+1} = \frac{\boldsymbol{\nabla}\widetilde{\mathbf{u}}}{\delta t} \tag{2.14}$$

In summary, the algorithm consists of three steps:

1. Calculate the intermediate velocity $\widetilde{\mathbf{u}}$ from equation 2.12.
2. Solve equation 2.14 for the new pressure p^{n+1}.
3. Calculate the new velocity $\mathrm{u}^{n+1}$from equation 2.13

Another variant of the method carry over pressure information from the previous time step, and the momentum equation may have the form (step 1):

$$\frac{\widetilde{\mathbf{u}} - \mathbf{u}^n}{\delta t} = -(\widetilde{\mathbf{u}} \cdot \boldsymbol{\nabla})\widetilde{\mathbf{u}} - \beta \boldsymbol{\nabla} p^n + \nu \boldsymbol{\nabla}^2 \widetilde{\mathbf{u}} + \mathbf{f}^{n+1} \tag{2.15}$$

where β is used as a relaxation parameter, and may be adjusted to improve convergence. In this case, the pressure equation 2.13 will read

$$\frac{\mathbf{u}^{n+1} - \widetilde{\mathbf{u}}}{\delta t} = -\boldsymbol{\nabla}(p^{n+1} - \beta p^n) \tag{2.16}$$

and the Poisson equation:

$$\boldsymbol{\nabla}^2 (p^{n+1} - \beta p^n) = \frac{\boldsymbol{\nabla}\widetilde{\mathbf{u}}}{\delta t} \tag{2.17}$$

A whole range of methods that follow a similar strategy has been developed over the years, with varying level of sophistication. However, the general principles remain:

1. Calculate an intermediate velocity field without satisfying continuity,
2. solve a separate pressure equation which *does* satisfy continuity, and
3. correct the velocity field according to the new/improved pressure field.

Many methods also apply iteration between momentum and pressure equations until a divergence free velocity field is obtained. Details of specific methods apart from the one described above will not be given here.

2.2 Space discretization

In fluid mechanics, as well as many other physical sciences, the world is viewed as a continuum. This means that physical properties are imagined to be distributed throughout space. The natural independent variables are three-dimensional space and time. The basic equations of fluid flow are based on the continuum assumption. However, in order to solve the equations numerically, the dependent variables are considered to exist only at *discrete points in space and time*. The result of discretizing the problem domain is that a system of generally insolvable PDEs transforms into a system of algebraic equations which *can* be solved.

The first step in any spatial discretization scheme is to construct a *mesh* or *grid* for the fluid domain. The grid file is generally made up of three main types of information :

- A list of coordinates for the grid points where flow variables are to be calculated (also called *vertices* or *nodes*)
- Information about how the grid points are connected
- Boundary information

The connectivity information may appear as indexing of the grid points. This is the case for *structured grids,* where each internal grid point has the same number of neighbours. In 2D, the (closest) neighbours of the point (i,j) then becomes $(i+1,j)$, $(i\text{-}1,j)$, $(i,\ j+1)$ and $(i,\ j\text{-}1)$. In *unstructured grids*, each point may have a different number of neighbours. In this case, the connectivity is given explicitly in a table. The connectivity may also tell us how grid points are grouped together in cells or elements, depending on the choice of discretization method. Boundary information in its simplest form is merely a set of indicators; numbers which act as name tags, telling the CFD code if a grid point belongs to a boundary, and if so, which boundary. The theory and practice of grid generation is a large topic in itself. Further details can be found in [23], and its references.

The most common space discretization schemes used in CFD are *local*, which means that the flow variables at any given point only depend upon the values at neighbouring points (here meaning "points nearby", not necessarily the *closest* neighbours only). The most widely used local techniques are the *Finite Difference Method* (FDM), the *Finite Volume Method* (FVM) and the *Finite Element Method* (FEM).

2.2.1 Finite Difference Method

The *Finite Difference Method* (FDM) uses the differential form of the conservation equations as its starting point. Each of the space derivatives in the Navier-Stokes and continuity equations are replaced by difference formulas. These formulas are commonly based on Taylor series expansion. Consider for instance the one-dimensional Taylor series

$$u(x+h,t) = u(x,t) + h\frac{\partial u(x,t)}{\partial x} + \frac{1}{2!}h^2\frac{\partial^2 u(x,t)}{\partial x^2} + \frac{1}{3!}h^3\frac{\partial^3 u(x,t)}{\partial x^3} + ... \quad (2.18)$$

Rearranging this yields the following expression for the first derivative:

$$\frac{\partial u(x,t)}{\partial x} = \frac{u(x+h,t) - u(x,t)}{h} + O(h) \quad (2.19)$$

In our case, h is the grid spacing. Equation 2.19 is a *forward difference approximation* of the space derivative, or just *forward space*. The expression is *first order accurate*, which means that the leading error term is of first order in h, denoted $O(h)$. Similarly, we may use the Taylor series

$$u(x-h,t) = u(x,t) - h\frac{\partial u(x,t)}{\partial x} + \frac{1}{2!}h^2\frac{\partial^2 u(x,t)}{\partial x^2} - \frac{1}{3!}h^3\frac{\partial^3 u(x,t)}{\partial x^3} + ... \quad (2.20)$$

to obtain the *backward space* approximation:

$$\frac{\partial u(x,t)}{\partial x} = \frac{u(x,t) - u(x-h,t)}{h} + O(h) \quad (2.21)$$

Using backward difference for the convection term is often referred to as *upwinding*. The effect of upwinding is similar to adding positive diffusion to the equation. This is often employed to stabilize the solution in advection-dominated problems, even if this means altering the physics of the problem slightly.

Subtracting equations 2.20 from 2.18 yields the second order accurate *central difference* approximation for the first space derivative:

$$\frac{\partial u(x,t)}{\partial x} = \frac{u(x+h,t) - u(x-h,t)}{2h} + O(h^2) \quad (2.22)$$

The central difference for the 2nd derivative (or Laplacian) reads

$$\frac{\partial^2 u(x,t)}{\partial x^2} = \frac{u(x+h,t) - 2u(x,t) + u(x-h,t)}{h^2} \quad (2.23)$$

Higher order approximations may be obtained in a similar manner as described above. As an example, using the central space approximations for

both 1st and 2nd derivatives of velocity, we obtain the following semi-discrete version (discretized in space, but not in time) of the x-component of Navier-Stokes equation 1.8 in 2D:

$$\frac{\partial u_{i,j}}{\partial t} + u_{i,j}\frac{u_{i+1,j} - u_{i-1,j}}{2\delta x} + v_{i,j}\frac{u_{i,j+1} - u_{i,j-1}}{2\delta y} = -\frac{p_{i+1,j} - p_{i-1,j}}{2\delta x} + \nu\left(\frac{u_{i+1,j} - 2u_{i,j} + u_{i-1,j}}{\delta x^2} - \frac{u_{i,j+1} - 2u_{i,j} + u_{i,j-1}}{\delta y^2}\right) + f_{1i,j} \tag{2.24}$$

Eq. 2.24 is solved at point (x_i, y_j), and the index notation used here implies that $u_{i+1,j} = u(x_i + \delta x, y_j, t)$, $u_{i,j-1} = u(x_i, y_j - \delta y, t)$ and so on. δx and δy are the grid spacings in the x- and y-direction, respectively. The discrete continuity equation reads

$$\frac{u_{i+1,j} - u_{i-1,j}}{2\delta x} + \frac{v_{i,j+1} - v_{i,j-1}}{2\delta y} = 0 \tag{2.25}$$

The extension to 3D is straightforward, and we get expressions similar to 2.24 and 2.25. The scheme results in a system of algebraic equations, with the nodal values as unknowns.

An alternative way of approximating the derivatives is to fit nodal values to an interpolation curve, and differentiate the resulting curve. This technique is called *polynomial fitting*. See e.g. Cheney & Kincaid [24] for details.

The historical roots of FDM dates back to the 18th century, when Leonhard Euler first studied the calculus of finite differences. FDM schemes were also the first to be applied in CFD. When applied to a regular grid with rectangular (2D) or prismatic (3D) cells on a simple domain (i.e. channel flow, cavity flow), FDM is easy to implement, and can be very efficient. For general geometries and less regular grids, however, the implementation soon becomes quite complicated, especially with regards to boundary conditions. Also, since FDM is a strictly *nodal (*or *point) based* method using the differential form of governing equations, global mass conservation tends to be poor. Due to these drawbacks, the finite difference method is rarely used in commercial CFD codes nowadays. However, FDM still has its appeal for academic purposes, mainly because of its conceptual simplicity and efficiency for simple, "academic" flow cases. Details about the finite difference method can be found in several text books, for example [18] and [26].

2.2.2 Finite Volume Method

The *Finite Volume Method* (FVM) was originally developed as a special version of the finite difference formulation, tailor-made for fluid flow and heat

transfer problems. FVM is the most popular discretization method in engineering CFD, including ship hydrodynamics applications. As the name implies, FVM is a *volume based method.* It uses the integral form of the conservation equations as its starting point, as opposed to FDM, which uses the differential form of the equations. The solution domain is subdivided into a finite number of contiguous *control volumes (CV)*, also called *cells* or *elements*. The conservation principles are applied directly to the CVs. Conservation of a general flow variable ϕ within a CV is achieved through a balancing of the fluxes of ϕ across the CV's boundaries and the net creation of ϕ inside the CV. Transformation of spatial derivatives into fluxes is accomplished by using Gauss' divergence theorem. Mathematically, this approach leads to an integral formulation of the Navier-Stokes equation 1.5 and continuity equation 1.4:

$$\frac{\partial}{\partial t}\iiint_{CV}\mathbf{u}dV + \mathbf{u}\iint_{A}u_n dA = \iint_{A}(\sigma\cdot\mathbf{n})dS + \iiint_{CV}\mathbf{f}dV \quad (2.26)$$

$$\iint_{A}(\mathbf{u}\cdot\mathbf{n})dA = 0 \quad (2.27)$$

Here, A denotes the total surface area of the control volume CV, $\mathbf{n}$ the outward normal vector to A, and u_n the normal velocity of fluid across A, positive outwards. Otherwise, previous definitions apply. The unknowns of eq. 2.26 and 2.27 are calculated at nodal points within each control volume, and are assumed constant over the CV. Thus, the volume integral of any value over CV is simply the nodal value times the volume of the element. Gradients at nodal points may be approximated by difference formulas, similar to FDM. In 3D, the surface A consists of a given number of polyhedral boundary faces. Consequently, the flux integral of e.g. a scalar ϕ over A will be the area a_i of face i, times the unknown ϕ_i times the normal vector, summed over the number of faces N:

$$\iint_{A}\phi\mathbf{n}dA = \sum_{i=1}^{N}a_i\phi_i\mathbf{n}_i \quad (2.28)$$

Values of ϕ at the boundaries are commonly approximated by interpolation between nodal points. The simplest case is linear interpolation. Gradients at boundary faces are also calculated using nodal values at neighbouring points. The actual choice of approximation techniques for the different terms may be problem dependent, or just a matter of taste. The finite volume discretization results in an algerbaic equation system, analogous to FDM. However, despite the apparent similarities, FVM does have some important advantages over FDM:

- Both local and global mass conservation is automatically satisfied in FVM.
- FVM allows for easier treatment of boundary conditions for complex domains.
- FVM is better adapted for the use of unstructured grids.

The last item is especially important for handling complex geometries, as unstructured grids can fit arbitrary domain boundaries, and the grid generation process can be fully automated. This is one of the reasons for the method's popularity in industrial use. Also, the fact that all terms in the equations have direct physical meaning makes FVM particularly attractive to engineers. Further details about the finite volume method can be found in e.g. [25] and [26].

2.2.3 Finite Element Method

The *Finite Element Method* (FEM) was first applied as a computational tool in the field of structural engineering. Here it became a powerful method for calculating stresses and strains in various load-bearing structures. Subsequently, using variational methods and functional analysis, mathematicians have developed FEM into a general method of solving partial differential equations. In this context, the finite element method as we know it today has been equipped with a strong mathematical foundation, with the availability of theoretical error estimates and error bounds. The method has its followers in the CFD community, especially among mathematicians. However, in the fluid engineering community, FEM is generally regarded as more abstract and difficult to comprehend in a fluid dynamics context, as compared to the finite volume method. Despite this view, the finite element method applied to fluid flow problems resembles FVM in many ways. In FEM the computational domain is subdivided into a set of volumes called *finite elements*, quite similar to the finite volumes in FVM. However, the distinguishing feature of FEM is that the differential form of the conservation equations are multiplied by *test functions* before they are integrated over the computational domain. In FVM, the integral form of the conservation equations are used directly.

The mathematical statement which forms the most common "point of departure" for finite element methods in CFD is the *variational* (or *weak*) *formulation* of the Navier-Stokes equation system. This form is obtained by multiplying equations 1.5 and 1.4 by test functions $\mathbf{v}$ and q respectively, and

then integrate over the fluid domain Ω with boundary $\Gamma = \Gamma^D \cup \Gamma^N$. The variational formulation reads (Laplacian form):

Find $\mathbf{u} \in U$ and $p \in Q$ such that

$$\int_\Omega \left(\frac{\partial \mathbf{u}}{\partial t}\mathbf{v} + (\mathbf{u}\cdot\boldsymbol{\nabla})\mathbf{u}\mathbf{v} + \nu\boldsymbol{\nabla}\mathbf{u}\cdot\boldsymbol{\nabla}\mathbf{v} - p(\boldsymbol{\nabla}\cdot\mathbf{v}) \right) d\Omega = \tag{2.29}$$

$$\int_\Omega f\cdot\mathbf{v}d\Omega + \int_{\Gamma^N} \mathbf{r}_N\cdot\mathbf{v}dS \quad \forall v \in V$$

$$\int_\Omega q(\boldsymbol{\nabla}\cdot\mathbf{u})d\Omega = 0 \quad \forall q \in Q \tag{2.30}$$

with boundary conditions

$$\mathbf{u} = \mathbf{r}_D \quad \text{on} \quad \Gamma^D \quad (Dirichlet) \tag{2.31}$$

$$-p\mathbf{n} + \nu\frac{\partial \mathbf{u}}{\partial \mathbf{n}} = \mathbf{r}_N \quad \text{on} \quad \Gamma^N \quad (Neumann) \tag{2.32}$$

The functional spaces U, V and Q are defined by

- $U = \{\mathbf{v}$ sufficiently smooth and satisfy $\mathbf{v}|_{\Gamma^D} = \mathbf{r}_D\}$
- $V = \{\mathbf{v}$ sufficiently smooth and satisfy $\mathbf{v}|_\Gamma = 0\}$
- $Q = \{q$ sufficiently smooth and satisfy $\int_\Omega q d\Omega = 0\}$

The formulation above is commonly referred to as the *Galerkin finite element formulation*, perhaps the most common FEM approach. Discretization of the problem is done by introducing a finite *nodal basis* for the functional spaces. If N_i is a nodal basis function, it has by definition the value one at node i, and zero everywhere else. In FEM, nodes include all the element corners, and can also include point(s) inside the element. The discrete approximation $\mathbf{u}_h$ may then be written:

$$\mathbf{u}_h(\mathbf{x}, t) = \sum_{i=1}^{n_{DOF}} \mathbf{u}_i N_i \tag{2.33}$$

where $\mathbf{u}_i = \mathbf{u}_h(\mathbf{x}_i, t)$ is the unknown nodal value. Subscript DOF denotes "degrees of freedom". We get a similar expression for the test function $\mathbf{v}$. The functions N_i are piece-wise polynomials, usually of low order, often exemplified in literature by so-called "hat functions" in one space dimension. The resulting one-dimensional approximation will then be piece-wise linear.

In 3D, the analogue is a "trilinear" basis function, i.e. linear in each space dimension. Many alternative basis functions may be used, however, they must produce a continuous solution for the velocity. The basis functions ϕ_i for the pressure is often of one order lower than the velocity basis function. This is motivated by the fact that the weak formulation includes 1st order derivatives of the velocity, while there are no pressure derivatives, only the pressure itself, see eq. 2.29. We get

$$p_h(\mathbf{x}, t) = \sum_{i=1}^{n_{DOF}} p_i \phi_i \tag{2.34}$$

where $p_i = p_h(\mathbf{x}_i, t)$.

The resulting semi-discrete algebraic equations may be written in the following compact matrix-vector form:

$$\mathbf{M}\frac{\partial \mathbf{u}}{\partial t} + [\mathbf{K} + \mathbf{L}(\mathbf{u})]\mathbf{u} + \mathbf{C}p = \mathbf{b}_f + \mathbf{b}_t \tag{2.35}$$

$$\mathbf{C}^T\mathbf{u} = 0 \tag{2.36}$$

Here, $\mathbf{u}$ and p are vectors containing the unknown (discrete) velocities and pressures, respectively. Further, $\mathbf{b}_f = \int_\Omega f \cdot \mathbf{v} d\Omega$ and $\mathbf{b}_t = \int_{\Gamma^N} \mathbf{r}_N \cdot \mathbf{v} dS$ (r.h.s of 2.29). The subscript h is dropped for convenience. (Note: Bold face is *not* used for the pressure vector, in order to indicate that it's (still) a scalar value, though represented mathematically as a vector in this case). The coefficient matrices are commonly named as follows:

- $\mathbf{M}$ is the *mass matrix*
- $\mathbf{K}$ is the *viscous* (or *diffusion*) *matrix*
- $\mathbf{L}(\mathbf{u})$ is the nonlinear *advection* (or *convection*) *matrix*
- $\mathbf{C}$ is the *coupling matrix* (it couples the velocity and the pressure)

The global coefficient matrices are assembled from element matrices in a quite mechanical way, element by element. For details on the construction of these matrices, see e.g. Gresho & Sani [28].

Apart from the strong mathematical foundation, a great advantage of the finite element method is the built-in ability to incorporate different physical boundary conditions on complex domains, especially the Neumann type. Also, FEM is often considered more accurate than FVM. For these and other reasons, FEM is chosen as the space discretization technique in the Navier-Stokes solver used in the present work (ref. chapter 3). For more details on FEM in the context of fluid dynamics, see [27], [28].

2.2.4 Global methods

The discretization schemes mentioned thus far are local, low order methods. For most engineering purposes, the accuracy and convergence properties of these methods are satisfactory. However, higher accuracy and/or faster convergence may be needed in certain cases, for example in time-dependent problems where long time integration is required. A typical example is direct numerical simulation of turbulence. The method of choice for these problems are often *spectral methods*. An important sub-category of the spectral discretization methods is the *spectral element method*, also called spectral Galerkin method. The overall procedure is similar to FEM as described above, but the nodal basis functions are *global* polynomials, instead of the piece-wise polynomials used in FEM. Common basis functions are the Chebyshev or Legendre type polynomials, and the grid is formed using various types of Gauss points. Another type of spectral method is the *spectral collocation* (or *pseudo-spectral*) *method*. Here, a set of global polynomials are used to interpolate the original Navier-Stokes equation directly at certain collocation points, also of Gaussian type.

The local methods described in previous sections all result in algebraic equations for which the coefficient matrices (see eq. 2.35 and 2.36) are *sparse* (i.e. many zero elements). Sparse matrix systems can be solved very efficiently, using comparatively little storage space. Spectral methods, on the other hand, produce full matrices, consequently the system is much more expensive to solve. However, spectral methods are more accurate and converge faster, so fewer nodes and fewer iterations are needed to obtain the same degree of accuracy compared to local methods. The reason why spectral methods are rarely used in industrial CFD is that the use of global polynomials severely reduces the flexibility with respect to handling complex domain geometries. For details on spectral methods, see [29].

2.3 Time discretization

So far, we have only considered a few approaches to spatial discretization of the Navier-Stokes equations, leaving time as a continuous variable. From a mathematical point of view, time could readily be treated as yet another space dimension, an approach which is employed by e.g. Zienkiewicz & Taylor [27]. However, there are some important arguments in favour of treating time differently. The most obvious is that time, unlike space, is hyperbolic in nature, which means that it has a definite direction of influence. Information can only travel forwards in time, whereas in space information can

travel in any direction. Furthermore, higher-order schemes produce very large matrix systems, which makes them quite expensive to solve [30]. Finally, advancing time in a step-by-step or "marching" manner enables us to write the semi-discrete algebraic equations as a set of ordinary differential equations (ODEs), for which there exist a great variety of sophisticated numerical methods. Consequently, the latter approach is most widespread in CFD.

Assuming some kind of spatial discretization of the Navier-Stokes system is already performed, the remaining problem can be expressed as

$$\frac{d\mathbf{u}(t)}{dt} = \mathbf{f}(t, \mathbf{u}(t)); \quad \mathbf{u}(t_0) = \mathbf{u}^0 \tag{2.37}$$

where $\mathbf{u}(t)$ is a vector containing all the unknowns. Eq. 2.37 is an *initial value problem*, where the basic task is to find the solution a short time δt after the initial time t_0, at which the solution is known. The solution $\mathbf{u}^1$ at $t_1 = t_0 + \delta t$ forms a new initial condition, and the solution can be advanced to $t_2 = t_1 + \delta t$, $t_3 = t_2 + \delta t$,... and so on. Only a few of the simpler methods for solving 2.37 are included here, in order to illustrate the main principles.

The starting point for many methods is obtained by integrating eq. 2.37 from t_n to t_{n+1}:

$$\mathbf{u}^{n+1} - \mathbf{u}^n = \int_{t_n}^{t_{n+1}} \mathbf{f}(t, \mathbf{u}(t))dt \tag{2.38}$$

Thus, the problem is reduced to finding some approximation to the integral on the right hand side. If we use the value of the integrand at the initial point t_n to evaluate the integral, we have:

$$\mathbf{u}^{n+1} = \mathbf{u}^n + \mathbf{f}(t_n, \mathbf{u}^n)\delta t \tag{2.39}$$

which is known as the *forward* or *explicit Euler* method. The method is called explicit because it only requires values at t_n, which are already known. If we instead use t^{n+1}, we obtain the *backward* or *implicit Euler*:

$$\mathbf{u}^{n+1} = \mathbf{u}^n + \mathbf{f}(t_{n+1}, \mathbf{u}^{n+1})\delta t \tag{2.40}$$

We may also use values at a point midway between t_n and t_{n+1}:

$$\mathbf{u}^{n+1} = \mathbf{u}^n + \mathbf{f}(t_{n+\frac{1}{2}}, \mathbf{u}^{n+\frac{1}{2}})\delta t \tag{2.41}$$

which is commonly known as the *midpoint rule*. Another important scheme uses a straight line interpolation between t_n and $t_{n+1}$to approximate the integral:

$$\mathbf{u}^{n+1} = \mathbf{u}^n + \frac{1}{2}[\mathbf{f}(t_n, \mathbf{u}^n) + \mathbf{f}(t_{n+1}, \mathbf{u}^{n+1})]\delta t \tag{2.42}$$

This method is called the *trapezoid rule*. All the methods mentioned so far involve only a single time step δt, and are often referred to as *single-step methods*. The term *two-level method* is also used. Further, all the methods mentioned above except the first one (forward Euler) are *implicit*. These methods require values of $\mathbf{u}$ at points other than t_n, where the solution is known. Thus, in order to calculate the right hand side, further approximation or iteration is needed. Explicit methods, on the other hand, can be solved directly. Details on time stepping schemes can be found in many textbooks, e.g Ferziger & Peric [26].

2.4 Boundary conditions in CFD

As mentioned earlier, initial and boundary conditions are needed to get a closed set of algebraic equations to be solved numerically. In general, every boundary node must have one condition (Dirichlet or Neumann) for each of the unknown variables, in order to close the equations, but not overdetermine the problem. In CFD, it is common to divide the boundary conditions into *physical* and *artificial* (or *computational)* boundary conditions. Physical boundary conditions are imposed exactly as in the real world, such as e.g rigid, no-slip walls. In cases where the physical flow domain is infinite (in one or more directions), artificial boundary conditions are used to create a bounded (finite sized) computational domain. In other cases when the real world conditions are indeterminable and/or hard to implement, artificial conditions are created in order to mimic the real conditions as closely as possible. Artificial boundary conditions include e.g far field and outflow conditions. "Far field" means far enough away from no-slip walls so that any disturbance can be neglected. Examples of the most common "practical boundary conditions" (physical and artificial) used in CFD (incompressible calculations) are mentioned below:

- No-slip wall: zero velocity
- Inflow: prescribed normal velocity
- Far field: "free-slip wall", i.e prescribed tangential velocity or zero tangential stress (depending on formulation), in addition to zero normal velocity (no in- or outflow)
- Outflow: prescribed pressure or zero normal stress

It should be noted that the practical implementation of boundary conditions depends strongly upon the choice of general solution method and

discretization scheme, and will not be examined here. However, the general features of the examples given above should apply in most cases.

2.5 Some numerical aspects

In order to give a physically realistic and reasonably accurate solution to the flow problem at hand, the numerical method should possess certain properties. Some of the properties are determined unconditionally by the solution approach and discretization methods chosen, while other features may be problem dependent. The most important properties are commented in the following sections. Most of what's written is extracted from Tannehill et al[18] and Ferziger & Peric[26].

2.5.1 Consistency

Firstly, the discretization scheme should be *consistent*. Consistency means that the truncation error becomes zero when the grid spacing and/or time step goes to zero. Thus, the original differential equation is recovered. The truncation error is the difference between the exact and the discretized equations. Consistency can be demonstrated by replacing nodal values in the discretized equations by Taylor series expansions about a single point.

2.5.2 Stability

Furthermore, the method should give a *numerically stable* solution. A method is stable if it does not amplify errors occuring in the numerical simulation. For iterative methods, stability ensures a solution that does not diverge. For time dependent problems, stability guarantees a bounded solution of the discretized equation when the solution of the underlying differential equation is also bounded. We may define the *amplification factor* G of a time stepping or iterative scheme in the following way:

$$G = \frac{u^{n+1}}{u^n} \tag{2.43}$$

where u^n and $u^{n+1}$are numerical solutions at times t_n and t_{n+1}, respectively. The stability condition is then given as

$$|G| \leq 1 \tag{2.44}$$

This condition forms the basis of the *Fourier series method* (or *von Neumann* method), perhaps the most common stability analysis method (see e.g

Tannehill et al [18]). Other methods include the *matrix method* [18] and the *max-min method,* ref. Greenspan & Casulli, [31]. These methods are however difficult to apply to non-linear PDEs such as Navier-Stokes equations. Consequently, stability analysis for a given discretization scheme is normally performed on linearized model equations, investigating one term at a time. For example, the well-known CFL condition (Courant-Friedrich-Levy) is derived from the linearized convection equation (or first order wave equation). The CFL condition states that fluid should not be convected through more than one cell/element per time step, demanding that the time step is smaller than the minimum ratio of grid size to velocity. Analyzing linearized equations may give stability criteria which are *sufficient*, but too restrictive compared to the *necessary* criteria.

2.5.3 Convergence

In order to be usable, a numerical method has to be *convergent*, i.e the solution of the discretized equations should tend towards the exact solution of the PDE as the grid spacing and/or time step goes to zero. For a well-posed, linear initial value problem, *Lax' equivalence theorem* states that stability is a necessary and sufficient criteria for convergence of a consistent discretization scheme. However, convergence of non-linear problems with complex boundary conditions (e.g Navier-Stokes equations) is more difficult to prove theoretically. Numerical experiments are therefore commonly used to demonstrate convergence of a particular CFD code for a given flow problem.

2.5.4 Accuracy

All numerical solutions to fluid flow problems are *approximate* solutions, and will contain errors. There are several different types of errors. The *truncation error* is already mentioned, usually proportional to a power of the grid spacing h and/or the time step δt. If the leading term of the truncation error is proportional to e.g h^2 and δt^3, we say that the method is second order accurate in space and third order accurate in time, or $O(h^2, \delta t^3)$. However, as a measure of accuracy, this only tells us the *rate* at which the truncation error decreases as h and δt goes to zero, but nothing about the *magnitude* of the error itself in a given flow calculation. The truncation error together with errors due to boundary conditions fall under the collective term *discretization errors.*

The difference between the "real" flow and the exact solution of the mathematical model (i.e the PDE) is defined as the *modeling error.* As an example, the incompressibility assumption in the Navier-Stokes equation introduce

modeling errors if the velocities become very large. Another example are errors related to turbulence modeling.

Because digital computers have finite accuracy, any algebraic operation performed on a computer will have *round-off errors*. The total (accumulated) round-off error will normally increase with the number of algebraic operations, i.e it will become larger when the grid spacing and/or time step is reduced. Furthermore, most CFD codes involve iterative solution of algebraic equation systems. The difference between the iterative and exact solution of these equations are called the *iteration error*. The iteration errors can be controlled during the simulation by setting appropriate convergence criteria. The smaller we want the error to be, the stricter the criteria, and the more iterations are needed.

Controlling the errors, and knowing how the numerical method behaves when inevitable errors occur, is a major task in CFD. The goal is to achieve maximum accuracy with the available resources, or conversely, to obtain the desired accuracy at minimum computational cost.

Part II

Numerical experiments

Chapter 3

Computational method

The computer code used in the numerical experiments is called VISTA, developed at SINTEF Applied Mathematics in collaboration with NTNU. VISTA is an object oriented Navier-Stokes solver for incompressible flows, designed to run on large parallel computers. It is implemented in C++, using the numerical library *Diffpack*$^{\text{TM}}$ [32]. The calculations are performed on NTNU's high performance computing facilities [11], two SGI Origin 3800 machines with 896 processors combined, a total memory of 816 GB and a total peak performance of 998 Gflops.

The numerical solution methods applied in the VISTA code are described in chapter 2, but will be defined more precisely in the following sections.

3.1 General solution method

The general solution method applied in the code is the projection method introduced by *A.J. Chorin* [22]. In principle, this method consists of three steps. First, the momentum equations are advanced in time, neglecting the pressure gradient term, in order to obtain an intermediate velocity $\widetilde{\mathbf{u}}$ (ref. eq. 2.12):

$$\frac{\widetilde{\mathbf{u}} - \mathbf{u}^n}{\delta t} = -(\mathbf{u}^n \cdot \boldsymbol{\nabla})\widetilde{\mathbf{u}} + \nu \boldsymbol{\nabla}^2 \widetilde{\mathbf{u}} + \mathbf{f}^{n+1} \tag{3.1}$$

where superscript n denotes the time step. The velocity $\widetilde{\mathbf{u}}$ does not satisfy the continuity equation. In this case, the backward Euler time discretization method (with extrapolated convective velocity) is shown to exemplify the equation. The updated pressure field is calculated from

$$\frac{\mathbf{u}^{n+1} - \widetilde{\mathbf{u}}}{\delta t} = -\boldsymbol{\nabla} p^{n+1} \tag{3.2}$$

(Ref. eq. 2.13). By taking the divergence of eq. 3.2, and imposing the incompressibility constraint $\boldsymbol{\nabla}\mathbf{u}^{n+1} = 0$, we obtain a Poisson equation for the pressure (2.14):

$$\boldsymbol{\nabla}^2 p^{n+1} = \frac{\boldsymbol{\nabla}\widetilde{\mathbf{u}}}{\delta t} \tag{3.3}$$

Note that p is the kinematic pressure (i.e. pressure divided by density).

To summarize:

1. Calculate the intermediate velocity $\widetilde{\mathbf{u}}$ from eq. 3.1.

2. Solve eq. 3.3 for the new pressure p^{n+1}.

3. Calculate the new velocity $\mathrm{u}^{n+1}$from eq. 3.2

In VISTA, the operator splitting is performed on the continuous equations as shown above. The resulting equations are subsequently discretized. When performed in that order, the method is called the *continuous projection method*, as opposed to the *discrete* projection method, where the discretization comes first.

3.1.1 Splitting error

The splitting error term can be obtained by combining equations 3.1 and 3.2, eliminating the intermediate velocity $\widetilde{\mathbf{u}}$. The error term reads

$$e_S = \delta t(\nu\boldsymbol{\nabla}^2 - (\mathbf{u}^n \cdot \boldsymbol{\nabla}))\boldsymbol{\nabla}p^{n+1} \tag{3.4}$$

This term is $O(\delta t)$, and tends to stabilize the solution. Consequently, when δt becomes very small, the solution may become unstable.

3.2 Space discretization

Finite elements are used for space discretization. In the finite element method (FEM), the variational (weak) form of the conservation equations is used. The computational domain is subdivided into a set of volumes called *finite elements.* The variational form of the Navier-Stokes equation system is obtained by multiplying the differential form of the equations by test functions before integrating over the computational domain. The variational formulation reads (ref. equation 2.29 to 2.32):

Find $\mathbf{u} \in U$ and $p \in Q$ such that

$$\int_\Omega \left(\frac{\partial \mathbf{u}}{\partial t}\mathbf{v} + (\mathbf{u}\cdot\boldsymbol{\nabla})\mathbf{u}\mathbf{v} + \nu\boldsymbol{\nabla}\mathbf{u}\cdot\boldsymbol{\nabla}\mathbf{v} - p(\boldsymbol{\nabla}\cdot\mathbf{v}) \right) d\Omega = \tag{3.5}$$

$$\int_\Omega f\cdot\mathbf{v}d\Omega + \int_{\Gamma^N} \mathbf{r}_N\cdot\mathbf{v}dS \quad \forall v \in V$$

$$\int_\Omega q(\boldsymbol{\nabla}\cdot\mathbf{u})d\Omega = 0 \quad \forall q \in Q \tag{3.6}$$

with boundary conditions

$$\mathbf{u} = \mathbf{r}_D \quad \text{on} \quad \Gamma^D \quad (Dirichlet) \tag{3.7}$$

$$-p\mathbf{n} + \nu\frac{\partial \mathbf{u}}{\partial \mathbf{n}} = \mathbf{r}_N \quad \text{on} \quad \Gamma^N \quad (Neumann) \tag{3.8}$$

The functional spaces U, V and Q are defined by

- $U = \{\mathbf{v}$ sufficiently smooth and satisfy $\mathbf{v}|_{\Gamma^D} = \mathbf{r}_D\}$
- $V = \{\mathbf{v}$ sufficiently smooth and satisfy $\mathbf{v}|_\Gamma = 0\}$
- $Q = \{q$ sufficiently smooth and satisfy $\int_\Omega q d\Omega = 0\}$

Discretization of the problem is done by introducing a *finite nodal basis* for the functional spaces. The discrete approximation $\mathbf{u}_h$ may be written (ref. equation 2.33):

$$\mathbf{u}_h(\mathbf{x},t) = \sum_{i=1}^{n_{DOF}} \mathbf{u}_i N_i \tag{3.9}$$

where $\mathbf{u}_i = \mathbf{u}_h(\mathbf{x}_i,t)$ is the unknown nodal value and N_i denotes the nodal basis functions. We get a similar expression for the weight function $\mathbf{v}$. The functions N_i are piece-wise polynomials. In the VISTA code, the velocity basis functions can be of first or second order. The discrete approximation for the pressure may be written (ref. eq. 2.34):

$$p_h(\mathbf{x},t) = \sum_{i=1}^{n_{DOF}} p_i\phi_i \tag{3.10}$$

where $p_i = p_h(\mathbf{x}_i,t)$. The basis functions ϕ_i for the pressure are of first order in the VISTA code. The resulting semi-discrete algebraic equations

may be written in the following compact matrix-vector form (ref. equations 2.35-2.36):

$$\mathbf{M}\frac{\partial \mathbf{u}}{\partial t} + [\mathbf{K} + \mathbf{L}(\mathbf{u})]\mathbf{u} + \mathbf{C}p = \mathbf{b}_f + \mathbf{b}_t \quad (3.11)$$

$$\mathbf{C}^T\mathbf{u} = 0 \quad (3.12)$$

Here, $\mathbf{u}$ and p are vectors containing the unknown (discrete) velocities and pressures, respectively. Further, $\mathbf{b}_f = \int_\Omega f \cdot \mathbf{v} d\Omega$ and $\mathbf{b}_t = \int_{\Gamma^N} \mathbf{r}_N \cdot \mathbf{v} dS$ (r.h.s of 3.5). The subscript h is dropped for convenience. For details on the construction of the coefficient matrices $\mathbf{M}$, $\mathbf{K}$, $\mathbf{L(u)}$ and $\mathbf{C}$, see e.g. Gresho & Sani [28].

3.3 Time discretization

Three different time discretization schemes are implemented in VISTA; the backward Euler method (first order), the trapezoid rule combined with a modified Euler method (denoted trapez/Euler; second order), and the Crank-Nicholson/Adams-Bashforth method (second order). Semi-implicit versions are used, because the projection methods prohibit the use of fully implicit methods. The diffusion term is treated implicitly, while the convective velocity is taken from the previous time step. In this version, the backward Euler applied to Navier-Stokes equations reads as follows:

$$\frac{\mathbf{u}^{n+1} - \mathbf{u}^n}{\partial t} = -(\mathbf{u}^n \cdot \boldsymbol{\nabla})\mathbf{u}^{n+1} - \boldsymbol{\nabla} p^{n+1} + \nu \boldsymbol{\nabla}^2 \mathbf{u}^{n+1} + \mathbf{f}^{n+1} \quad (3.13)$$

$$\boldsymbol{\nabla} \cdot \mathbf{u}^{n+1} = \mathbf{0} \quad (3.14)$$

In the present computations, the backward Euler and trapez/Euler methods are used. See Holmen [36] for further details on the implementation of the schemes.

3.4 Turbulence model

The effect of turbulence is modelled using large-eddy simulation (LES). In LES, the larger unsteady turbulent motions are directly represented, whereas the effects of the smaller-scale motions are modelled. The velocity $\mathbf{u}(\mathbf{x}, t)$ is decomposed into a space filtered (or resolved) component $\overline{\mathbf{u}}(\mathbf{x}, t)$ and a residual (or subgrid-scale, SGS) component $\mathbf{u}'(\mathbf{x}, t)$, so that

$$\mathbf{u}(\mathbf{x}, t) = \overline{\mathbf{u}}(\mathbf{x}, t) + \mathbf{u}'(\mathbf{x}, t) \quad (3.15)$$

The decomposition (equation 3.15) is inserted into the Navier-Stokes equations, here written in Einstein notation, conservative form (omitting the body force for convenience):

$$\frac{\partial u_i}{\partial t} + \frac{\partial (u_i u_j)}{\partial x_j} = -\frac{\partial p}{\partial x_i} + \nu \frac{\partial^2 u_i}{\partial x_j \partial x_j} \tag{3.16}$$

$$\frac{\partial u_i}{\partial x_i} = 0 \tag{3.17}$$

The resulting filtered equations read:

$$\frac{\partial \overline{u}_i}{\partial t} + \frac{\partial (\overline{u_i u_j})}{\partial x_j} = -\frac{\partial \overline{p}}{\partial x_i} + \nu \frac{\partial^2 \overline{u}_i}{\partial x_j \partial x_j} \tag{3.18}$$

$$\frac{\partial \overline{u}_i}{\partial x_i} = 0 \tag{3.19}$$

The filtered product $\overline{u_i u_j}$ is different than the product of the filtered velocities $\overline{u}_i \overline{u}_j$. The difference is defined as the residual-stress tensor,

$$\tau_{ij}^R \equiv \overline{u_i u_j} - \overline{u}_i \overline{u}_j \tag{3.20}$$

The residual kinetic energy is

$$k_r \equiv \frac{1}{2} \tau_{ii}^R \tag{3.21}$$

and the anisotropic residual-stress tensor is defined as

$$\tau_{ij}^r \equiv \tau_{ij}^R - \frac{2}{3} k_r \delta_{ij} \tag{3.22}$$

where δ_{ij} is the Kronecker delta, defined as

$$\begin{aligned} \delta_{ij} &= 0 \quad \text{for} \quad i \neq j \\ &= 1 \quad \text{for} \quad i = j \end{aligned} \tag{3.23}$$

The isotropic part of the residual stress is absorbed into the pressure term, giving a modified filtered pressure:

$$\overline{p}' \equiv \overline{p} + \frac{2}{3} k_r \tag{3.24}$$

The filtered momentum equation (eq. 3.18) may then be rewritten as follows:

$$\frac{\partial \overline{u}_i}{\partial t} + \overline{u}_j \frac{\partial \overline{u}_i}{\partial x_j} = -\frac{\partial \overline{p}'}{\partial x_i} + \nu \frac{\partial^2 \overline{u}_i}{\partial x_j \partial x_j} - \frac{\partial \tau_{ij}^r}{\partial x_j} \tag{3.25}$$

Eq. 3.25 and 3.19 may be solved for $\overline{\mathbf{u}}(\mathbf{x},t)$ and $\overline{p}'(\mathbf{x},t)$ in the same manner as described in section 3.1. However, the filtered equations are unclosed, so we need a model for residual-stress tensor τ_{ij}^r, also called a *subgrid-scale (SGS) model*. The oldest and most well-known SGS model is the one due to Smagorinsky (1963), and this model is also implemented in the VISTA code. Here, the residual stress is related to the filtered rate of strain using the *eddy-viscosity hypothesis*:

$$\tau_{ij}^r = -2\nu_r \overline{S}_{ij}$$

where

$$\overline{S}_{ij} = \frac{1}{2}(\frac{\partial \overline{u}_i}{\partial x_j} + \frac{\partial \overline{u}_j}{\partial x_i}) \tag{3.26}$$

The eddy viscosity of the residual motions, $\nu_r(\mathbf{x},t)$, is modelled by analogy to Prandtl's mixing length hypothesis:

$$\nu_r = (C_S\Delta)^2\overline{\mathcal{S}} \tag{3.27}$$

where $\overline{\mathcal{S}} = (2\overline{S}_{ij}\overline{S}_{ij})^{\frac{1}{2}}$. C_S is the Smagorinsky coefficient and Δ the filter width. We may note that the actual filtering operation is never explicitly performed, but lies implicitly in the model for τ_{ij}^r. In our case, the filter width Δ is taken as the geometric mean of each element, i.e $\Delta = (\Delta_1\Delta_2\Delta_3)^{\frac{1}{3}}$, and is thus a function of the local grid resolution.

The basic Smagorinsky model as described above is not well suited for wall-bounded flows, since the residual viscosity does not vanish at the wall. A common remedy to this problem is to multiply ν_r by a damping function, which is unity in the free flow, but reduces to zero at the wall. In the VISTA code, the *van Driest damping function* is implemented, replacing the Smagorinsky coefficient with the following expression:

$$C_S = C_S^0[1 - \exp(-y^+/A^+)] \tag{3.28}$$

where $y^+ = u_\tau y/\nu$ is the distance from the wall in dimensionless (wall) units, $u_\tau = (\tau_w/\rho)^{\frac{1}{2}}$ the wall friction velocity, and τ_w the magnitude of the shear stress at the wall. A^+ is a dimensionless constant, normally taken to be 25. C_S^0 is commonly chosen to be 0.1, but may vary depending on the type of flow. Further details on large-eddy simulations may be found in e.g. Pope [41].

Chapter 4

Flow around a single cylinder

4.1 Introduction

Flow around a circular cylinder is one of the most studied flow cases in fluid dynamics. The geometry is very simple, yet this flow has many interesting and complex features, described by many researchers through theoretical, experimental and numerical work. Also, the circular cylinder plays an integral role in a large number of practical applications. Today, the rapid increase in computer power makes it possible to perform detailed numerical studies at ever increasing Reynolds numbers, and consequently, this flow case is still the subject of many studies. These considerations makes flow around a circular cylinder an ideal test case for verification and validation of CFD codes, as well as a good starting point for the study of more complex flows.

The behaviour of flow around a cylinder changes dramatically as the Reynolds number, defined as $Re = u_\infty d/\nu$, increases from zero. Here, u_∞ is the free stream velocity, d the cylinder diameter and ν the kinematic viscosity. Starting from rest, the flow around a cylinder is steady and stable. At Reynolds number $Re \sim 5$ a couple of symmetrical two-dimensional vortices are formed behind the cylinder. At $Re \simeq 45$ to 47 these vortices become unstable (the *primary* instability of the flow), and starts to shed successively from each side of the cylinder, leading to oscillating drag and lift forces on the cylinder. The vortex shedding continues for Reynolds numbers up to at least $O(10^5)$. This phenomenon is also known as the *von Kármán vortex street*, see figure 4.1.

The non-dimensional form of the shedding frequency f is defined as $St = f \cdot d/u_\infty$, known as the *Strouhal number*. The Strouhal number increases with increasing Reynolds number. At $Re \simeq 190$, the 2D oscillatory flow becomes unstable to long-wavelength 3D perturbations (the *secondary*

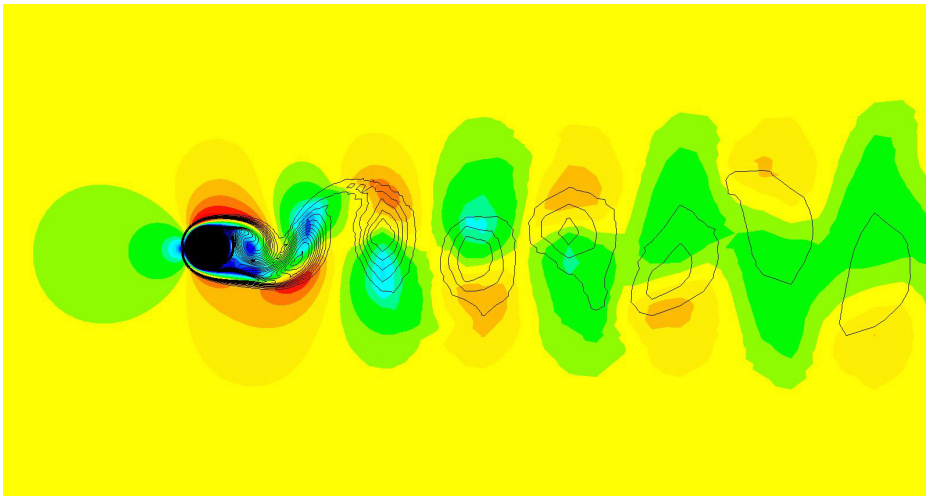

Figure 4.1: Von Kármán vortex street: velocity field (colormap) with vorticity contour lines (black). Results from 3D calculation at $Re = 265$, present study.

instability of the flow). A discontinuity ('jump') in the Strouhal-Reynolds number relationship occurs, see figure 4.2. Streamwise vortices are formed in the wake, together with a "waviness" in the primary vortex shedding. This flow regime is called 'mode A' (by C.H.K. Williamson [37]). Using stability analysis, Barkley and Henderson [38] showed that the transition to 'mode A' at $Re \simeq 190$ happens when the spanwise wavelength λ of the three-dimensional perturbation reach a critical value of 3.96 cylinder diameters. At $Re \simeq 260$, there is a second jump in the *St-Re* relationship. The following Reynolds number regime is called 'mode B', where the flow is unstable to short-wavelength instabilities, with a critical λ of 0.822 diameters [38]. A visualization of the flow patterns is shown in figure 4.3. An isosurface of the vorticity field is plotted at $Re = 265$ (results from present study, see section 4.2). The vorticity field is the scalar value of the vorticity vector, defined as $\boldsymbol{\zeta} = \boldsymbol{\nabla} \times \mathbf{u}$. We can clearly observe both the short- and long-wavelength instabilities. The three-dimensional wake patterns resulting from 'mode A' and 'mode B' have similar visual appearence, however at different length scales, but are assumed to arise from different physical mechanisms [37].

Curves of neutral stability for the 2D von Kármán wake with respect to 3D perturbations are shown in figure 4.4. From the figure we see that for a given Reynolds number larger than the critical value(s), $Re \simeq 190$ and $Re \simeq 260$, each instability mode is associated with a continuous band of wavelengths, not with a single wavelength value. The number of discrete wavelengths present in the wake depends on both Re and spanwise dimen-

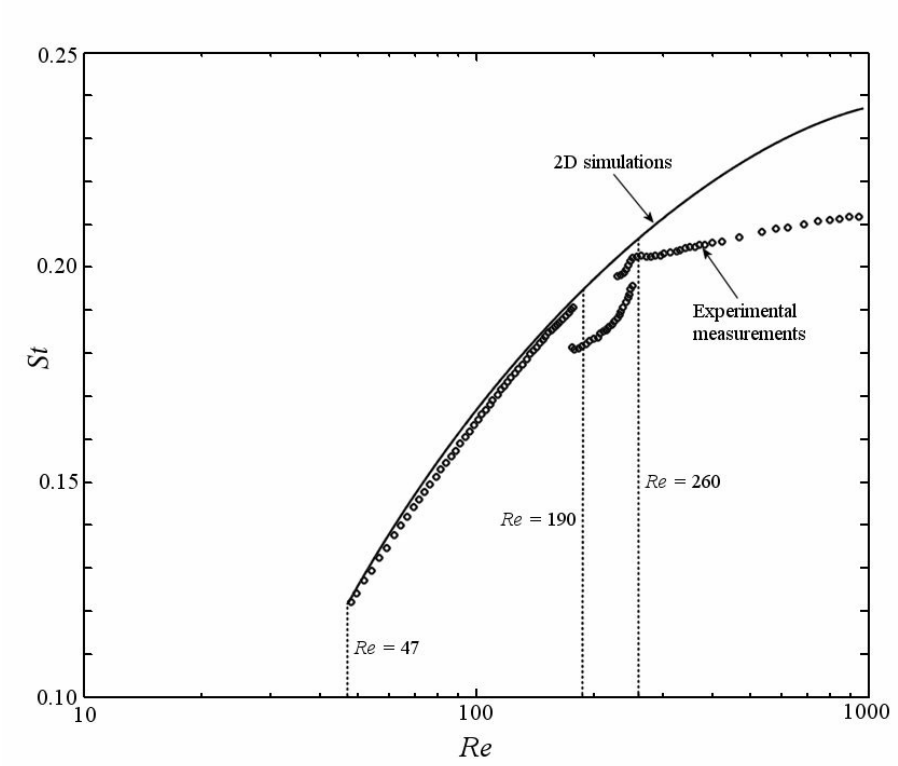

Figure 4.2: Variation of Strouhal number as a function of Reynolds number for 2D and 3D cylinder wake flow (reproduced after Henderson [39]). Notice the significant difference between the 2D simulations and the experimental measurements already at $Re > 190$.

sion (= cylinder length). In flow calculations, periodic boundary conditions are commonly used in the spanwise direction to approximate the flow past an infinitely long cylinder. However, this approximation is not valid unless the spanwise domain size is large enough to represent the continuous spectrum of the infinite problem [39]. Only perturbations with wavelength $\lambda_n = L/n$, where n is an integer, will be present in the solution. According to Henderson, the flow will be perfectly periodic if a single mode (A or B) is present. Two modes will lead to a quasiperodic behavior, where the shedding frequency will alternate between the two modal values. Finally, when three or more modes are amplified, the flow will go into a state of *spatiotemporal chaos,* which eventually leads to turbulence at $Re \approx 1000$. Transition to turbulence starts in the separated shear layers downstream of the cylinder. The point of transition moves upstream as Re increases, but the boundary

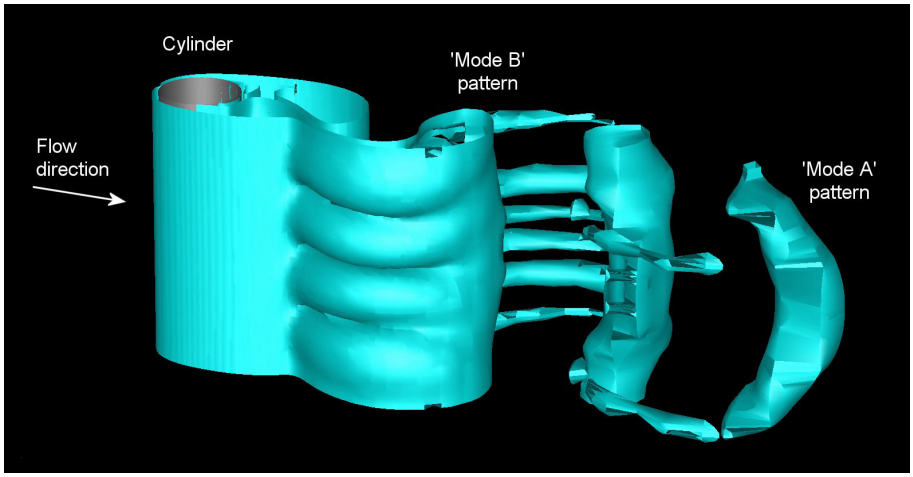

Figure 4.3: Isosurface of the vorticity field (scalar value of the vorticity vector) at $Re = 265$. Results from present study, showing the 3D character of the wake flow. The vorticity value is $|\boldsymbol{\zeta}| = 300$, approx 4% of the maximum value.

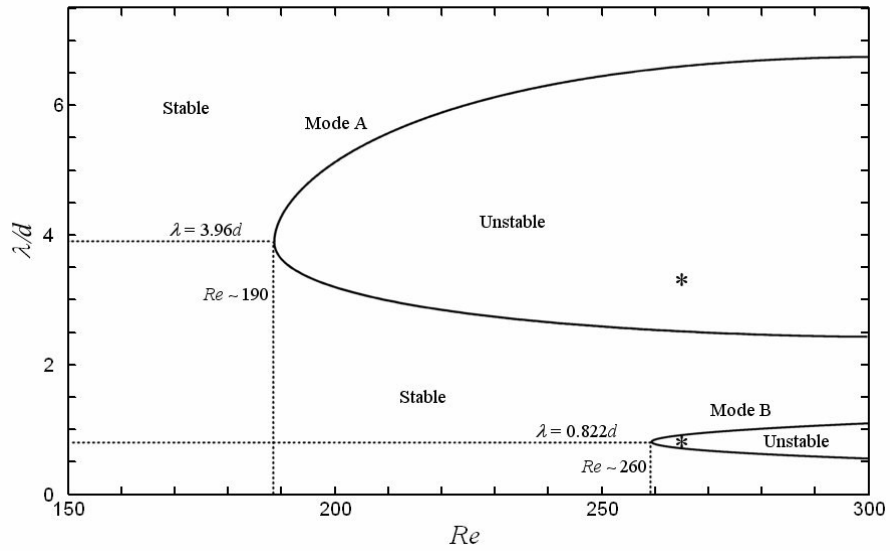

Figure 4.4: Curves of neutral stability with respect to spanwise perturbations. Unstable modes exist in the regions inside the curves (reproduced after Henderson [39]). The two cases considered in section 4.2 are marked with an asterisk ($*$).

layer around the entire cylinder remains laminar until $Re \approx 200{,}000$. Upon a further increase in Re, the flow will go through stages of laminar boundary layer separation and subsequent turbulent re-attachement. This leads to a narrowing of the wake, and a large decrease in drag on the cylinder. At $Re \sim O(10^6)$ the final stage of transition occurs, when the bondary layer on the cylinder becomes turbulent upstream of the separation point. A detailed review of the different flow regimes is given by C.K.H. Williamson [40]. In the present study, detailed calculations of the flow around a single cylinder are performed at $Re = 265$ and $Re = 3900$, and calculations of flow around two cylinders arranged in tandem are carried out at $Re = 21600$ (treated separately in chapter 5).

4.2 Flow around a cylinder at $Re = 265$

4.2.1 Description of the numerical experiment

Numerical simulation of laminar flow around a circular cylinder is performed at $Re = 265$. The Navier-Stokes equations are solved without the use of a turbulence model. Direct numerical simulation (DNS) results reported by Henderson [39] show that the onset of three-dimensionality in the wake, which happens at $Re \simeq 190$, influences the mean surface pressure on the cylinder. Here, the 'mean surface pressure' is defined as the surface pressure averaged in time and along the span of the cylinder. We may define a surface pressure coefficient as

$$C_p \equiv (p - p_\infty)/\frac{1}{2}\rho u_\infty^2 \tag{4.1}$$

where p is the mean surface pressure and p_∞ is the free stream pressure. The three-dimensional behavior causes a reduction in magnitude of C_p on the low-pressure side (or base) of the cylinder, compared to two-dimensional simulations. This will lead to a reduction in mean drag on the cylinder. A comparison of the surface pressure from one 2D simulation and two 3D simulations (ref. Henderson [39]) with different cylinder lengths, $L = 0.822d$ and $3.288d$ respectively, is shown in figure 4.5. Here, $\theta = 0$ is the base of the cylinder, and $\theta = \pm\pi$ is the front stagnation point, see figure 4.6. The Reynolds number of 265 is just above the critical Re for 'mode B'. In Henderson's 3D simulation with the shortest cylinder ($L = 0.822d$), only a single 'mode B' instability is present. In the simulation with the four times longer cylinder, $L = 3.288d$, one 'mode A' and one 'mode B' instability is present. This result can be inferred from the stability diagram on figure 4.4. We will use Henderson's results as benchmark data for the present study (see

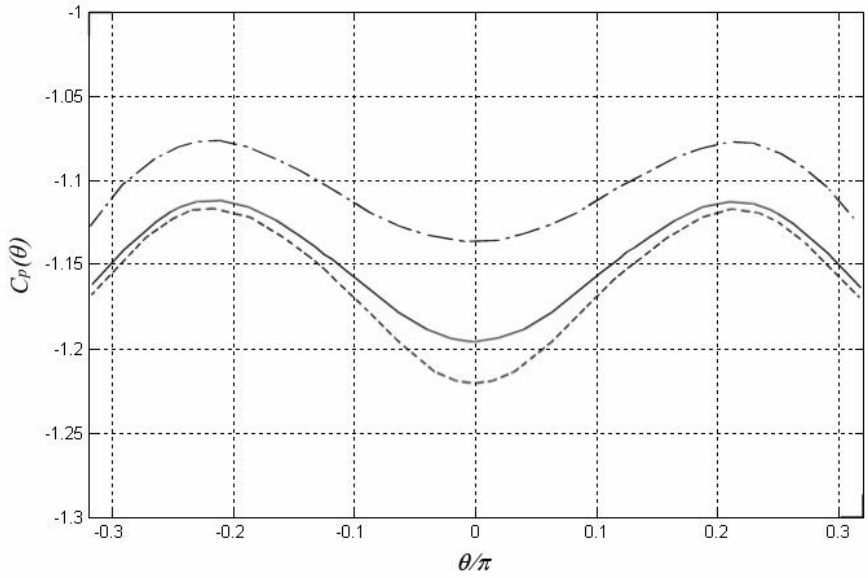

Figure 4.5: Expanded view of the mean surface pressure distribution on the low-pressure side (base) of a circular cylinder at Re = 265 (DNS results by Henderson [39]). Dashed line: 2D simulation. Solid line: 3D simulation with L = 0.822d. Dash-dot: 3D simulation with L = 3.288d.

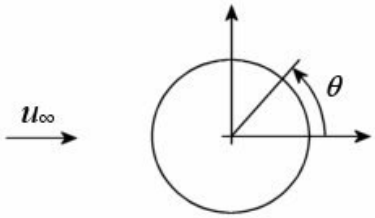

Figure 4.6: Definition of the angular position θ

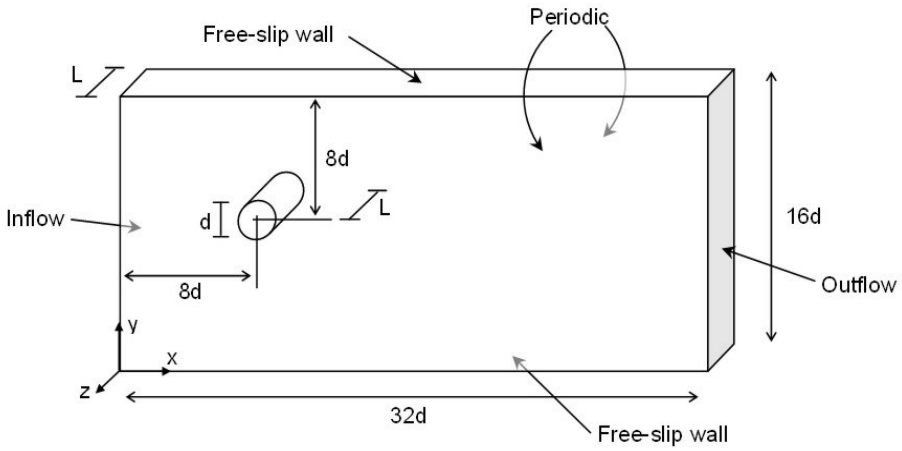

Figure 4.7: Computational domain for the circular cylinder

table 4.3). The two cases considered in the present study are marked with an asterisk ($*$) in figure 4.4.

The computational domain is shown in figure 4.7. The cylinder diameter $d = 0.1$.The centre of the cylinder is placed halfway between the free-slip walls, making the flow domain symmetrical about the x-axis (the ambient flow direction). This can make it difficult to start the vortex shedding when gradually increasing the Reynolds number, because the symmetry tends to reinforce the stability of the low Re solution. A common remedy to this problem is to place the cylinder slightly off centre, thus introducing an asymmetry. In the present case, however, a non-uniform initial velocity field is used to trigger the flow instabilities; both the 2D vortex shedding and the 3D (spanwise) instability. At $t = 0$, the velocity field is described by a linear function in y multiplied by a quadratic function in z (see fig. 4.7 for axis definitions). During a time interval τ after $t = 0$, the inflow and free-slip wall velocities gradually transform into a prescribed constant value of u. This effectively provokes the desired flow behaviour. So, after a time τ the boundary conditions become stationary, with $u = u_\infty = 2.65$ and $v = w = 0$ at the inflow and free-slip wall boundaries. In order to get the prescribed Reynolds number of 265, the viscosity and density are adjusted to suitable values. We have chosen viscosity $\mu = 1{\cdot}10^{-3}$ and density $\rho = 1$.

Periodic boundary conditions are used in the spanwise direction. At the outflow boundary, the pressure is set to zero. Note that $p = 0$ is stricter than the usual homogeneous Neumann condition, which requires zero normal stress. However, using the Neumann condition at the outflow caused some

problems with pressure growth in the corners between the outflow and the periodic boundaries. So, $p = 0$ was chosen instead, in order to avoid these difficulties. The outflow boundary is assumed to be far enough downstream so that the zero pressure condition doesn't influence the pressure on the cylinder surface.

The backward Euler time discretization scheme is used in all the simulations in the present section. This is a first order method, unconditionally stable and known to produce a smooth (non-oscillatory) solution even for very large time steps. Therefore, our main consideration is accuracy when it comes to choosing the time step δt. (However, it should be noted that the use of equal order finite elements in combination with the projection method may lead to instabilities when the time step becomes too small relative to the grid spacing). In order to get accurate results, the physical time scales of interest should be sufficiently resolved, i.e. $\delta t << T_{phys}$. The most significant physical time scale in our case is the vortex shedding period (which is equal to the lift cycle):

$$T_{lc} = \frac{d}{u_\infty \cdot St} \tag{4.2}$$

Based on literature and a number of calculation tests, we estimate that O(100) time steps per vortex shedding cycle is required. A more systematic study of time step sensitivity is performed as part of the experiment, see below.

The numerical experiment consists of the following parts:

1. Cylinder of length $L = 0.822d$

   - Calculations performed on three topologically similar grids, G1 ("coarse"), G2 ("medium") and G3 ("fine"). The goal is to investigate the sensitivity to grid resolution. In this part of the experiment, the time step δt is kept fixed at 0.001, which gives a dimensionless time step $\delta t' = \delta t \cdot u_\infty / d = 0.0265$.
   - Calculations with varying time step performed on one of the grids (G2), in order to investigate time step sensitivity.

2. Cylinder of length $L = 3.288d$

   - Calculations with a longer cylinder, performed on a grid with identical 2D cross sections as grid G2 (but with a different z resolution). The aim here is to study the change in wake flow pattern when the cylinder length is increased.

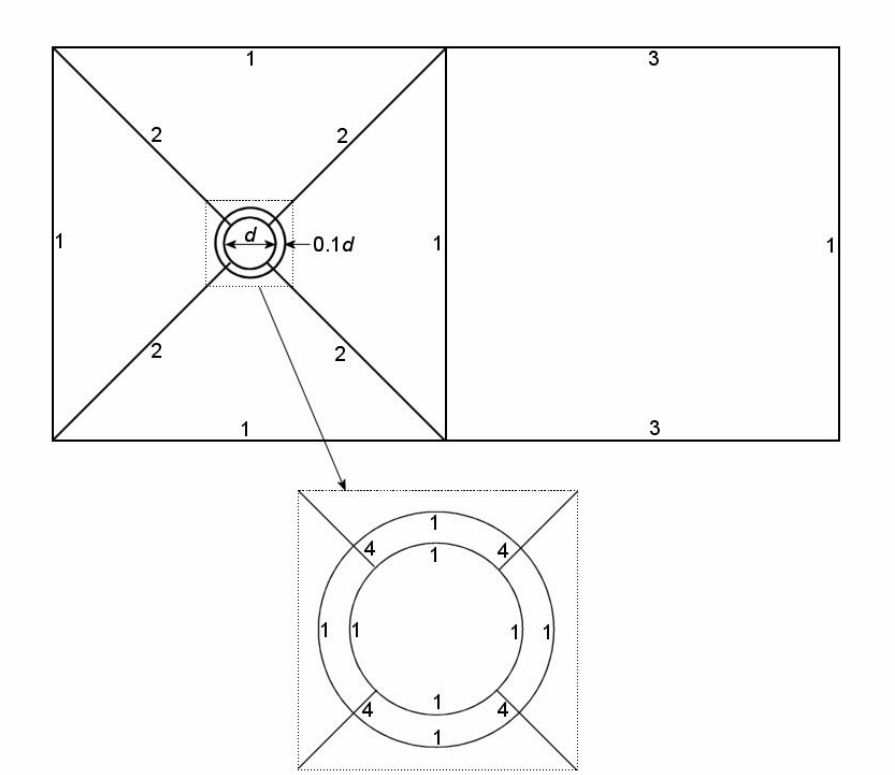

Figure 4.8: Block topology of the grids (schematic view). Number of elements and grading factors for the different curves are given in table 4.1, referring to the numbers 1-4 in the figure.

4.2.2 Cylinder of length $L = 0.822d$

Computational grids

The computational grids used in the simulations are generated using *Griddler* [42], a computer program developed at SINTEF Applied Mathematics. The grids are block structured, with 8 node linear hexahedral elements for both velocity and pressure. The block topology of the grids is shown as a 2D cross section in figure 4.8. The nodes are uniformly spaced in the spanwise (z) direction, and clustered towards the cylinder surface. Four thin "shell blocks" enclosing the cylinder ensures proper control of the gridding in the boundary layer close to the surface. The clustering (grading) of nodes is done as "evenly" as possible, in order to avoid any large jumps in element size, which may cause numerical difficulties. See figure 4.9 and 4.10. Data for the

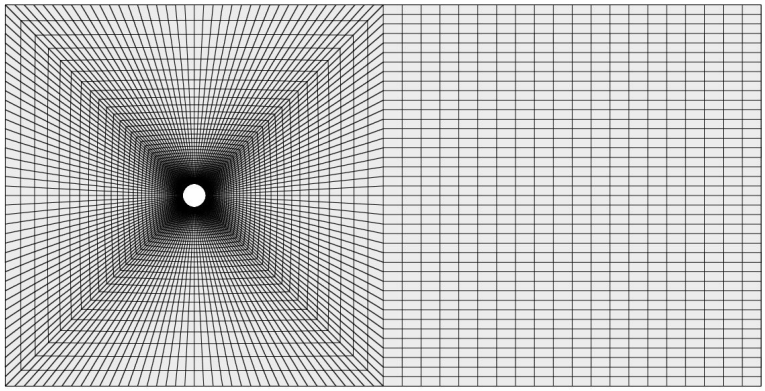

Figure 4.9: The coarsest grid, G1 (ref. table 4.1)

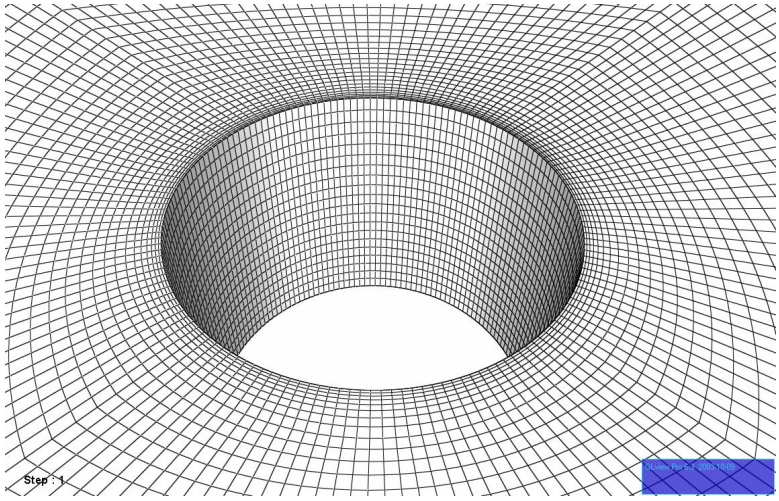

Figure 4.10: Close-up view of grid G1.

Grid:	G1	G2	G3
Total no. of nodes	181860	365202	719136
No. of nodes in the xy plane	8660	13526	22473
Total no. of elements	169600	345800	688128
Elem. thickness at the cyl. surface, % of d	0.577	0.464	0.388
No. of spanwise elements	20	26	32
No. of elem. along curves marked 1 and 2	40	50	64
No. of elem. along curves marked 3	20	26	32
No. of elem. along curves marked 4	8	10	12
Grading factor, curves marked 1 and 3	1	1	1
Grading factor, curves marked 2	32	32	32
Grading factor, curves marked 4	4	4	4

Table 4.1: Grid data, cylinder of length L=0.822d. Curve numbers refer to figure 4.8. The grading factor is the ratio between the largest and smallest element along the curve. A grading factor of 1 means that no grading is used; all elements have equal length. Whenever grading is used, the nodes are clustered towards the cylinder surface, see figures 4.9 and 4.10

grids covering the computational domain (shown in figure 4.7) are given in table 4.1. (In this case, detailed data are provided for future reference). The coarsest grid (G1) is uniformly refined throughout the domain, in order to produce the medium fine grid (G2). A refinement factor of approximately $2^{\frac{1}{3}}$ is used along each curve defining the grid. Consequently, G2 has approximately twice as many nodes as G1. The same refinement is used from G2 to G3, so that G3 has ca. twice as many nodes as G2. In order to get accurate results, the grid spacing in the wall-normal direction near the cylinder surface should be small enough to capture the most important features of the boundary layer. As a rule of thumb, the boundary layer thickness is often taken to be $O(d/\sqrt{Re})$. According to this measure, the grids in the present study have between 5 and 10 elements inside the boundary layer, which should be sufficient resolution.

Simulation setup

An overview of the individual runs performed in this experiment are shown in table 4.2. The first column of table 4.2 constitutes a "grid convergence" test, while the second row makes a "time step convergence" test. Each time series are run for 3 seconds, i.e. 3000 time steps when $\delta t = 0.001$, 1500 when $\delta t = 0.002$ etc.

Grid	$\delta t = 0.001$	$\delta t = 0.002$	$\delta t = 0.004$
G1	x		
G2	x	x	x
G3	x		

Table 4.2: Overview of simulations with cylinder of length L=0.822d and Reynolds number Re=265

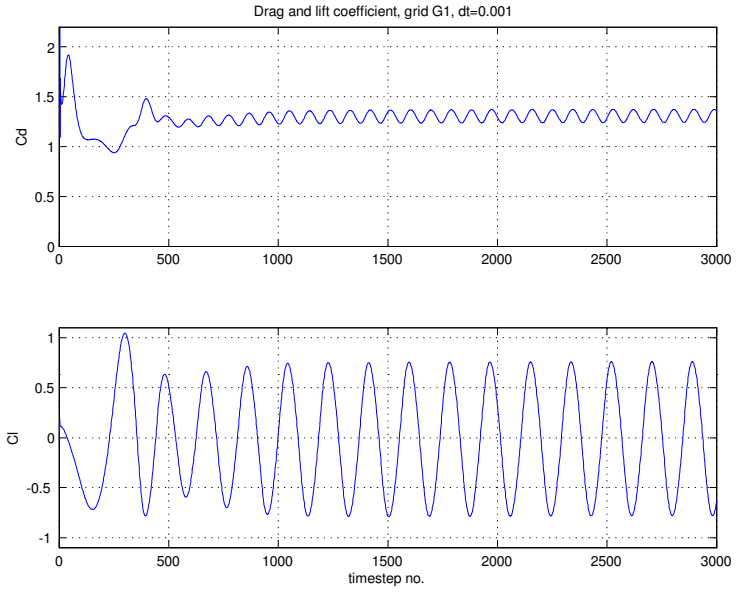

Figure 4.11: Drag and lift coefficient, grid G1, $\delta t = 0.001$.

Results overview

The fluctuating drag and lift coefficients as a function of time for the simulation with grid G1 and $\delta t = 0.001$ is shown in figure 4.11. Time histories of drag and lift from the other runs in table 4.2 are shown in appendix A.1. The drag and lift coefficient are defined as

$$C_D = \frac{F_x}{\frac{1}{2}\rho u_\infty^2 L d} \qquad and \qquad C_L = \frac{F_y}{\frac{1}{2}\rho u_\infty^2 L d} \tag{4.3}$$

(See figure 4.7 for further definitions.) The drag and lift time histories look quite similar in all the runs. It takes about 1 sec. of "physical" time to reach a time-periodic state, regardless of time step. Flow visualizations show that the 'mode B' instability is present in all the runs. An example is shown in figure 4.12.

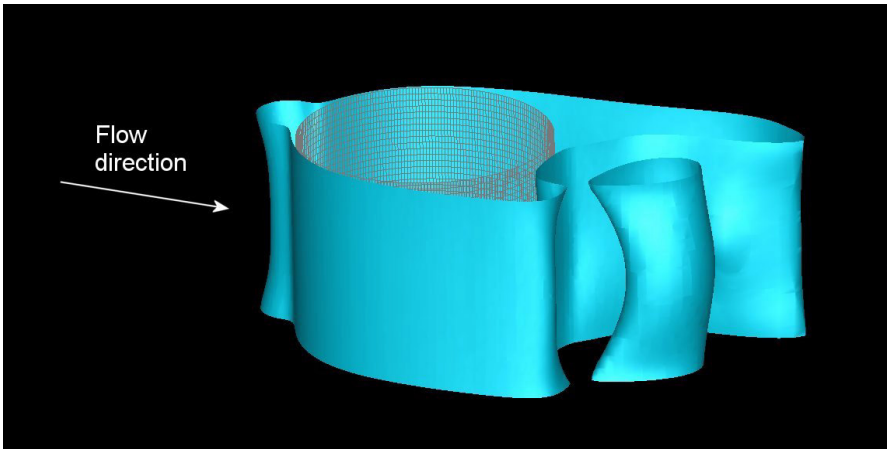

Figure 4.12: Isosurface of the velocity field, grid G3, $\delta t = 0.001$. The 'mode B' pattern can be seen as a sinusoidal spanwise variation of the velocity field.

The most important flow parameters (from the perfectly time-periodic part of the calculations) are shown in table 4.3, together with reference values. 2D reference values are also included, and we see that both the 2D Strouhal number and pressure coefficients are slightly higher than the 3D reference values. Subscript *"PtP"* denotes "peak-to-peak", defined as the difference between max and min values. Note that the peak-to-peak value is unique only when the time series is perfectly periodic, as in the present case. Otherwise, the standard deviation should be used as a measure of the level of fluctuation. C_{p0} is the mean base pressure coefficient (the pressure coefficient at $\theta = 0$), and C_{pmin} the mean lowest value of C_p. The definition of the pressure coefficient C_p is given in the previous section. The instantaneous pressure on the cylinder surface is collected from two full lift cycles towards the end of each simulation, approx. 100 time steps per lift cycle, forming the basis for the calculation of the mean pressure distribution. The Strouhal number St is calculated directly from the mean zero crossing period of the lift coefficient.

Grid convergence test

A comparison of the pressure distribution on the cylinder for the cases with $\delta t = 0.001$ and different grids is shown on figure 4.13, together with 3D reference data (circles). The base pressure coefficient C_{p0} is plotted against the total number of nodes, together with the reference value (dash-dotted line) in figure 4.14. From figure 4.13 we see that the general shape of the pressure curves is well reproduced, and also the position of minimum pressure. As the

Data from:	St	C_D	$C_{D,PtP}$	$C_{L,PtP}$	C_{pmin}	C_{p0}
G1, $\delta t = 0.001$	0.205	1.308	0.138	1.550	-1.530	-1.185
G2, $\delta t = 0.001$	0.205	1.289	0.133	1.473	-1.505	-1.140
G2, $\delta t = 0.002$	0.197	1.281	0.139	1.560	-1.479	-1.136
G2, $\delta t = 0.004$	0.185	1.260	0.137	1.564	-1.441	-1.110
G3, $\delta t = 0.001$	0.205	1.263	0.109	1.338	-1.477	-1.079
Ref. 3D	0.202 (1)	-	-	-	-1.560 (2)	-1.195 (2)
Ref. 2D	0.207 (2)	-	-	-	-1.580 (2)	-1.210 (2)

Table 4.3: Flow parameters from present DNS and reference data; (1) Experiment by Williamson [40], (2) Simulations by Henderson [39].

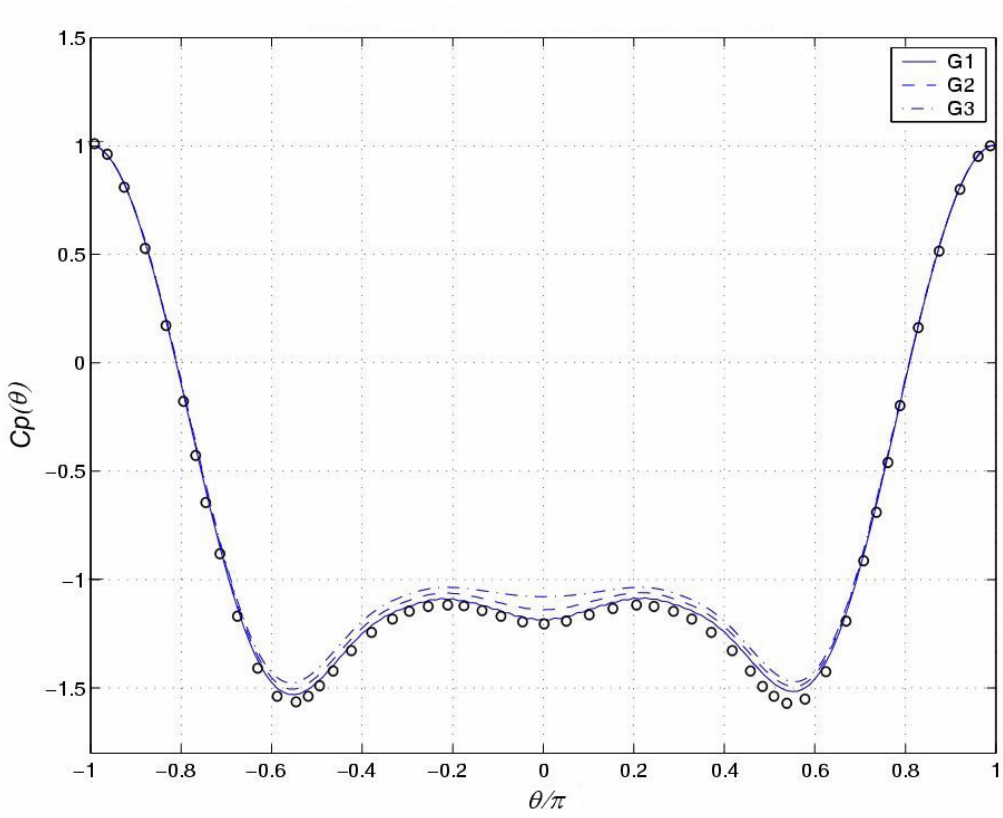

Figure 4.13: Mean pressure distribution on the cylinder surface, three different grids with fixed time step $\delta t = 0.001$. Circles (○) mark the reference values from Henderson [39] (3D).

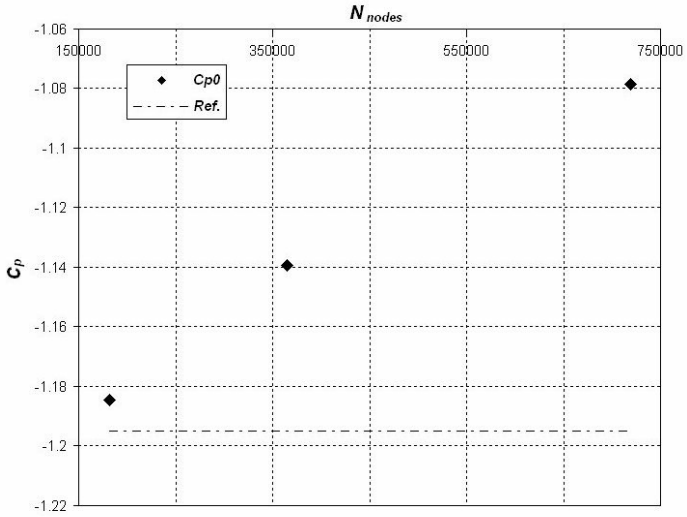

Figure 4.14: Comparison of base pressure coefficient C_{p0} with reference value from [39], grid convergence test

grid is refined, the pressure level around the rear of the cylinder increases (i.e the "base suction" decreases), and consequently the mean drag decreases (see table 4.3). This trend is consistent with resolving more and more of the three-dimensional physics of the wake. The results also indicate that the VISTA code converges towards a different level of mean surface pressure than the code used by Henderson, i.e. our results depart from Henderson's, when the grid is refined. This may be attributed to the different computational methods chosen in the two codes. Henderson uses a very accurate, high order spectral element method. However, further refinement studies are needed to confirm this trend. Also, we may notice a reduction in peak-to-peak values as the grid is refined. This indicates that force oscillations become smaller as more of the 3D physics is resolved.

An error estimate of the base pressure coefficient may be taken as

$$err = \frac{|C_{p0}^{calc} - C_{p0}^{ref}|}{|C_{p0}^{ref}|} \tag{4.4}$$

According to this estimate, the error will thus increase with increasing node number, see figure 4.15, and a possible reason for this is mentioned above. Obviously, the error shows exactly the same trend as figure 4.14. We may note that the error is below 10 % in all the runs. This is a quite satisfactory result, and in any case good enough for engineering purposes.

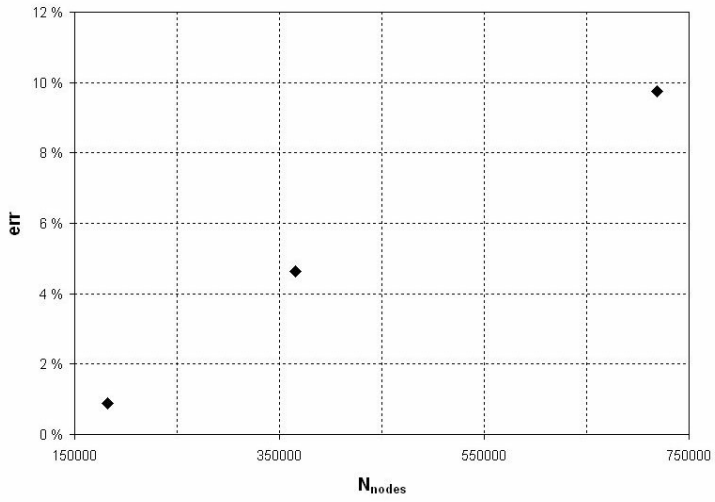

Figure 4.15: Error in base pressure coefficient C_{p0} relative to the reference value from [39], grid convergence test

Time step convergence test

A comparison of the pressure distribution on the cylinder for the cases with grid G2 and three different time steps is shown on figure 4.16, together with the reference data. The general shape of the curves and the position of minimum pressure is well reproduced, as in the grid convergence test. However, decreasing the time step seems to have the opposite effect as refining the grid. Indeed, our pressure distribution curve approaches the reference curve when the time step becomes smaller, but at the same time we approach the 2D solution (the dashed curve in figure 4.5). We would expect the same trend when decreasing the time step as we observed when refining the grid. As this is not the case, we should make further investigations. Consequently, an additional calculation is done on the same grid, one with $\delta t = 0.0005$ (i.e. halving the shortest time step). The resulting pressure distribution is plotted in figure 4.17, together with the $\delta t = 0.001$ curve. We see that the curves lie very close together. The blue curve ($\delta t = 0.0005$) lies just below the red curve ($\delta t = 0.001$) on most of the rear side of the cylinder ($|\frac{\theta}{\pi}| \lesssim 0.5$). Only at the base itself the blue curve barely crosses the red one. Thus, the trend is somewhat inconclusive in this case. Upon close inspection, we may notice that the blue curve isn't perfectly smooth, but has a slight 'saw-tooth' pattern. A magnified view is shown in figure 4.18. A similar but less distinct pattern is also present in the pressure distribution for the

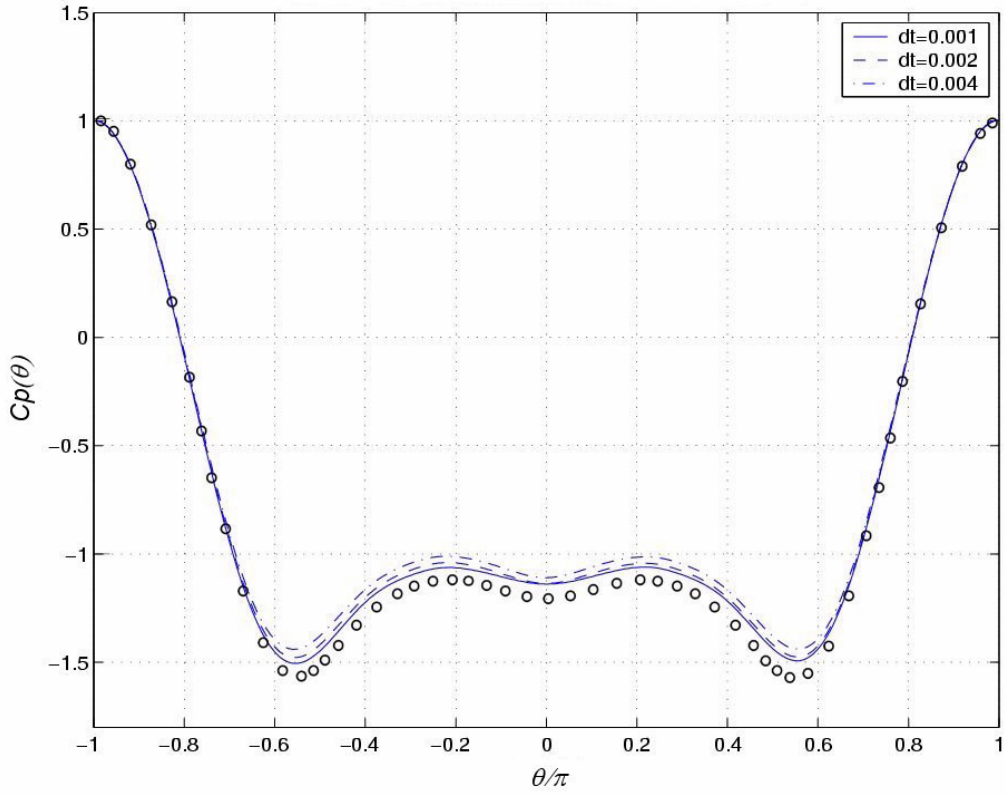

Figure 4.16: Mean pressure distribution on the cylinder surface, grid G2 with three different time steps. Circles (○) mark the reference values from Henderson [39] (3D).

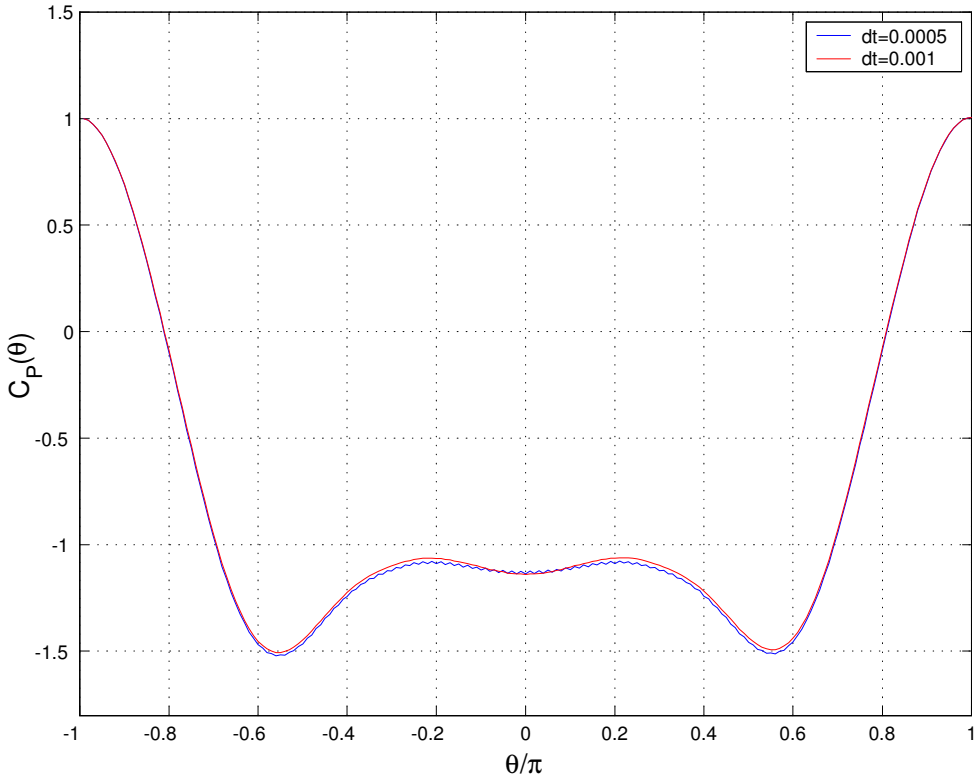

Figure 4.17: Mean pressure distribution on the cylinder surface. Grid G2 with two different time steps, $\delta t = 0.0005$ (blue) and $\delta t = 0.001$ (red)

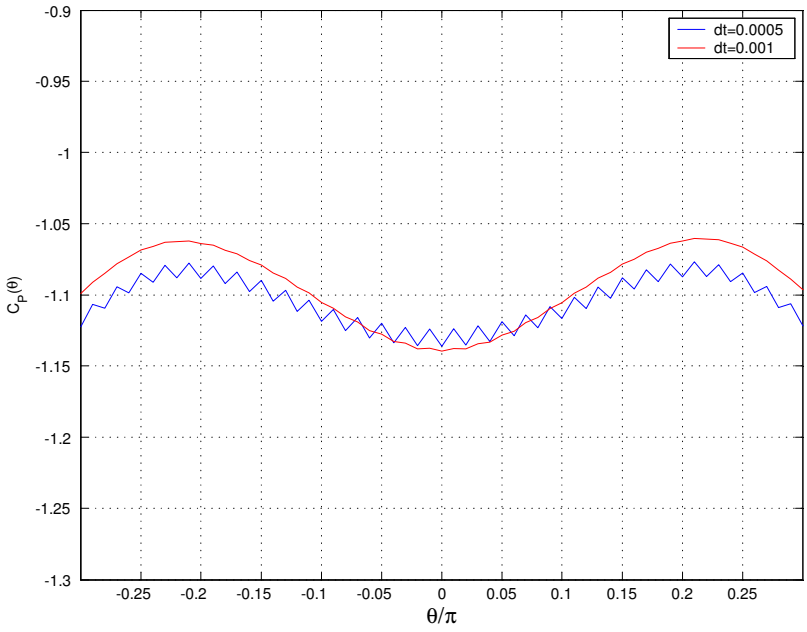

Figure 4.18: Magnified view of the mean pressure distribution shown in figure 4.17. Grid G2 with two different time steps, $\delta t = 0.0005$ (blue) and $\delta t = 0.001$ (red)

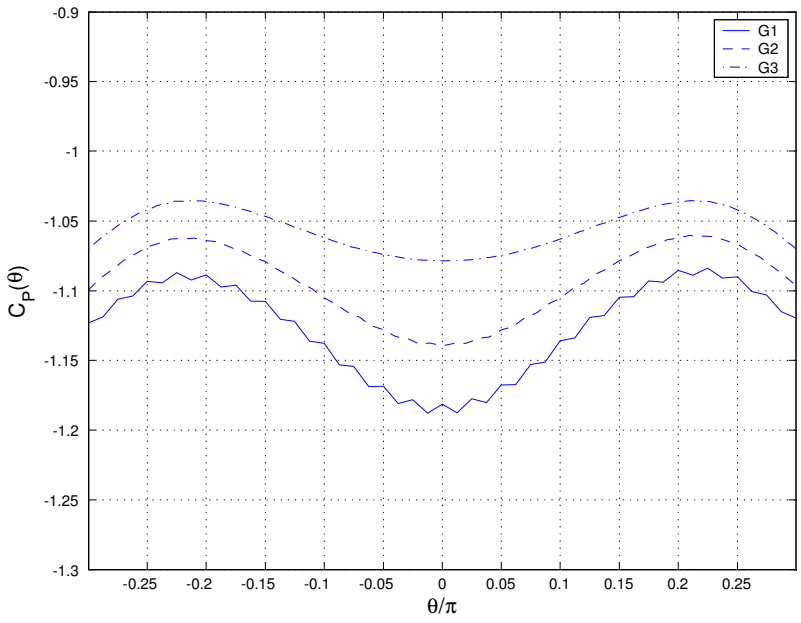

Figure 4.19: Magnified view of the mean pressure distribution shown in figure 4.13, three different grids with fixed time step $\delta t = 0.001$.

coarser G1 grid with $\delta t = 0.001$. It's difficult to see in figure 4.13, but becomes apparent when we magnify pressure distribution, see figure 4.19 (note: the reference data (circles) in figure 4.13 are not plotted in figure 4.19). The base pressure coefficient C_{p0} for all the four runs is plotted against the time step together with the reference value (dash-dotted line) in figure 4.20. From this figure it appears that the optimal time step for this particular grid is somewhere between 0.001 and 0.002. In general, decreasing the time step will lead to a smaller discretization error. This error is $O(\delta t)$ for the backward Euler method. However, errors due to the operator splitting will also become smaller as we decrease the time step. The splitting error (see equation 3.4) has a stabilizing effect on the solution, which is important when we use equal order (linear) elements for velocity and pressure, as we do in this numerical experiment. When the time step becomes very small, we will lose this stabilization. Eventually, our solution will be destroyed. This can explain the saw-tooth pattern mentioned above. A similar saw-tooth pattern also appeared when we used a larger time step on the coarsest grid. This means that the error due to the operator splitting is a function of the grid spacing as well as the time step.

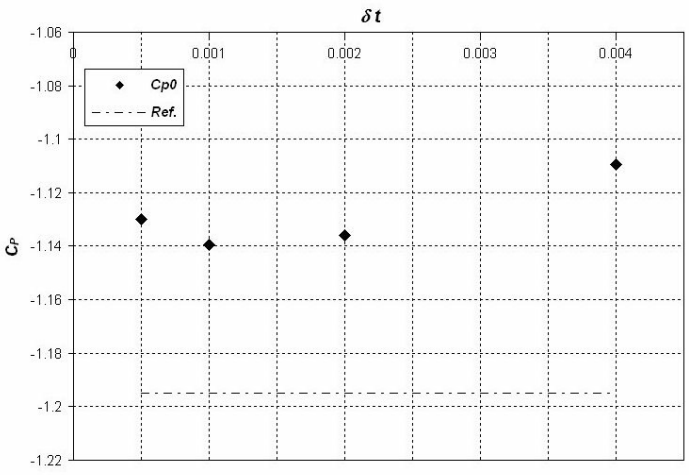

Figure 4.20: Comparison of base pressure coefficient C_{p0} with reference value from [39], time step convergence test

Conclusions

Our findings in the first part of this numerical experiment are summarized below:

- A single 'mode B' instability is present in our calculations of flow around a cylinder of length $L = 0.822d$ and $Re = 265$.
- The general shape of the mean pressure distribution on the cylinder surface is well reproduced in the calculations, and also the position of minimum pressure, compared to the reference results.
- The VISTA code seems to converge towards a different pressure distribution than the reference solution when the grid is refined, but further refinement studies are needed to confirm this.
- For any particular grid, there exists an optimal time step for which the error is minimal. If the time step is decreased beyond this optimum, we will lose stabilization. When linear elements are used for both velocity and pressure, the loss of stabilization will eventually destroy the solution.
- The stabilization also depends on the grid spacing. The finer grid, the smaller time step can be used without losing stabilization.

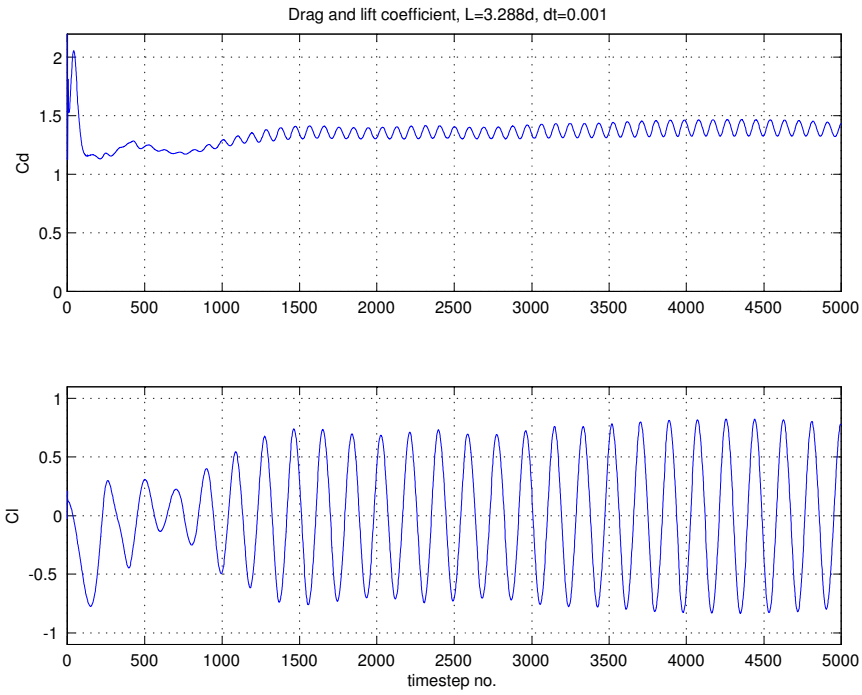

Figure 4.21: Time series of drag and lift coefficient, $L = 0.3288d$, δt= 0.001.

4.2.3 Cylinder of length $L = 3.288d$

General remarks

In this part of the numerical experiment, a calculation is performed on a single computational grid, and with one time step, $\delta t = 0.001$. The simulation is run for 5000 time steps. The grid is based on grid G2 from the previous section. It has the same 2D cross section as G2, but only 56 elements in the z-direction, whereas G2 had 26. The cylinder is now four times longer; so ideally there should be 4 x 26 = 104 elements in the z-direction in order to make a direct comparison with the results from G2. However, some software limitations at the time of the calculations made it necessary to reduce the problem size somewhat. The total number of nodes in the new grid is 770982. The purpose of this part of the experiment is to study the change in wake flow pattern when the cylinder length is increased.

Results and discussion

The drag and lift history is shown in figure 4.21. We observe that the simulation does not reach a perfectly time-periodic state; there is a slight variation

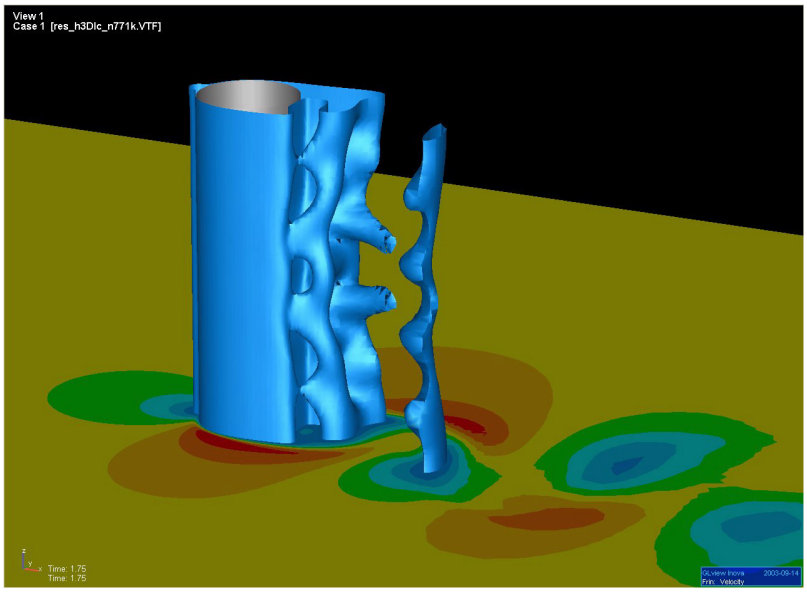

Figure 4.22: Isosurface of the velocity field. We may observe four repetitions of the pattern shown in figure 4.12 along the span of the cylinder.

in mean drag, and a variation in amplitude of both lift and drag. This is consistent with observations made by Henderson [39], where the flow enters a quasi-periodic state with mixed mode A and B patterns at $Re = 265$ and $L = 3.288d$.

Figure 4.22 illustrates the characteristic 3D spanwise variation of the velocity associated with the 'mode B' instability. We can clearly recognize the pattern shown in figure 4.12 for the short cylinder ($L = 0.822d$), but now repeated four times along the span of the cylinder.

Figure 4.23 shows the development of the Strouhal number's relative change from the mean value, starting at time step 1500 when the startup transient has died out (see figure 4.21). Interestingly, St seems to vary within a group of five distinct values. This is similar to the behaviour demonstrated by Henderson [39]. However, the simulation time in the present calculation is too short to draw any definitive conclusions regarding drag, lift and Strouhal number variations.

Vorticity isosurfaces at two different times are shown in figure 4.24, the first one after approx. 2000 time steps (top), and the second after approx. 4900 time steps (bottom). The grid lines at the centre plane is also shown. Both snapshots are taken at the same phase within the oscillation cycle, and the same vorticity value, $|\boldsymbol{\zeta}| = 300$, is represented in both cases. $|\boldsymbol{\zeta}| = 300$

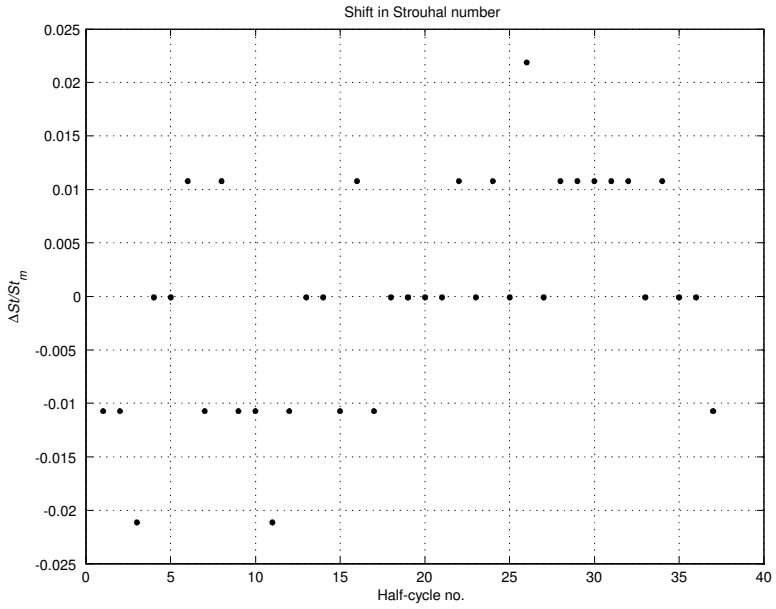

Figure 4.23: Relative change in St as a function of lift half-cycle number, starting at time step no. 1500 (ref. fig. 4.21).

is about 4% of the maximum vorticity at the give time steps.

After 2000 time steps we clearly see that both the 'mode A' (long wavelength) and 'mode B' (short wavelength) pattern is present. At the later time, however, the 'mode B' pattern seems to have disappeared. This may be due to the bi-modal behaviour of the flow, in which case we would expect the 'mode B' pattern to reappear later in the simulation. In order to demonstrate this, however, we would require a considerably longer simulation time. Another possible explanation is that the grid resolution in the spanwise direction is insufficient, having the effect that the shortest wavelengths are damped out after some time.

The pressure distributions corresponding to the two flow situations shown in figure 4.24 are shown in figure 4.25. Here we observe a pressure drop around the base of the cylinder when the 'mode B' pattern is no longer present. This change in pressure is consistent with going to a more two-dimensional flow behaviour, also shown by Henderson [39] (see also figure 4.5). Also, we may notice a slight increase in drag and lift amplitudes starting around time step 3000, see figure 4.21.

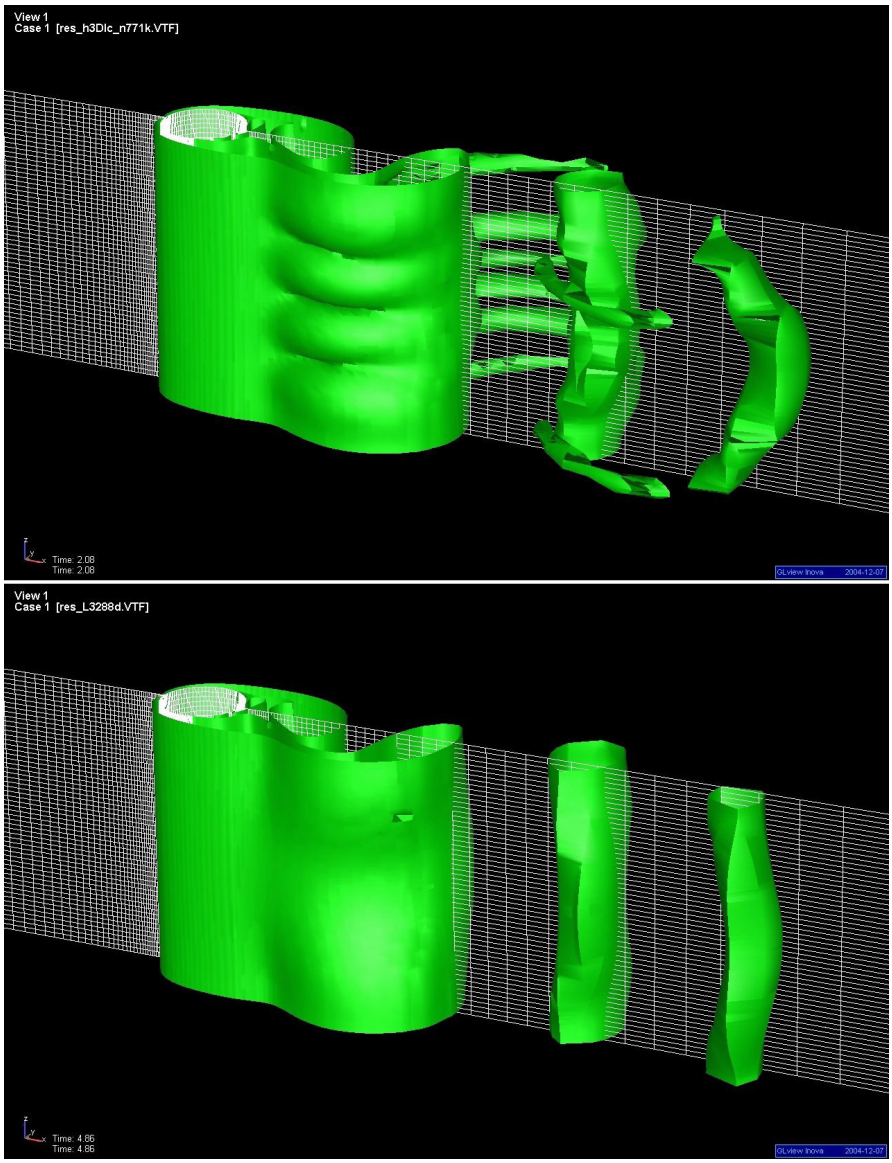

Figure 4.24: Vorticity isosurface with value $|\boldsymbol{\zeta}| = 300$ after approx. 2000 time steps (top) and 4900 time steps (bottom). Notice how the 'mode B' pattern present after 2000 time steps seems to have disappeared after 4900 time steps.

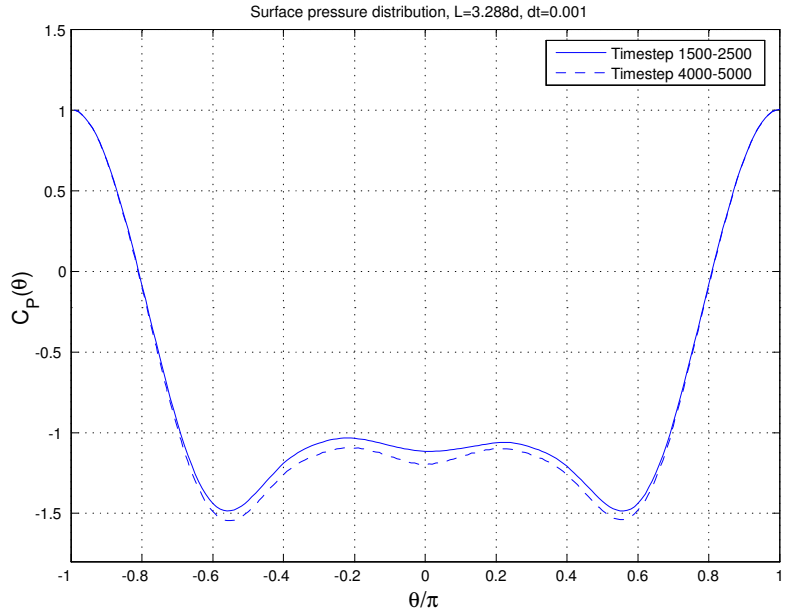

Figure 4.25: Pressure distribution from two different intervals: Timestep 1500-2000 (solid line, corresponding to the situation at the upper half of figure 4.24), and timestep 4000-5000 (dotted line, corresponding to the lower half of figure 4.24). Notice that there is less three-dimensionality in the lower half of figure 4.24 than in the upper half. The corresponding difference in pressure distribution is consistent with results from Henderson [39], see figure 4.5.

Conclusions

The findings in the second part of the experiment can be summarized as follows:

- Both 'mode A' and 'mode B' instabilities are present in our calculation of the flow around a cylinder of length $L = 3.288d$ and $Re = 265$.
- The flow does not reach a perfectly time-periodic state as in the case of the short ($L = 0.822d$) cylinder. There are slight variations in mean drag, amplitudes of lift and drag, and also Strouhal number, during the course of the simulation. This is linked to the bi-modality of the flow.
- Towards the end of the simulation, the shortest wavelength pattern ('mode B') is no longer present. The corresponding surface pressure distribution shows a drop around the base of the cylinder, consistent with a more two-dimensional flow behaviour. The simulation time is too short to determine whether the disappearence of the 'mode B' pattern is a characteristic of the flow itself, or if it's due to insufficient grid resolution in the spanwise direction.

4.3 Flow around a cylinder at $Re = 3900$

4.3.1 Description of the numerical experiment

Large-eddy simulation (LES) of turbulent flow around a circular cylinder is performed at $Re = 3900$. Flow around a cylinder at $Re = 3900$ has become a benchmark case for numerical simulation of subcritical/transitional flows. This is mainly due to the particle image velocimetry (PIV) experiments performed by Lourenco and Shih [45], and later also hot wire experiments by Ong and Wallace [46]. At $Re = 3900$ the cylinder flow is characterized by laminar boundary layer separation, with transition to turbulence happening somewhere in the wake. The flow is more complex and 'chaotic' now than in the previous cases at $Re = 265$, but still the two-dimensional large-scale vortex shedding is a dominating feature, see figure 4.26.

The computational domain is identical with the one used in the previous case with $Re = 265$ and $L = 3.288d$, see figure 4.7. Thus, the Reynolds number is the only flow parameter which has changed. Other authors have used $L = \pi d$, e.g [43], [44], but for the sake of comparison with the lower Re calculations, $L = 3.288d$ is chosen here. Similar initial and boundary conditions are used, but now with $u_\infty = 3.9$ and $\mu = 1{\cdot}10^{-4}$ (the density remains unchanged). In order to initiate the turbulent behaviour of the flow,

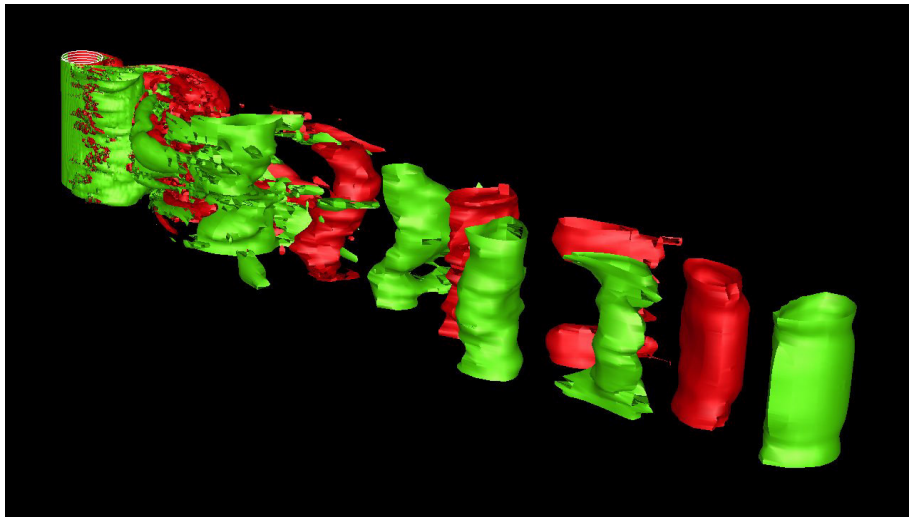

Figure 4.26: Isosurfaces of instantaneous spanwise vorticity, $\zeta_z = 200$ (green) and $\zeta_z = -200$ (red). Results from present study.

Description	Value
L/d	3.288
Total no. of nodes	1079960
No. of nodes in the xy plane (2D cross-sections)	22040
Total no. of elements	1044480
No. of circumferential elements	240
No. of spanwise elements	48
Element thickness at the cylinder surface, % of d	0.12

Table 4.4: Data for grid used in LES at Re=3900

1% white noise is added at $t = 0$. The grid topology and element type (8 node linear hexahedral elements for both velocity and pressure) is also the same, however, a somewhat finer grid is used in the present case. Key data for the grid are given in table 4.4. As in the previous grids, the nodes are clustered towards the cylinder surface, and evenly spaced in the spanwise direction. In addition, there is a moderate clustering in the tangential direction towards $\theta = \pm\pi/2$ (see figure 4.6) in order to increase the resolution in the separation region, and also some clustering towards $\theta = 0$ throughout the wake.

In this numerical experiment, the effect of using van Driest wall damping and the influence of changing the time integration scheme is examined. Three simulations are performed, see table 4.5. Here, TE denotes the trapezoid rule combined with a modified Euler method (referred to as trapez/Euler in the

Case	Time integration scheme	Van Driest damping
1	TE	yes
2	BE	yes
3	BE	no

Table 4.5: Overview of simulations, LES at Re=3900. TE: Trapez/Euler, BE: Backward Euler.

Data from:	St	$\overline{C_D}$	L_r/d
Case 1	0.205	1.134	1.226
Case 2	0.202	1.148	1.024
Case 3	0.214	1.070	1.258
Experiment	0.21±0.005 (1)	0.99±0.05 (2)	1.18±0.05 (3)

Table 4.6: Mean flow parameters, Re=3900. Lr: Recirculation length. Exp. data: (1) Ong/Wallace, (2) Norberg, (3) Lourenco/Shih (in ref. [43])

following). Trapez/Euler is a second order implicit method (apart from one approximation, see Holmen [36]). BE is the backward Euler method, first order implicit. All the calculations are performed on the same grid, with time step $\delta t = 0.001$. The simulations are run for 2000 time steps. It should be noted that an attempt was made with trapez/Euler and no wall damping, but this turned out to be unstable to the extent that the solution was destroyed. Flow statistics was accumulated over approximately 10-12 vortex shedding cycles (see figure 4.27), corresponding to 50-60 dimensionless time units, tu_∞/d.

4.3.2 Results and discussion

The Strouhal number, mean drag, and recirculation length from the present LES runs are given in table 4.6, together with experimental data, cited from Kravchenko and Moin [43]. The experimental data originate from different studies, since not all experiments provide all the flow parameters of interest. The recirculation length L_r is measured from the back of the cylinder.

The Strouhal number agrees very well with experimental result, while the mean drag is overpredicted in all the calculations. As noted in section 4.2, the three-dimensional behaviour of the flow leads to a reduction of base pressure and mean drag compared to 2D flow simulations. A restriction of the spanwise domain size will also restrict the 3D behaviour, and may lead to an increase in mean drag. This could explain the overprediction in the present case, where the cylinder is relatively short. However, further simulations with

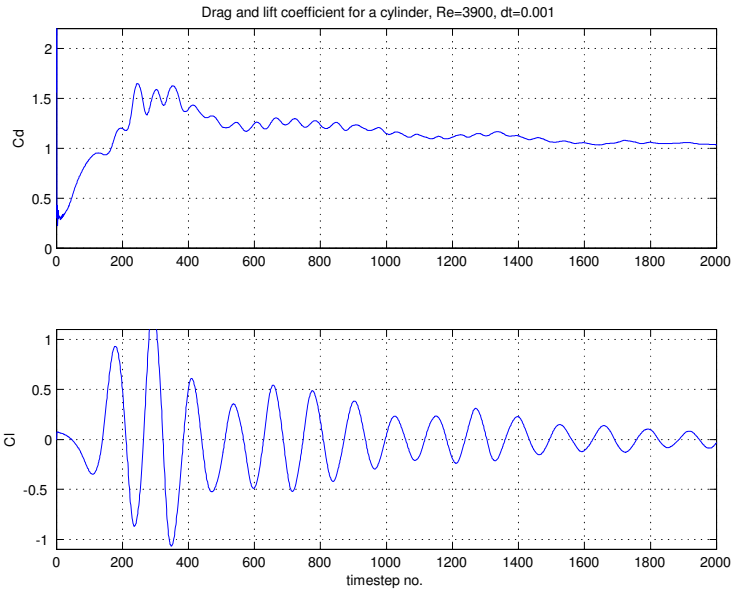

Figure 4.27: Drag and lift coefficient, Trapez/Euler with van Driest wall damping (Case 1).

varying cylinder length would be needed to confirm this. The recirculation length is in good agreement with the experiment in case 1 and 3, whereas it is somewhat underpredicted in case 2.

The time history of drag and lift from case 1 is shown in figure 4.27. The corresponding figures from case 2 and 3 are shown in appendix A.2. It is evident that the flow is quasi-periodic, still with the primary vortex shedding as the dominating feature, but there also seem to be some variation of the force amplitudes. However, the simulation time is too short to demonstrate whether these variations are quasi-periodic or have a more stochastic nature. The drag and lift shows a similar progress in all the three cases, but in case 2 the oscillation amplitudes are noticeably larger in the first part of the simulation than the two other cases.

The mean streamwise velocity along the centreline is shown in figure 4.28. Firstly, we may note that the curve from the experiment by Lourenco & Shih behaves a bit oddly in the interval $x/d = 2.5$ to 4.5. None of the present simulations show this behaviour, nor do simulations by other authors ([43], [44]). Also, the velocity should be exactly zero at the back of the cylinder, however, the data are taken "as is" from Tremblay et al [44], since the original data were unavailable. The position of minimum velocity, as well as the size of the resirculation zone, agree well with the experiment in case 1 and 3.

However, the minimum value of u itself doesn't quite match in either case. Also, the curves in case 1 and 3 has a change in slope very close to the cylinder, which is not present in the experiment by Ong & Wallace [46]. The slope seems to be better predicted in case 2, but here the position of minimum value is a bit too close to the cylinder surface. In the far wake, case 1 is in best agreement with the experiment by Loureco & Shih [45].

Figures 4.29 to 4.31 show mean streamwise velocity profiles at three locations in the wake. On figure 4.29, we observe that case 2 is in exellent agreement with the experiment in the very near wake at $x/d = 1.06$, apart from the minimum value of u at the centreline. Case 2, as well as the experiment, show V-shaped profiles at $x/d = 1.06$, while case 1 and 3 show more U-shaped profiles at this position. At $x/d = 1.54$, all three cases show V-shaped profiles, similar to the experiments, but here the results are more scattered near the centreline. An interesting observation in figure 4.29 and 4.30 is that case 2 show good agreement with the experiment also at the wake boundaries (outside the U/V shape itself, $|y/d| \gtrsim 0.75$), whereas the velocity in case 1 and 3 is too high in these regions. At the far wake position, $x/d = 7.0$, agreement with the experiment is fair, however, the results are generally more scattered.

As we have seen, the overall agreement between the simulation results and the experimental data is good. However, looking at all the results in connection, the effects of interchanging time discretization scheme and turning on and off the van Driest damping can be seen more clearly. Case 1 and 3 may be regarded as permutations of case 2. In case 1, the time discretization scheme is changed from backward Euler to trapez/Euler, and in case 3, wall damping is turned off. In the near wake, these two separate changes (from case 2 to case 1 and 3 respectively) appear to have a qualitatively similar effect. In both case 1 and 3 we observe a change in slope of the centreline streamwise velocity very close to the cylinder, along with an increase of the resirculaton length. Also, the streamwise velocity profile at position $x/d = 1.06$ changes from a near V-shape in case 2 to a more pronounced U-shape in case 1 and 3. However, Tremblay et al [44] point out that the shape of the streamwise velocity profile is closely related to the relative position within the recirculation region. In case 2, $x/d = 1.06$ corresponds to a position immidiately downstream of the point of minimum streamwise velocity, while in case 1 and 3, $x/d = 1.06$ is just upstream of the point of minimum streamwise velocity, see figure 4.28. This means that the wake in case 2 has developed further at position $x/d = 1.06$ than in case 1 and 3, and this may account for the difference in shape.

It is difficult to give a perfectly good explanation for the observed differences between the three cases. The time discretization schemes have slightly

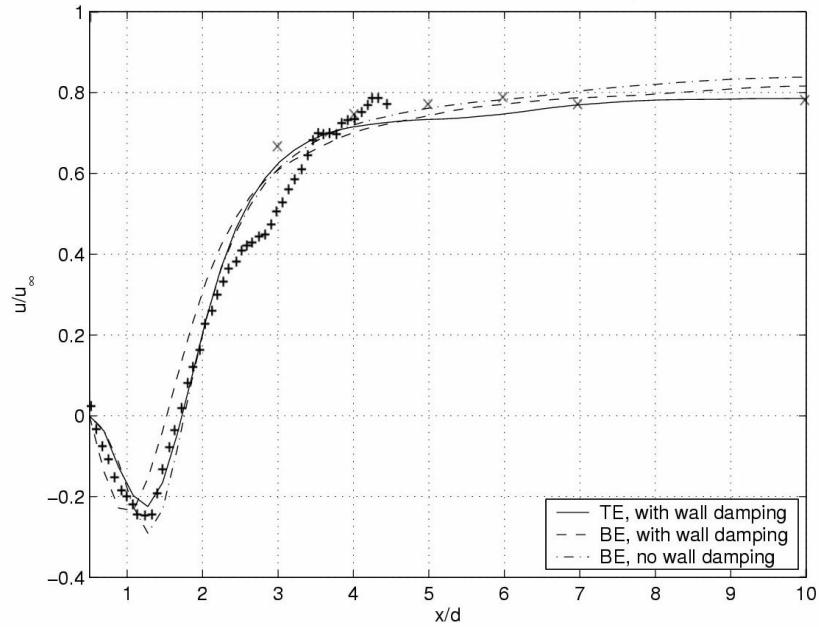

Figure 4.28: Mean streamwise velocity along the centreline of the wake. The x coordinate is measured from the cylinder centre, so x/d = 0.5 corresponds to the back of the cylinder. Experimental data (taken from [44]): + Lourenco and Shih [45], × Ong and Wallace [46].

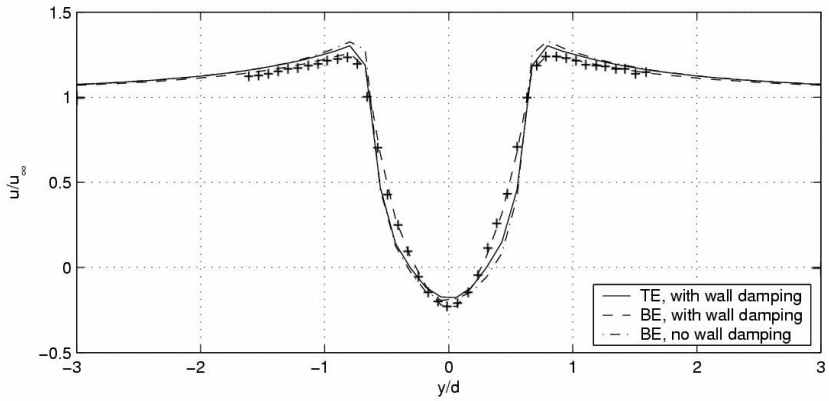

Figure 4.29: Mean streamwise velocity profile at location x/d=1.06. Symbols as in figure 4.28.

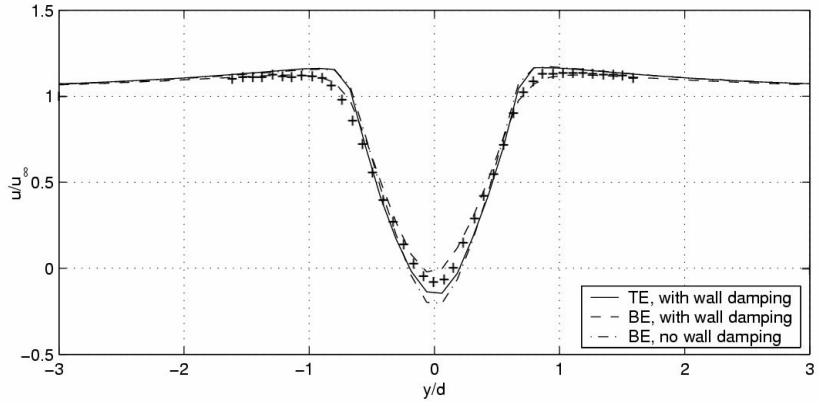

Figure 4.30: Mean streamwise velocity profile at location x/d=1.54. Symbols as in figure 4.28.

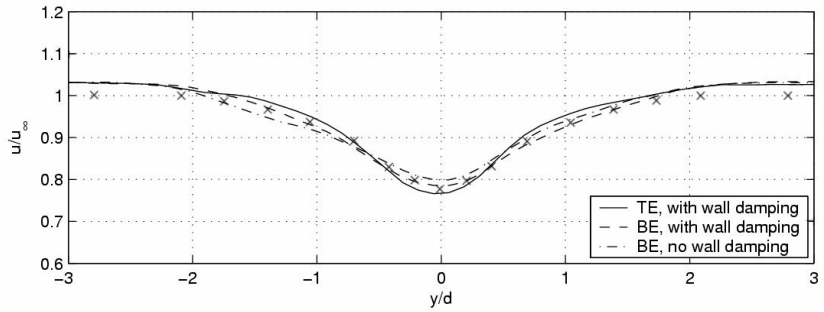

Figure 4.31: Mean streamwise velocity profile at location x/d=7.00. Symbols as in figure 4.28.

different characteristics. Backward Euler is a 1st order method, known as being more stable, but also more dissipative, than the 2nd order trapez/Euler method. The van Driest damping function is a much used improvement of the Smagorinsky model, affecting the velocity fluctuations very close to the cylinder surface, and thereby influencing everything that happens in the wake. There may be numerical interaction between the different models and methods employed, which may reinforce or weaken certain characteristics. However, it is evident from the three test cases that both the choice of time discretization scheme and the issue of wall damping have a significance for the prediction of the recirculation region behind a cylinder using large eddy simulations.

4.3.3 Conclusions

A few concluding remarks on our findings in this experiment are given below:

- The overall agreement between the present LES and the experimental data is good.
- The mean drag is overpredicted in all the test cases. A possible cause is that the spanwise domain size (cylinder length) is too small.
- There are some differences in velocity profiles and centreline velocity between the three cases, especially in the near wake. These differences suggest an influence of both time discretization scheme and van Driest damping. However, it is not clear from the present simulations which case give the "best" result, also keeping in mind that there are uncertainties in the experimental data.

Chapter 5

Flow around two cylinders in tandem

5.1 Introduction

Two or more parallel circular cylinders placed close to each other are found in many areas of engineering. Systems of flexible risers or tendons are examples of applications with particular interest in marine engineering. Risers are commonly arranged in clusters, and an important issue is avoiding collisions between the individual risers. Flow interference effects may strongly influence the dynamic behaviour of the riser system.

Despite its widespread applications, the study of flow around two cylinders started much later than flow around a single cylinder. According to Zdravkovich [47], a reason for this was the common assumption that the flow around two cylinders, and the resulting forces acting on the cylinders, should be similar to the flow around and forces acting on a single cylinder. This implied weak or negligible flow interference between the two cylinders. However, early tests (late 1960s - early 1970s) showed that this was not the case. It turned out that interference effects might change the flow pattern and vortex shedding dramatically, as well as the direction and magnitude of forces acting on the cylinders. The degree of interference was found to depend on the arrangement of the cylinders relative to each other, and on their orientation to the free stream. Even today, the flow around two cylinders is less well understood than the flow around a single cylinder, and also less studied.

Figure 5.1 shows two cylinders close to each other, with the cylinder axis perpendicular to the free stream velocity. The three main arrangement categories are: side-by-side (S = 0, T$\neq$0), tandem/in-line (S$\neq$0,T = 0), and

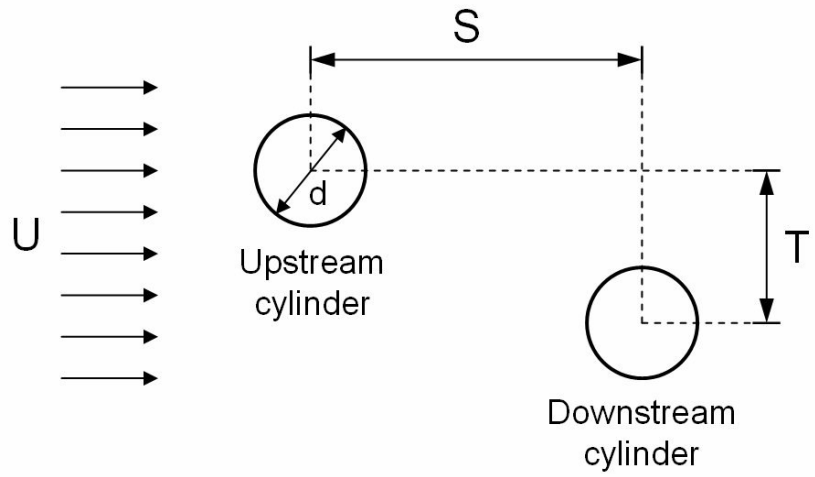

Figure 5.1: Definition sketch for the different arrangements: Side-by-side (S=0, T≠0), tandem/in-line (S≠0,T=0), and staggered (S≠0, T≠0). Further, there should be a gap between the cylinders, i.e. the total distance between the cylinder centres is greater than one cylinder diameter.

staggered (S≠0, T≠0). S and T are the streamwise and transverse spacings between the cylinder centres, respectively. In the present study, flow around two cylinders in a tandem arrangement (S = 5d, T = 0, see figure 5.1) will be investigated numerically.

A detailed experimental study of flow around two cylinders in tandem is reported by Igarashi [48]. The Reynolds number range in the experiments is $8.7{\cdot}10^3 \leq Re \leq 5.2{\cdot}10^4$ (subcritical regime), and the cylinder spacing is varied in the range $1.03 \leq \mathrm{S/d} \leq 5.0$, where d is the cylinder diameter. A total of 8 different flow patterns are identified in this parameter space. For Re greater than approx. $3.5 \cdot 10^4$, the flow pattern only depends on the cylinder spacing, whereas for lower Re, there is also some Reynolds number dependence. Some key features are summarized below (ref. [47]) (the transverse spacing is T = 0 in all the cases):

- Streamwise spacing S/d < 1.1-1.3: The separated shear layer from the upstream cylinder does not reattach to the downstream cylinder. The two cylinders act (more or less) like a single body.
- Streamwise spacing 1.1-1.3 < S/d < 3.5-3.8: The separated shear layer from the upstream cylinder reattaches to the downstream cylinder. The reattachement can be alternate, permanent or intermittent.

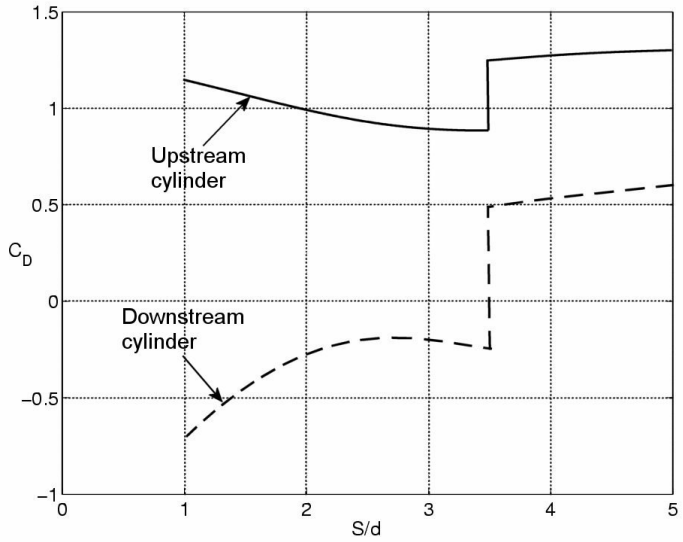

Figure 5.2: Drag coefficients as a function of cylinder spacing S/d. Two cylinders in tandem at Re=21000 (exp. by Imaichi et al, ref. [10] in [48]). Notice the discontinuity (jump) at S/d $\sim$ 3.5. At the jump, the separated shear layer from the upstream cylinder goes from a state where it reattaches to the downstream cylinder, to a state where it rolls up in front of the downstream cylinder. After the jump, we have vortex shedding behind both cylinders. (Figure reproduced after Igarashi [48])

- Streamwise spacing 3.5-3.8 $<$ S/d $<$ 5-6: The separated shear layer from the upstream cylinder roll up in front of the downstream cylinder, i.e. we have vortex shedding behind both cylinders. The two vortex streets are syncronized in frequency and phase.

- Streamwise spacing S/d $>$ 5-6: Uncoupled vortex shedding behind both cylinders. Possible different shedding frequencies for the two cylinders.

Figure 5.2 shows the drag coefficient of two cylinders in tandem as a function of the spacing S/d at Re = 21000 (data from experiments by Imaichi et al, referenced by Igarashi [48]), and figure 5.3 shows the Strouhal number based on measured velocity fluctuations behind the downstream cylinder at Re = 22000 (data from experiments by Igarashi [48]). The discontinuity in drag and Strouhal number at S/d $\sim$ 3.2-3.5 indicates the start of the regime where the separated shear layer from the upstream cylinder no longer reattaches to the downstream cylinder, and we have vortex shedding behind

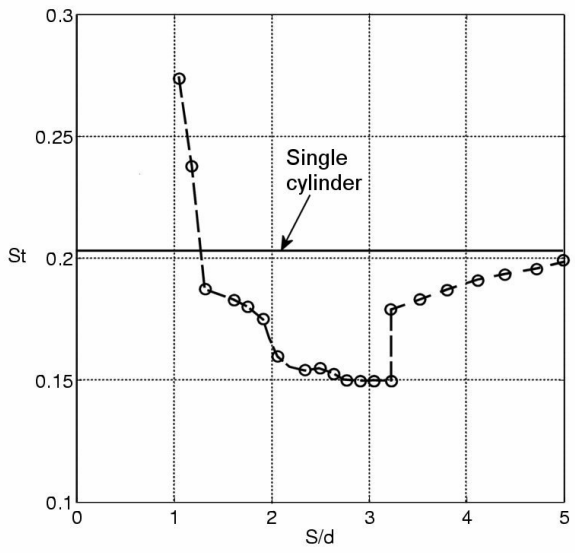

Figure 5.3: Strouhal number as a function of cylinder spacing for two cylinders in tandem at Re=22000 (exp. by Igarashi [48]), based on measured velocity fluctuations behind the downstream cylinder. See also comments to figure 5.2.

both cylinders. There is a quite dramatic jump in drag coefficient at this point, especially for the downstream cylinder, where C_D changes from negative to positive. When S/d increases beyond the discontinuity, we see that the Strouhal number gradually approaches the value of a single cylinder. This will also be the case for the drag coefficient of the upstream cylinder, see figure 5.2.

5.2 Large-eddy simulation at $Re = 21600$

5.2.1 General description

Large-eddy simulation (LES) of the turbulent flow around two cylinders in a tandem arrangement is performed at $Re = 21600$. The cylinders are fixed in space, subject to a constant, uniform and turbulence free inflow velocity field. The results are compared with data from laboratory experiments done in the current flume at Danish Hydraulic Institute (DHI) in 1999 [49], commissioned by Norsk Hydro Production. At $Re = 21600$, the flow around a single cylinder is characterized by laminar boundary layer separation, with transition to turbulence happening somewhere in the near wake. This will also be the case

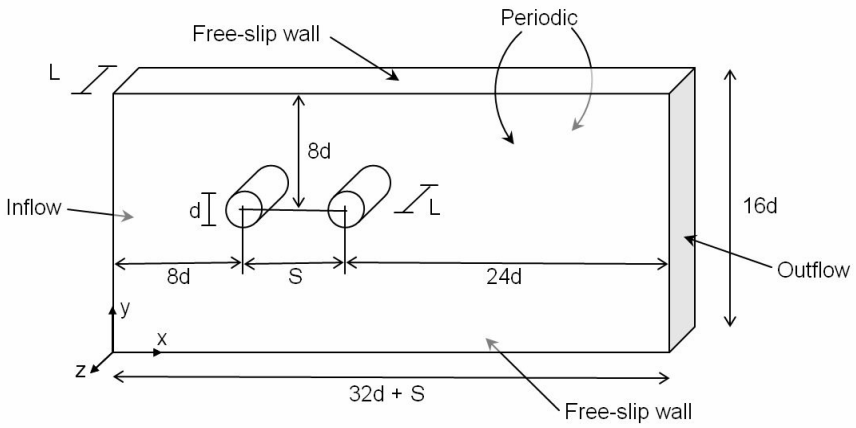

Figure 5.4: Key dimensions of the computational domain

for the upstream cylinder in the tandem arrangement, while the downstream cylinder will be exposed to the turbulent wake generated by the upstream cylinder. The computational domain is shown in figure 5.4. The cylinder diameter is d = 0.1, and the cylinder spacing is S/d = 5.0 in all the test cases. Figure 5.5 shows a principle drawing of the main flow characteristics for this cylinder spacing (ref. Zdravkovich [47]). Three different spanwise dimensions L (in the z-direction) are tested; L = 0.822d, 1.644d and 3.822d. The aim is to investigate the influence of the cylinder length in the three-dimensional computations.

Two-dimensional simulations are also performed (ref. [50]) using the same code and input data, for comparison. A two-dimensional equivalent of LES with wall damping is used. In addition, 2D simulations are carried out using no turbulence model at all. It should be noted, however, that 2D simulations of turbulent flow can never be physically correct, since turbulence is a three-dimensional phenomenon. Nevertheless, 2D computation of turbulent flow around bodies can give reasonable results in certain cases. In the present work, the two-dimensional results are included to demonstrate that there *is* a difference between 2D and 3D, and that three-dimensional effects are quite significant for the flow case in question.

The initial condition and the boundary conditions are similar to the conditions used in the previous case with a single cylinder at $Re = 3900$ (see section 4.3). In the present case, the inflow velocity is $u_\infty = 2.16$ and the viscosity $\mu = 1{\cdot}10^{-5}$, in order to get the prescribed Reynolds number of 21600 (the density remains unchanged). Also here, a non-uniform velocity field is used throughout the domain at $t = 0$, and 1% white noise is added in order

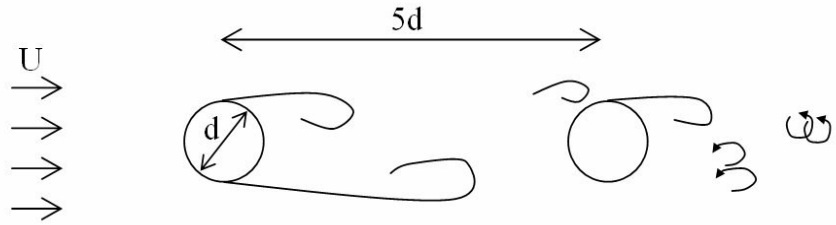

Figure 5.5: Principle drawing of the main flow characteristics: Stable, alternating vortex shedding from the upstream cylinder creates a vortex street in front of the downstream cylinder. Two vortex streets are formed behind the cylinders, syncronized in frequency and phase ("binary" vortex street). The forces acting on the upstream cylinder are mainly unaffected by the downstream cylinder (ref. Zdravkovich [47]).

to initiate the turbulent behaviour of the flow.

5.2.2 Computational grids

Three computational grids with identical two-dimensional cross-sections but with different spanwise dimension are generated, i.e. one grid for each test case. The grids are denoted SC ("short cylinder"), MC ("medium") and LC ("long"). These descriptions should only be regarded as a convenient way of distinguishing between the different cases, and not as an indication of the domain size relative to the infinite physical problem.

In the present study, a grid sensitivity analysis is not performed. Based on experience from previous simulations, the grid resolution should be sufficient in order to obtain good etimates of the Strouhal number and mean forces, even if grid convergence is not proven. Key data are given in table 5.1. Notice that the cylinder length is doubled from short to medium, and from medium to long. The basic length of $L/d = 0.822$ corresponds to the critical length scale of the 'Mode B' instability in laminar flow (see section 4.1). This basic length is chosen also in the present simulations because it has some physical significance, rather than just choosing, say, L/d = 1 as the basic length. The thickness of the elements adjacent to the cylinder wall corresponds to $0.385\frac{d}{\sqrt{Re}}$. The quantity $\frac{d}{\sqrt{Re}}$ is a frequently used estimate of the order of magnitude of the boundary layer thickness. As in previous simulations, the grids are block structured, with 8 node linear hexahedral elements for both velocity and pressure. The block topology of the grids is

Description	SC	MC	LC
Aspect ratio, L/d	0.822	1.644	3.288
Total no. of nodes	472624	915709	1801879
No. of nodes in each 2D cross-section	29539	29539	29539
Total no. of elements	438000	876000	1752000
No. of circumf. elem., upstream cylinder	180	180	180
No. of circumf. elem., downstream cylinder	200	200	200
No. of spanwise elements (along L)	15	30	60
Elem. thickness at the cylinder wall, % of d	0.262	0.262	0.262

Table 5.1: Grid data

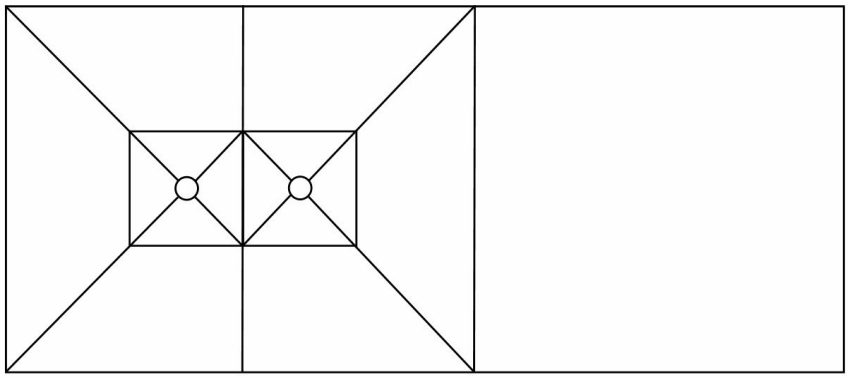

Figure 5.6: Block topology of the grids in the xy plane. See also figure 5.4.

shown as a 2D cross section in figure 5.6. The nodes are clustered towards the cylinder surface, and evenly distributed in the spanwise direction. There is a concentration of nodes in the zone between the cylinders, and behind the downstream cylinder. Moderate clustering is applied towards the middle of the wake in these areas. A detailed view of the grid is shown in figure 5.7.

5.2.3 Time integration

The second order trapez/Euler method is used in the present simulations. The time step in all three cases is $\delta t = 0.002$, which translates to O(100) time steps per vortex shedding cycle. Based on literature study and previous experience, this is found to be sufficient in order to resolve the large scale motions of the flow. An estimate of the viscous (Kolmogorov) timescale may

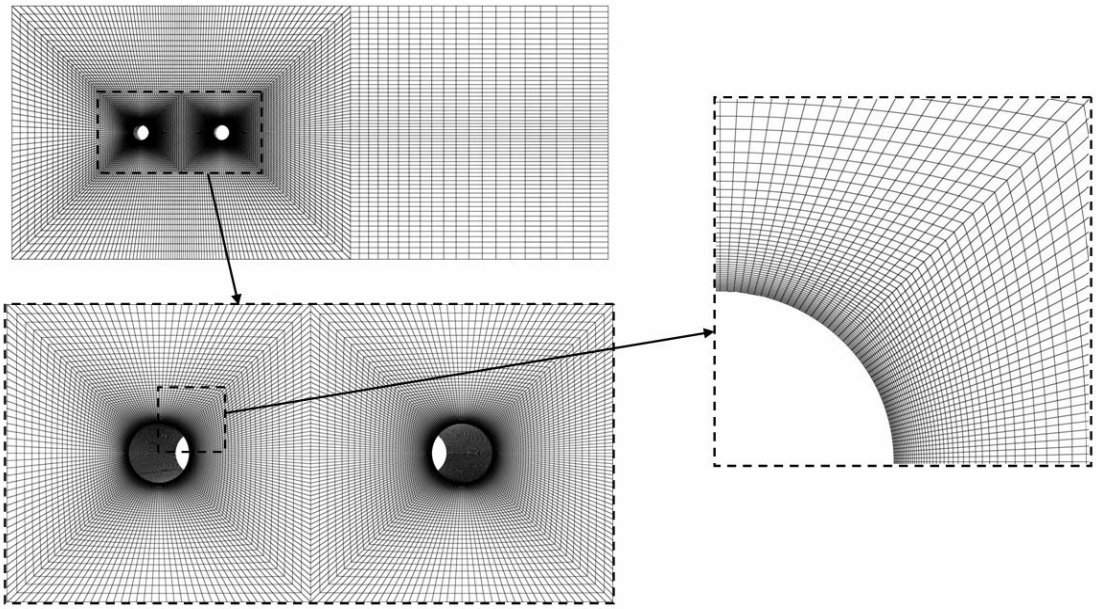

Figure 5.7: Computational grid.

be taken as

$$T_\nu = \frac{d}{St \cdot u_\infty \cdot \sqrt{Re}} \tag{5.1}$$

According to this, the ratio of time step to viscous timescale is $\delta t/T_\nu \simeq 1.2$, i.e the chosen time step does not resolve the estimated viscous timescale. However, in LES this should be sufficient resolution, since we filter out the smallest turbulent scales.

The total simulation time in each case is 10 seconds of "physical time", or 5000 time steps. This corresponds to a dimensionless time of $tu_\infty/d = 216$.

5.2.4 Results

Time series of fluctuating drag and lift coefficients from case SC (L/d = 0.822) is shown in figure 5.8. The time series from the two other 3D cases (MC and LC) and from the DHI experiment are shown in appendix B. Key results for the upstream cylinder is given in table 5.2, and for the downstream cylinder in table 5.3. When extracting data from the LES series, the first 600 time steps are excluded from the calculations, due to startup transients. The experimental data are used in full length. The results in table 5.2 and 5.3

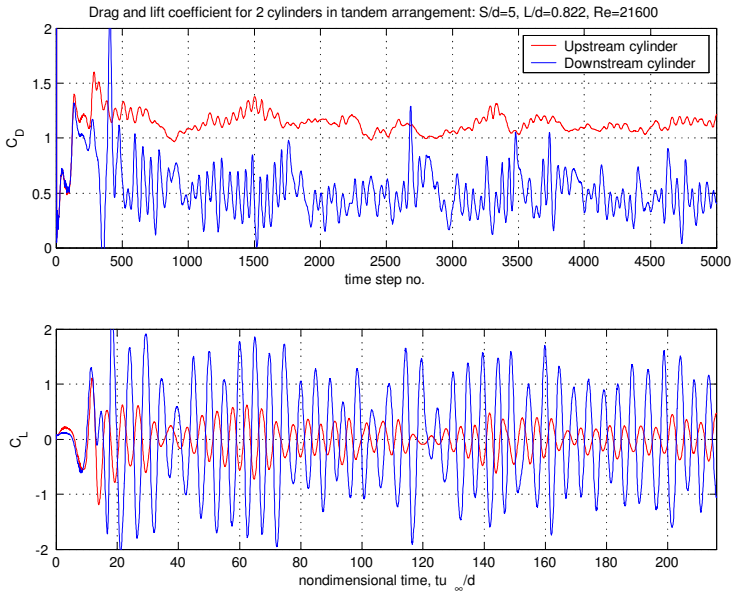

Figure 5.8: LES results: Time series of drag and lift, case SC (L/d=0.822)

Upstream cylinder	DHI exp. Ref. [49]	LES, SC Present	LES, MC Present	LES, LC Present	2D[1)] Ref [50]	2D[2)] Ref. [50]
L/d	7.5	0.822	1.644	3.288	0	0
St	0.1921	0.2006	0.1964	0.1879	0.1837	0.2232
Mean drag	1.0558	1.1243	1.0799	1.0031	1.5493	0.9126
Mean lift	0.0269	-0.0057	-0.0062	-0.0021	0.0037	0.0084
St.dev., drag	0.0706	0.0712	0.0479	0.0294	0.1550	0.0758
St.dev., lift	0.1874	0.2496	0.1660	0.0719	0.9267	0.1947

Table 5.2: Key results for the upstream cylinder. The Strouhal number is based on the frequency of the lift oscillations. Startup transients are excluded from the simulation data. From the DHI experiment, all the available data are used. 2D simulations: 1) with turbulence model (2D equivalent of LES), 2) no turbulence model.

Downstr. cylinder	DHI exp. Ref. [49]	LES, SC Present	LES, MC Present	LES, LC Present	2D[1)] Ref [50]	2D[2)] Ref. [50]
L/d	7.5	0.822	1.644	3.288	0	0
St	0.1910	0.2006	0.1964	0.1879	0.1837	0.2232
Mean drag	0.5003	0.4909	0.4785	0.5813	0.3574	0.6885
Mean lift	-0.0095	0.0040	0.0011	-0.0105	0.0003	0.0030
St.dev., drag	0.0823	0.1816	0.1354	0.1057	0.3953	0.2814
St.dev., lift	0.3699	0.9403	0.8140	0.6746	1.5372	0.6380

Table 5.3: Key results for the downstream cylinder. See comments to table 5.2.

are plotted as a function of cylinder length in figures 5.9 to 5.12. Note that the mean lift is not plotted; as this should theoretically be zero. Small deviations from zero in the simulations are insignificant, and may be due to the asymmetrical initial velocity field. However, we may notice that the mean lift on the upstream cylinder in the laboratory experiment is significantly larger than in the simulations, see table 5.2. This could imply a systematic error in the measurements. The data from the DHI laboratory experiments are plotted as constant levels in figures 5.9 to 5.12, independent of the cylinder length. The reason is that the results from the physical experiments are assumed to represent an infinitely long, "real" cylinder, although the actual length is L/d = 7.5. The influence of cylinder length in the laboratory experiments is not considered here, however, this may be an important factor that should be investigated.

Power spectra of the lift coefficient are presented in figure 5.13 (upstream cylinder) and 5.14 (downstream cylinder), calculated using FFT. The spectra are normalized (i.e the area under the curve is equal to one).

Figure 5.15 shows examples of the vorticity isosurface at corresponding phase within the shedding cycle for the three test cases; SC, MC and LC (top to bottom). The vorticity field is the scalar value of the vorticity vector, defined as $\boldsymbol{\zeta} = \boldsymbol{\nabla} \times \mathbf{u}$. The isosurface value is approx. 1.5% of the maximum vorticity.

5.2.5 Remarks on sampling time

When doing physical experiments or numerical simulation of "nearly random" processes such as turbulent flow, considerable sampling times are required in order to obtain a representative population of sample values. In the present case, the forces on the cylinders are of primary interest, so we need to look at the available time series of lift and drag from the experiment

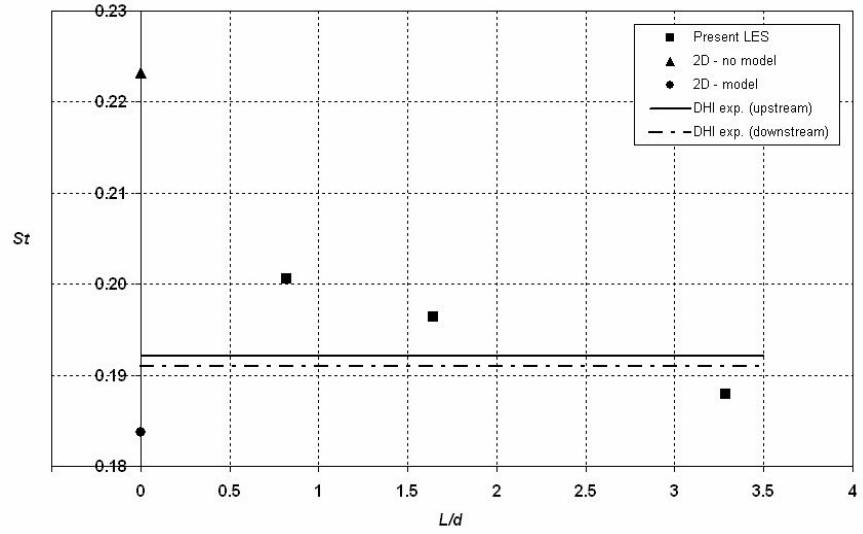

Figure 5.9: Strouhal number as a function of cylinder aspect ratio, L/d. 2D simulations: L/d = 0 $\Longrightarrow$ data on the y-axis.

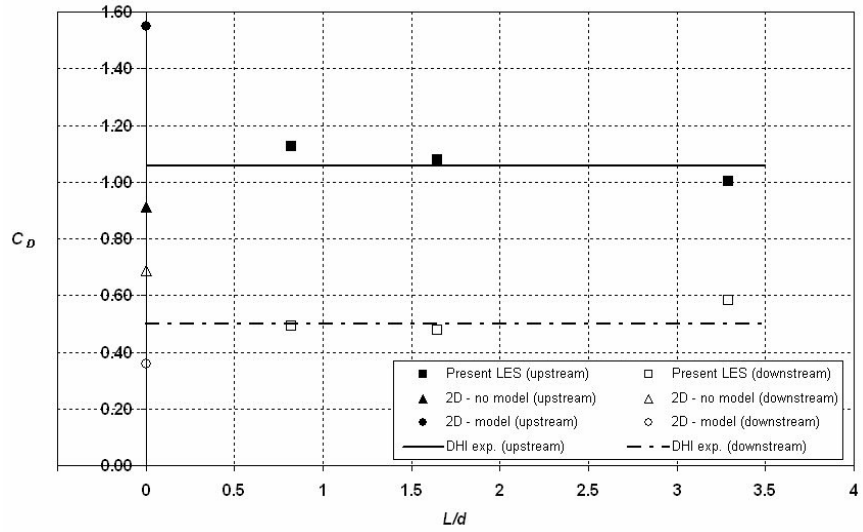

Figure 5.10: Mean drag as a function of cylinder aspect ratio, L/d. 2D simulations: L/d = 0 $\Longrightarrow$ data on the y-axis.

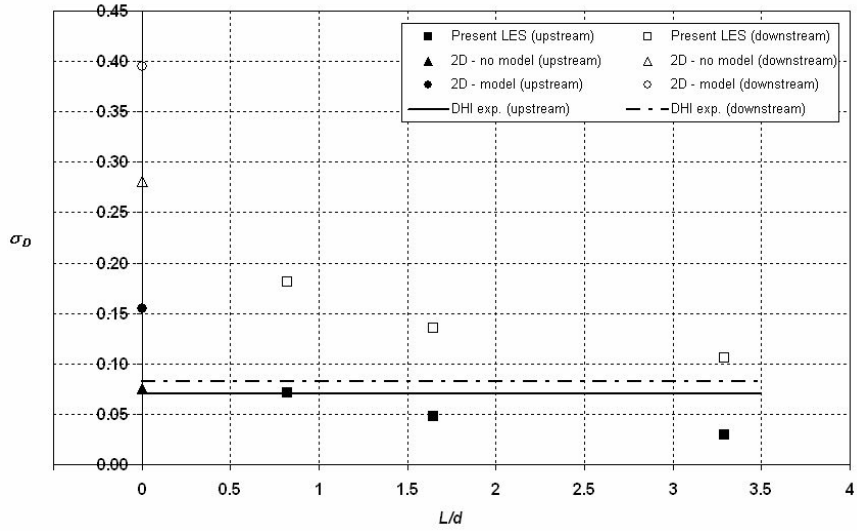

Figure 5.11: Standard deviation of drag as a function of cylinder aspect ratio, L/d. 2D simulations: L/d = 0 $\Longrightarrow$ data on the y-axis.

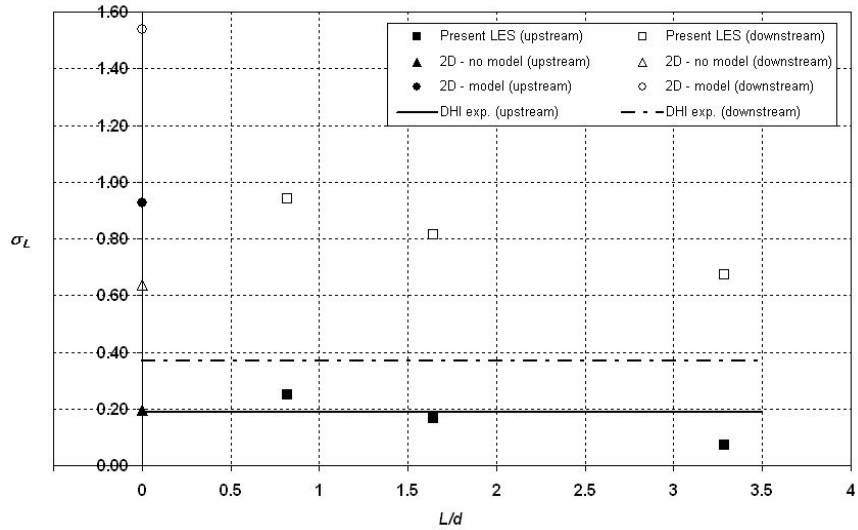

Figure 5.12: Standard deviation of lift as a function of cylinder aspect ratio, L/d. 2D simulations: L/d = 0 $\Longrightarrow$ data on the y-axis.

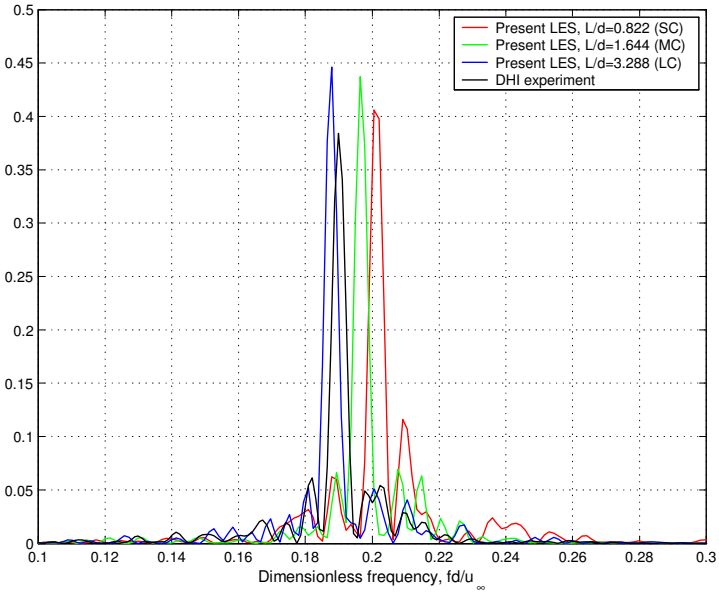

Figure 5.13: Normalized power spectra of lift, upstream cylinder. The peak on each curve represents the primary vortex shedding frequency, i.e. the Strouhal number.

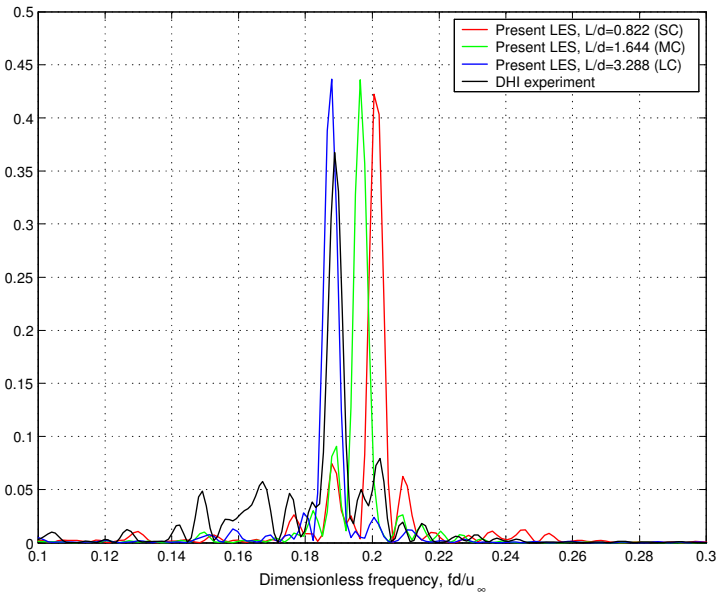

Figure 5.14: Normalized power spectra of lift, downstream cylinder.

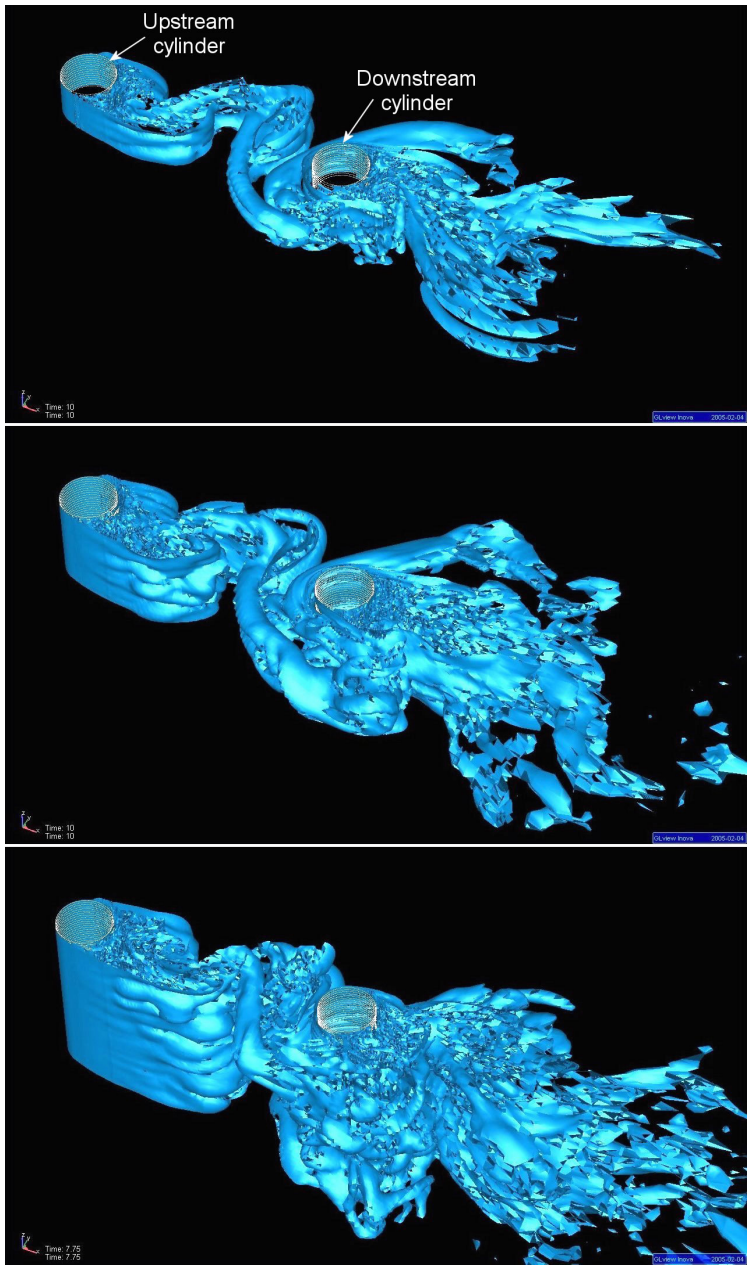

Figure 5.15: Vorticity isosurface at corresponding phase. Top to bottom: SC, MC and LC. Isosurface value: $|\zeta| = 500$, approx. 1.5% of max. value. Notice how the wake becomes less coherent and more three-dimensional and chaotic, especially behind the downstream cylinder, as the cylinder length increases.

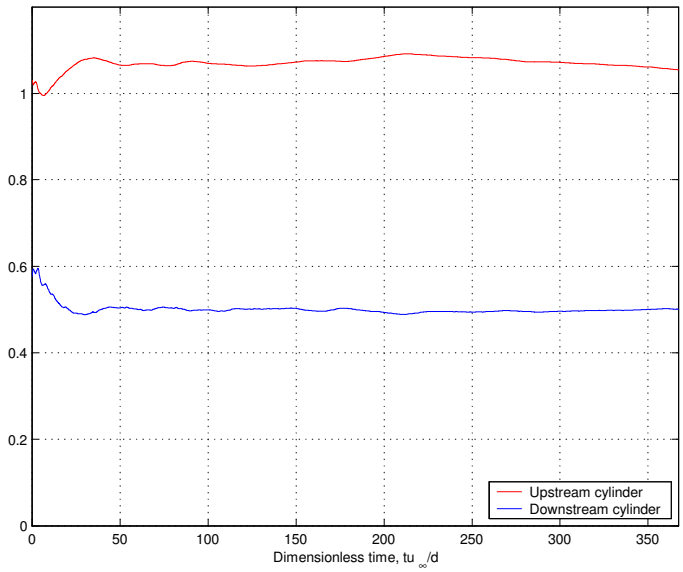

Figure 5.16: DHI experiment: Cumulative mean drag force on the two cylinders.

in order to get some clue as to how long simulation time we need. We only have access to a single time sample in the present study, so we assume that this sample is completely representative of the flow case in question (ergodic process). The total sampling time of the DHI experiment is approximately 370 in dimensionless time units, tu_∞/d. Figure 5.16-5.17 show the cumulative mean values of drag and lift on the two cylinders, i.e. a new mean value is calculated for each time step added to the series, starting at the beginning of the sample. The cumulative values are plotted as a function of dimensionless time, tu_∞/d. Figure 5.18 shows the cumulative standard deviation of lift and drag.

We see that the mean drag shows little change after approx. 50 time units, while it takes about 200 time units for the mean lift to stabilize at a more or less constant level (if we disregard the oscillations). The standard deviations also appear to become more stable after 200 time units, however, the trends are less conclusive. For example, the standard deviation of lift on the upstream cylinder shows a slightly decreasing tendency, see figure 5.18. From the cumulative values it seems clear that accurate prediction of the standard deviations require longer sampling times than what is needed for mean value estimates. Even with the available data covering 370 time units, there is some uncertainty regarding the standard deviations in the DHI experiment.

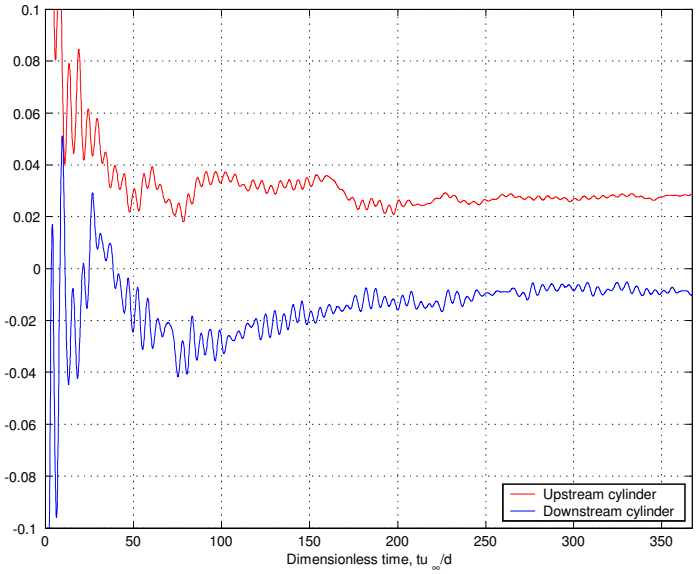

Figure 5.17: DHI experiment: Cumulative mean lift force on the two cylinders.

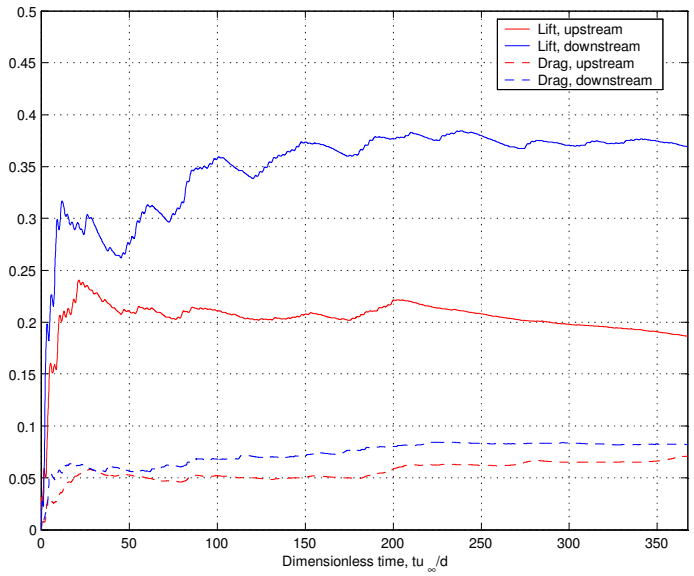

Figure 5.18: DHI experiment: Cumulative standard deviation of lift and drag for the two cylinders.

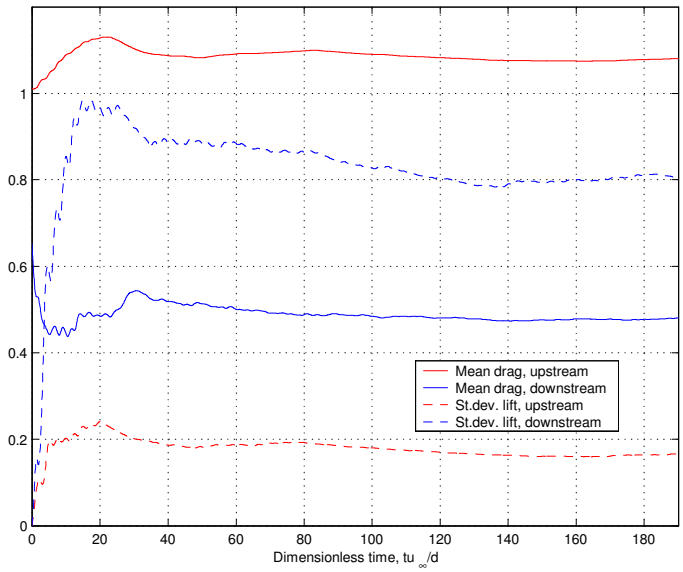

Figure 5.19: LES, case MC: Cumulative mean drag and standard deviation of lift for the two cylinders.

The present LES time series include about 4400 time steps when the startup transients are removed, equivalent to 190 dimensionless time units. Cumulative mean drag and standard deviation of lift for one of the LES time series (case MC) is shown in figure 5.19, starting at time step 600. We observe that the mean drag converges after about 50 time units also here, while the standard deviation of lift stabilizes earlier in the simulation than in the physical experiment. The two other cases (SC and LC) show similar trends. Consequently, 190 time units should be sufficient to obtain representative values for both mean and standard deviation of lift and drag in the numerical simulations.

5.2.6 Discussion

The following trends may be observed directly from the time series of lift and drag (figure 5.8 and figures in appendix B):

- The mean drag on the downstream cylinder is about half the mean drag on the upstream cylinder. Clearly, the downstream cylinder is sheltered behind the upstream cylinder. Consequently, the effect of the incoming flow on the downstream cylinder is reduced.

- The oscillations of both lift and drag are significantly larger on the downstream cylinder than on the upstream cylinder. This is caused by the vortices shed by the upstream cylinder colliding with the downstream cylinder, inducing large pressure fluctuations.

- There appears to be an "almost periodic" variation in the force amplitudes, which can be seen most clearly in the lift time series. The phenomenon is especially evident in the laboratory experiment, where the time series are longer, but the same effect appear in the numerical simulations as well. In order to quantify this variation, we would need significantly longer sampling times.

From figure 5.9 we see that the Strouhal number (St) of the present large-eddy simulations agrees well with the DHI experiment. The deviation is only about 2-4% for all the three cylinder lengths. Further, we observe that the Strouhal number decreases when the cylinder length is increased, which clearly indicates a length dependence. We may also note that St from the present LES and the DHI experiment are both in good agreement with experiments by Igarashi [48], see figure 5.3. The 2D simulation with turbulence model (denoted '2D - model' in the following) also gives a good estimate of St, while the 2D simulation with no model (denoted '2D - no model') is a bit further off. Note that St is identical for the upstream and downstream cylinder in all the simulations, while there is a small difference between the cylinders in the experimental results. However, this difference is too small to disprove frequency syncronization in the laboratory experiment.

The mean drag on both cylinders in the present LES is also in excellent agreement with the DHI experiment, see figure 5.10. The largest deviation is ca. 5%. Also here, the mean values show a slight decrease when the cylinder length is increased. The trend is consistent, apart from one result; the mean drag on the downstream cylinder in the LC case. Note that the experiment by Imaichi, ref. figure 5.2, gives a higher drag coefficient for the upstream cylinder than the present LES and the DHI experiment, whereas the agreement is good for the downstream cylinder. The 2D results do not agree equally well; especially the mean drag on the upstream cylinder in the '2D - model' case is much too high.

When it comes to the standard deviation of lift and drag (figure 5.11-5.12), the present LES show reasonably good agreement for the upstream cylinder, however, the force oscillations on the downstream cylinder are generally too high compared to the experimental results. This can also be seen directly from the time series of drag and lift (figure 5.8 and the figures in appendix B). However, the decreasing trend with increasing cylinder length is very

consistent. In the case of standard deviations, '2D - no model' appears to hit the spot for the upstream cylinder, while the values for the downstream cylinder are too high. '2D - model', on the other hand, is further away from the experimental results. Not surprisingly, it appears to be more difficult to get good estimates of the standard deviations than of the Strouhal number and mean values of lift and drag in the numerical simulations.

From figure 5.13-5.14, we see that the present LES and the experiment have the same general shape of the lift power spectra. The peaks are a bit higher in the simulation than in the experiment, suggesting that more energy is concentrated around the primary (von Karman) vortex shedding frequency in the simulations. The difference is largest for the downstream cylinder. Here we can clearly see a few additional peaks around the Strouhal frequency on the experimental spectrum, which are not present on the simulated spectrum. Apart from this, the spectral content of the lift oscillations appears to be quite similar in the simulations and the experiment.

The influence of the cylinder length is quite evident in the 3D simulations. All the main parameters (apart from the mean drag on the downstream cylinder) show a consistent decrease when the spanwise dimension L is increased. An indication of what causes the decrease in mean drag on the upstream cylinder may be found by looking at figure 5.15. When comparing the isosurfaces of vorticity from the three cases, we may notice that the wake becomes less coherent, and more chaotic and "three-dimensional" as the length increases. It is also quite evident that the vortex shedding from the upstream cylinder becomes less syncronized along the span of the cylinder. What happens around the downstream cylinder is more difficult to see from the isosurface plot. A loss of syncronization in the z-direction means that the integrated effect of the pressure distribution on the cylinder surface is reduced, and we get a lower mean drag. In the case of 2D flow simulation, we have perfect syncronization (as everything happens in a single cross-section), and consequently the mean drag becomes higher.

5.2.7 Conclusions

The results from the present large-eddy simulations of flow around two circular cylinders in a tandem arrangement at Re = 21600 show good agreement with the experimental data from DHI. This demonstrates that the numerical method can be applied successfully to this type of flow case, at least for the purpose of estimating the Strouhal number and mean forces acting on the cylinders. The main characteristics of the flow are well reproduced. However, whether or not the computed velocity field contains the small-scale characteristics of a true turbulent flow field has not been investigated here, as this

is beyond the scope of the present study. Nevertheless, the isosurface plot in figure 5.15 gives an impression of the complexity of the flow, and shows that the flow is indeed three-dimensional, even if the geometry is nominally two-dimensional. Overall, the 3D simulations give better and more consistent results than the 2D simulations.

A clear dependence on the spanwise dimension (cylinder length) is demonstrated in the computations. The plots in figures 5.9-5.12 suggest that the results may change even more if the cylinder length is increased beyond L/d = 3.288. Further simulations should be carried out with the same 2D cross-section, but with even larger spanwise dimension, in order to determine the asymptotic cylinder length for the present case (i.e. the spanwise dimension for which the results become length independent).

Further investigations into the apparent quasi-periodic variation of the force amplitudes should also be carried out, however, this will require significantly longer simulation times. Assuming we need O(50) cycles of the force amplitude variation to get a representative sample, the simulation time should be at least ten times longer than in the present simulations.

Chapter 6

Laminar flow around spheroids

6.1 Flow around a 6:1 ellipsoid

Flow around an ellipsoid (or prolate spheroid) with an aspect ratio of 6:1 has become a benchmark case for numerical investigation of bluff body flows. The geometry can be seen as a generalization of several applications in aero- and hydrodynamics: A simplified submarine hull, the body of an airplane or helicopter, a missile or torpedo etc. Several researchers have done CFD computations of flow around an ellipsoid at an angle of attack, typically 10-20 degrees, see figure 6.1. This may represent e.g. a turning U-boat. See for example Rhee & Hino [51], Constantinescu et al [52]. However, in the present case, the 6:1 ellipsoid is subject to pure cross flow, i.e $\alpha = 90$ degrees, see figure 6.2. In this initial study of flow around an ellipsoid, a single computational grid with approx. 434000 nodes is used. The body surface is constructed from six rational B-spline surfaces, see figure 6.3. The Reynolds number is $Re = u_\infty d/\nu = 100$ (laminar flow), and the dimensionless time step is $\delta t' = \delta t \cdot u_\infty / d = 0.075$. When choosing the resolution in space

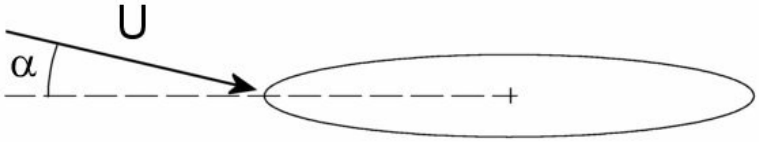

Figure 6.1: Definition of the the angle of attack α. In most of the computational and experimental work done by other researchers, $\alpha \leq 20$ degrees.

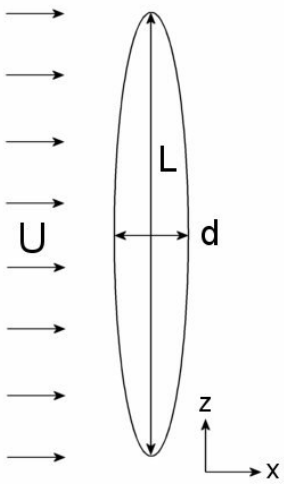

Figure 6.2: Ellipsoid in pure cross flow.

and time, similar considerations are made as in the cylinder case (laminar flow), see section 4.2. A single simulation is performed, with a sampling time of $t \cdot u_\infty/d = 225$ (dimensionless units is), corresponding to 3000 time steps. The time integration is performed using the first order backward Euler method.

6.2 Flow around a sphere

Numerical simulation of flow arund a sphere is one of the most challenging cases of three-dimensional bluff body flow. It may be see as a generalization of flow around spheroids, like the 6:1 ellipsoid described above. What makes the sphere even more difficult than the ellipsoid is the fact that the sphere is rotationally invariant about every axis - all directions are equal. Consequently, flow around a sphere is less geometry driven than any other bluff body flow. From a computational point of view, this makes the flow very sensitive to numerical methods and user input.

In the present study, flow around a sphere $Re = 300$ is performed. The results are compared with data from Johnson & Patel [53]. A single simulation is performed, with a computational grid of approx. 732000 nodes. As in the ellipsoid case, the grid is generated using rational B-spline surfaces. The dimensionless time step in the simulation is $\delta t' = \delta t \cdot u_\infty/d = 0.03$. The sampling time is $t \cdot u_\infty/d = 105$, corresponding to 3500 time steps. The second order trapez/Euler time integration method is applied in this simulation.

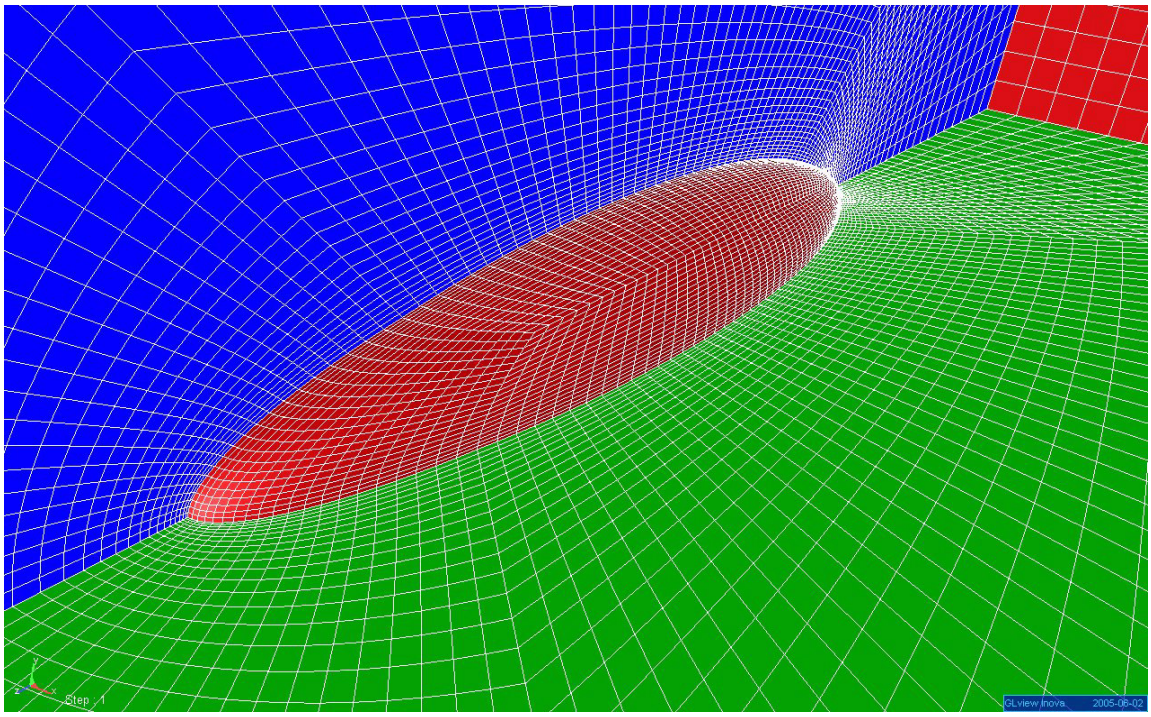

Figure 6.3: The figure shows the computational grid on the surface of the ellipsoid itself, and on two planes intersecting the ellipsoid; the xz plane (green) and the yz plane (blue). We can also see one of the domain boundaries (red, upper right hand corner of the image).

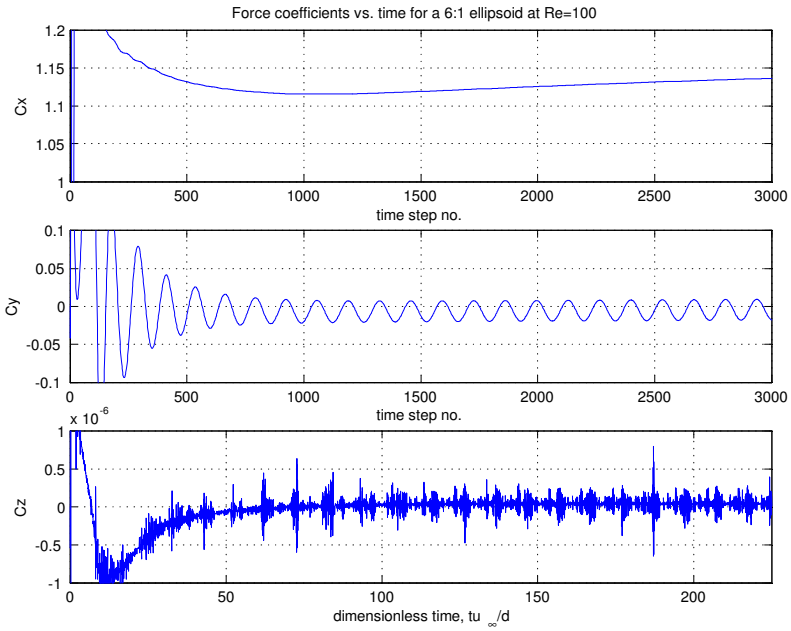

Figure 6.4: 6:1 ellipsoid, $Re = 100$: Time history of force coefficients C_x (drag), C_y (lift) and C_z (side force).

6.3 Results and discussion

Figure 6.4 and 6.5 show the time history of the force coefficients in each axial direction for the ellipsoid and the sphere, respectively. The force coefficients for the ellipsoid are defined as

$$C_{x,y} = \frac{F_{x,y}}{\frac{\pi}{8}\rho u_\infty^2 L d} \tag{6.1}$$

$$C_z = \frac{F_z}{\frac{\pi}{8}\rho u_\infty^2 d^2} \tag{6.2}$$

and for the sphere:

$$C_{x,y,z} = \frac{F_{x,y,z}}{\frac{\pi}{8}\rho u_\infty^2 d^2} \tag{6.3}$$

Here, C_x corresponds to drag, C_y lift and C_z side force coefficient. We observe that the drag (C_x) on the ellipsoid does not quite stabilize at a constant mean level within the time sample, but shows a slight increase towards the end of the simulation. This slow variation most likely "overrides" any oscillations in drag force, and the drag curve appears smooth. The drag on the sphere, on

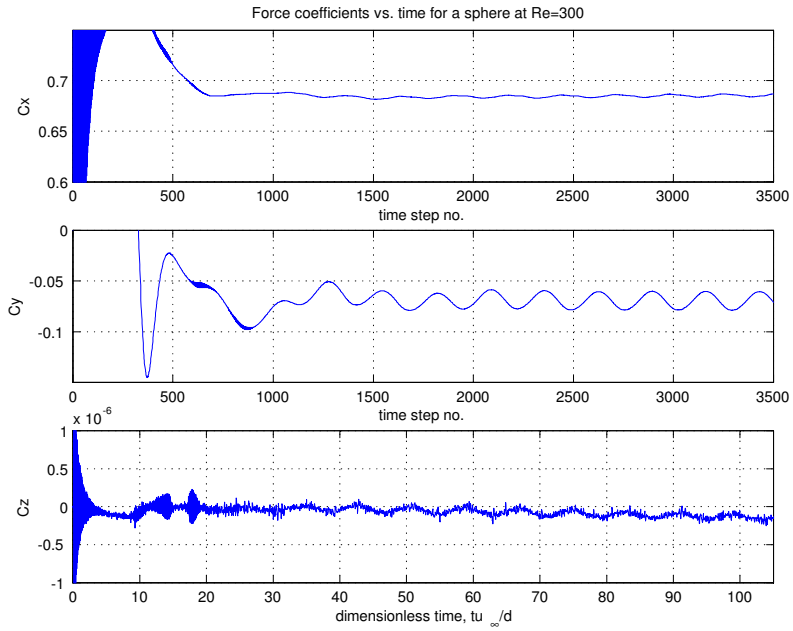

Figure 6.5: Sphere, $Re = 300$: Time history of force coefficients C_x (drag), C_y (lift) and C_z (side force).

Description	Ellipsoid, Re = 100 Present simulations	Sphere, Re = 300 Present simulations	Sphere, Re = 300 Simulations, ref. [53]
Strouhal number	0.0993	0.1252	0.137
Mean drag (x-dir.)	1.1245	0.6846	0.656
Mean lift (y-dir.)	-0.0059	-0.0693	-0.069
Peak-to-peak drag	0.0000	0.0043	0.007
Peak-to-peak lift	0.0325	0.0205	0.032

Table 6.1: Mean flow parameters for the 6:1 ellipsoid at Re=100 and the sphere at Re=300.

the other hand, shows a small periodic oscillation around a constant mean value. The lift force (C_y) is perfectly time periodic in both cases. Further, there are small numerical oscillations in side force (C_z) in the two cases (notice that the scale on the C_z-axis spans the interval -10^{-6} to 10^{-6}). By definition, the side force acts normal to the mean flow symmetry plane, and should therefore be zero.

A visualization of the wake flow pattern behind the ellipsoid is shown in figure 6.6. The figure shows the instantaneous streamwise vorticity ζ_x as isosurfaces (top, side and perspective view of the same instant). The green surface has the value $\zeta_x = 0.5$, while the red surface has $\zeta_x = -0.5$. These values correspond to about 5% of the maximum streamwise vorticity, positive and negative. Figure 6.7 shows a similar visualization of the streamwise vorticity behind the sphere. The green and red surfaces have the values $\zeta_x = -1.7$ and 1.7 respectively. This corresponds to ca. 10% of the max values.

Key parameters from the present simulations of ellipsoid and sphere flow are listed in table 6.1, together with data from Johnson & Patel [53]. Their numerical results show that the flow around a sphere becomes unsteady and periodic at $Re \simeq 280$. At $Re = 100$, the sphere flow is steady and axisymmetric. Looking at the present ellipsoid simulation, the the flow is clearly unsteady at $Re = 100$. This indicates that unsteadiness starts at a much lower Reynolds number for the ellipsoid than for a sphere. From table 6.1, we see that the Strouhal number for the ellipsoid at $Re = 100$ is lower than for the sphere at $Re = 300$, however, the St values are comparable in magnitude. Some of the difference in St may be due to the difference in Re in the two cases. The computed mean drag on the ellipsoid at $Re = 100$ is very close to the value of about 1.12 reported for a sphere at $Re = 100$ (Johnson & Patel and their references, both simulations and experiments).

In the case of the sphere at $Re = 300$, we may note that the overall agreement between the present simulation and the data from Johnson &

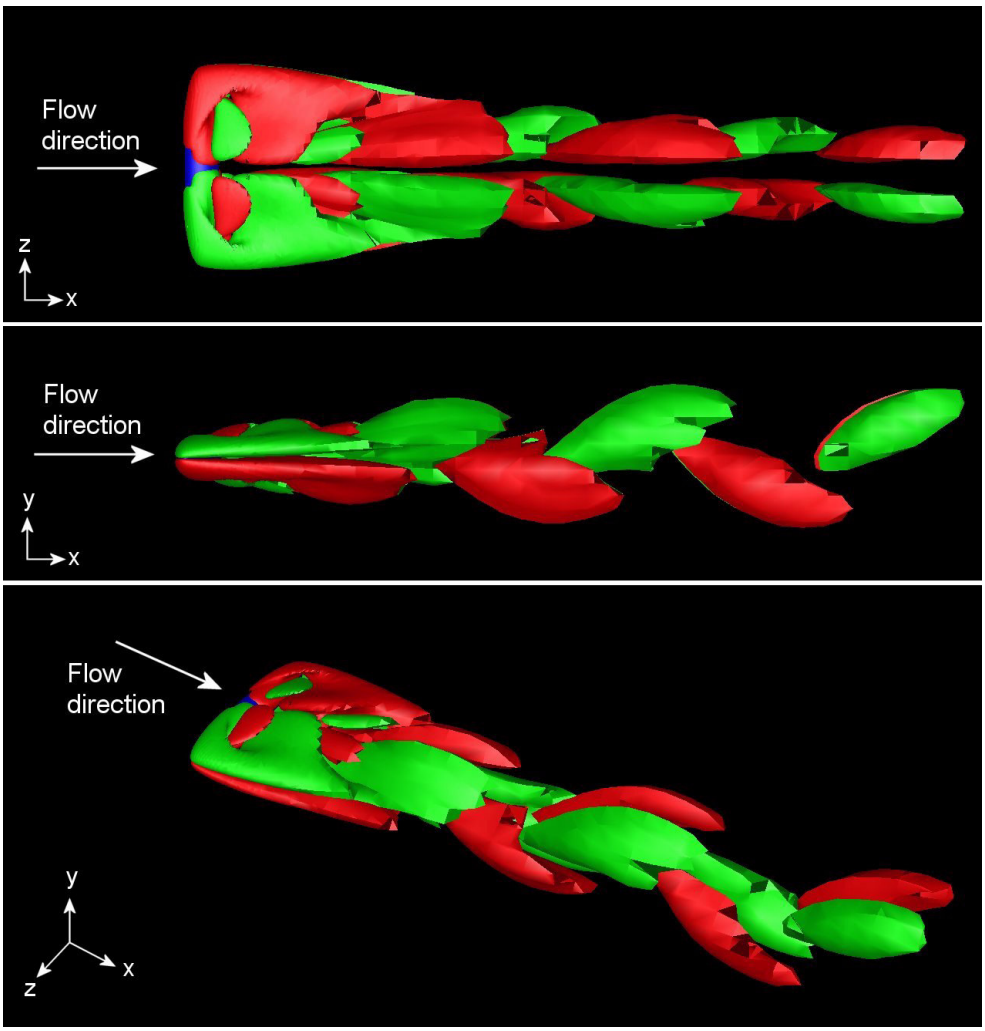

Figure 6.6: 6:1 ellipsoid: Isosurfaces of instantaneous streamwise vorticity, $\zeta_x = 0.5$ (green) and $\zeta_x = -0.5$ (red). Three different views of the same instant. The values correspond to about 5% of the max values (positive and negative).

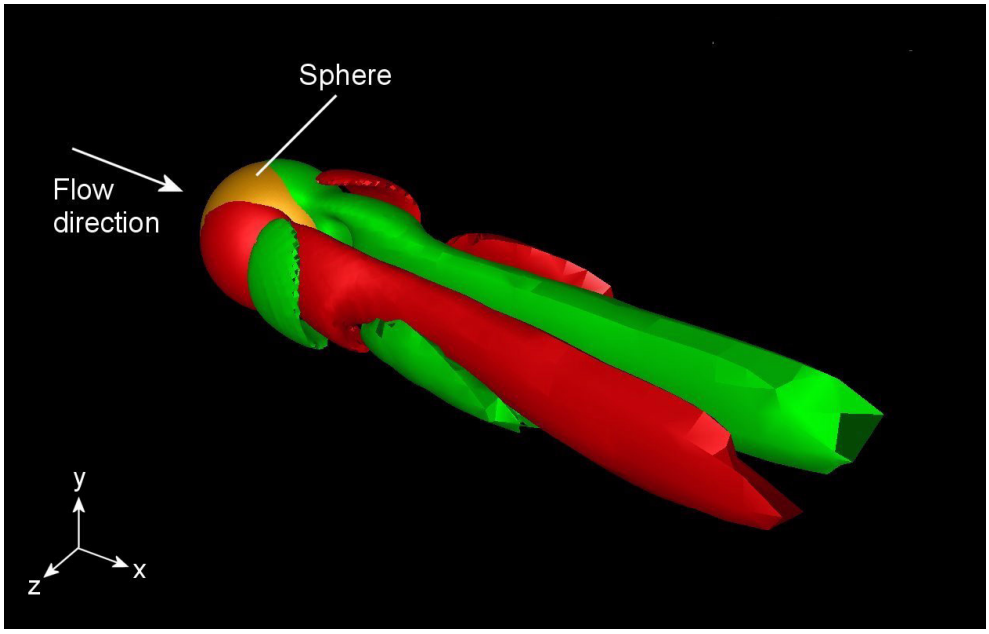

Figure 6.7: Sphere: Isosurfaces of instantaneous streamwise vorticity, $\zeta_x = 1.7$ (green) and $\zeta_x = -1.7$ (red), corresponding to about 10 % of the max. values (positive/negative).

Patel is very good. Especially, the mean lift forces are very close in the two cases. The Strouhal number is slightly lower in the present simulation, and this may be due to insufficient grid resolution. Also, the peak-to peak values are lower than the results of Johnson & Patel. However, the oscillations are generally very small relative to the mean force on the sphere - much smaller than the oscillatory force on a cylinder at $Re = 265$, see table 4.3. This indicates that the vortex shedding is quite weak. Therefore, we would expect the flow around a sphere to be more sensitive to grid resolution and time step than the flow around a circular cylinder.

All the three cases listed in table 6.1 show a mean lift force (or lateral force in the case of a sphere) different from zero, a quite interesting flow feature. According to Johnson & Patel, this is due to a loss of axial symmetry occuring before the flow becomes unsteady. The loss of symmetry starts at $Re = 212$ in the sphere case. When the Reynolds number increases, the absolute value of mean lift also increases, which means that the flow becomes more asymmetric.

6.4 Conclusions

Initial simulations of flow around an ellipsoid and a sphere at low Reynolds numbers are performed, and the results are very encouraging. Regarding the cross flow around a 6:1 ellipsoid, it's impossible to draw any definitive conclusion from a single time sample at $Re = 100$, with no reference data available. However, the present simulation gives a few indications concerning the nature of the wake flow. First of all, the flow is unsteady and time periodic at $Re = 100$. The visualization shows that the flow pattern bears little resemblance to the von Karman vortex street behind a circular cylinder, but looks more similar to the flow behind a sphere at $Re = 300$. The comparison of mean flow data from the present 6:1 ellipsoid simulation and the data for a sphere at $Re = 300$ substantiates the relationship between the flows around the ellipsoid and the sphere, in particular, the non-zero lift force found in both cases.

Chapter 7

Concluding remarks and future work

Through a series of numerical experiments we have demonstrated that the Navier-Stokes solver VISTA is able to simulate realistic, complex three-dimensional flow situations, generic to many problems in the field of marine engineering. The agreement with reference values, i.e experiments at the same Reynolds number, is generally very good. In all the cases where mean drag has been compared, we obtain a deviation on the order of 5% from the reference results. This is within the bounds of uncertainty (standard deviation) in most laboratory experiments. So, the goal of *high fidelity simulations* in marine engineering has been fulfilled. Of course, this level of accuracy comes at a cost; the computational work involved is substantial. The total simulation time for a representative time sample may vary from a couple of days in the laminar cases, to more than a week for the largest turbulent cases. Most of the simulations presented have been run on 32-96 processors on the supercomputer at NTNU. It should be noted, however, that the supercomputer processors are up to 5 years old. The VISTA code has been tested on a new (2004) PC cluster, and a performance increase of a factor 4-5 compared to the supercomputer has been reported. It should also be stressed that the VISTA code is still under development, and has not yet been fully optimized for serial performance.

An important insight from the cylinder cases is that "the world is 3D" - even when the geometry is nominally two-dimensional, and the Reynolds number is low. Although the two-dimensional vortex shedding is very strong, and governs the overall flow picture around a circular cylinder in a large Reynolds number region, three-dimensional effects play an important role long before the flow becomes turbulent. In fact, the wake turbulence has its origin in the 3D instabilities described in section 4.2.

A substantial part of the man-hours required to do the present simulations were spent on grid generation. High quality computational grids are essential in order to obtain accurate results in CFD. The grid generator used, Griddler, is a script based code, with no graphical user interface. Using a script based tool ensures good control of the grid generation, but the input can be quite tedious. All the grids used in the present simulations are block structured, with hexahedral elements. This type of grid is favourable with respect to controlling the grid quality in critical areas, such as the boundary layer regions very close to body surfaces. Also, structured grids are generally known to have good convergence properties. On the downside, structured grids are not very flexible. In order to get enough elements where you want them, you may have to put a lot of elements where they are not needed, and this is not very cost-effective. When the geometry and block topology becomes more complex, this problem increases. An obvious solution is to use unstructured grids (currently not implemented for 3D grids in Griddler). This solves the flexibility problem, and in addition, we get the possibility of using adaptive grids. However, we lose some control of the gridding in critical areas (boundary layers etc.). An even better solution would be to use grids that are structured in areas where we need full control, and unstructured/adaptive in the rest of the domain (hybrid grids). This type of grid is also well suited for moving objects.

Introducing moving cylinders is a highly relevant extension of the present work, with particular view to the problem of vortex induced vibrations (VIV) of marine risers. A logical first step towards true fluid-structure interaction (FSI) would be to impose forced oscillations of the cylinders (or the downstream cylinder in the tandem case), and solve the fluid problem independently of the cylinder motion. Of course, both the problem of forced oscillations, and the true FSI problem where the motion is determined by the forces acting on the cylinder, are significantly more computationally expensive than the fixed cylinder problem. Vortex induced vibrations and fluid-structure interaction are hot topics in the marine research communities at present, and areas of ongoing work in the VISTA group.

Visualization of complex fluid flows is a challenging task. This applies to both computer simulations and laboratory experiments. Turbulent flows in particular put great demands on the visualization techniques, but also laminar flows can be quite complicated, as the present study has shown. In the case of 3D cylinder wakes, the fact that the geometry has a constant 2D cross-section makes the flow easier to visualize. We can get much information about the flow field from looking at cutting planes. However, three-dimensional flow features require other visualization tools. Examples are particle tracing, streak lines, or the iso-surfaces used in the present study.

When the geometry is also "fully three-dimensional", as in the case of a sphere or an ellipsoid as presented in chapter 6, we really depend upon 3D visualization in order to understand what is going on. In these cases, even iso-surfaces of scalar fields such as the velocity or vorticity fail to give a clear picture of the complex vortex shedding.

CFD simulations have the potential of generating huge amounts of data, but storing all the data is neither possible nor desirable. Consequently, careful data extraction and postprocessing are essential ingredients in the successful use of CFD. The resolution of data that can be extracted from a simulation is only limited by the grid resolution and the time step. In most cases, the velocity and pressure fields are output directly from the solver. All other visualization variables are derived from the velocity and pressure. Laboratory experiments also generate a lot of data. However, in contrast to CFD, practical limitations related to experimental measurements determine which data can be extracted. For example, state of the art PIV (particle image velocimetry) equipment can provide a high resolution of the three-dimensional velocity vector, but measurements may only be performed in a single two-dimensional cutting plane at a time. It is not possible to capture the entire three-dimensional flow domain at once, as we can do with CFD. Also, the pressure on body surfaces can only be measured experimentally at discrete points. An advantage of experiments, however, is that certain aspects of the flow can be seen directly, such as 3D separation lines and vortex patterns, turbulent mixing, and so on. These flow features are not trivial to abstract from computed velocity and pressure fields.

Practically all flow problems encountered in marine engineering are turbulent, and turbulence modelling will inevitably become an important issue when doing marine CFD calculations. In the present work, the highest Reynolds number is $Re = u_\infty d/\nu = 21600$, at which also the referenced model tests of marine risers are performed [49]. In this flow regime, we have laminar separation on the cylinder surface, and turbulence occuring somewhere in the near wake (subcritical turbulent flow). We do not require a turbulence model that can treat turbulent boundary separation very accurately in this case. The static Smagorinsky model used in the present simulations is relatively crude when it comes to near-wall modelling, but still gives good results for the Strouhal number and mean forces. Apart from the fact that the flow is subcritical, this could also indicate that the flow problem itself is mainly geometry driven, and not very sensitive to turbulence modelling in general. The full scale Reynolds number for ocean current past a typical marine riser is $O(10^6)$. Further simulations of flow around a 3D cylinder at e.g $Re = 10^6$, using both the static Smagorinsky model and more sophisticated models, may answer some of these questions, and would be a relevant extension of

the work presented here. Also, a proper physical assessment of how well the simulated turbulence agrees with real turbulence should be performed.

Many questions related to numerics and software implementation have come up in the course of the present work, and should be addressed as part of the general validation and verification of the code. This includes more complete convergence studies, error estimation and so on. Also, issues related to serial as well as parallel performance of the code should be investigated. We have not focused on perfomance in this study. There are also many interesting questions related to general CFD practice that need further investigation. One example is regarding the size of the computational domain. In the cylinder cases, we have focused on the spanwise domain size, i.e the length of the cylinders. Increasing the cylinder length further is an obvious extension of the present work, simply to determine the length required to approximate an infinitely long cylinder in three-dimensional flow simulations. But also, the width and the streamwise dimension of the computational domain are important factors. We want to avoid blockage effects, pressure reflections from the outflow boundary etc., but we would also like to keep the computational domain as small as possible to save computational work. These issues have not been investigated in the present work.

An important statistical issue concerns the length of time samples, not only in computations, but also in laboratory experiments. How long time series do we need? The answer depends on the nature of the flow. If the flow is perfectly periodic, a few vortex shedding cycles is enough. But in most situations, the flow is only quasi-periodic - even low Reynolds number flow past a circular cylinder, as the present study has shown. There may be slow variations in frequency and amplitude of the oscillating forces on the cylinders. In order to quantify these variations, we need significantly longer sampling times than what's required for perfectly periodic flows. In computer simulations we also want to make sure that such variations are of physical and not numerical origin. The physical mechanisms governing the slow amplitude variations involve interaction between different types of vortex shedding and turbulence, and are not yet understood. This problem, as well as many other complex phenomena, ensures that flow around a circular cylinder will remain a challenge for researchers in the years to come.

Chapter 8

Bibliography

[1] L. Larsson, F. Stern, V. Bertram (editors): *"Gothenburg 2000: A Workshop on Numerical Ship Hydrodynamics",* Proceedings. (Chalmers University of Technology, 2002)

[2] R.F. Beck, A.M. Reed, E.P. Rood: *"Application of Modern Numerical Methods in Marine Hydrodynamics"*, SNAME Transactions (Vol. 104, 1996, pp. 519-537)

[3] L.Larsson et.al.: *"Failures, Fantasies and Feats in the Theoretical/Numerical prediction of Ship Performance",* 22nd Symposium on Naval Hydrodynamics, Washington DC, 1998

[4] J.J. Gorski: *"Present State of Numerical Ship Hydrodynamics and Validation Experiments",* 20th International Conference on Offshore Mechanics and Arctic Engineering (OMAE), Rio De Janeiro, Brazil, 2001

[5] C.W. Dawson: *"A Practical Computer Method for Solving Ship-Wave Problems",* 2nd International Conference on Numerical Ship Hydrodynamics, Berkeley, California, 1977

[6] J.L. Hess, A.M.O. Smith: *"Calculation of Non-Lifting Potential Flow About Arbitrary Three-Dimensional Bodies",* Douglas Aircraft Company Report No. ES40662, 1962

[7] O.M. Faltinsen: *"Sea loads on ship and offshore structures"*, Cambridge University Press, 1990

[8] O.M. Faltinsen, F.C. Michelsen: *"Motions of Large Structures in Waves at Zero Froude Number"*, International symposium on the dynamics of marine vehicles and structures in waves, London, 1974

[9] K. Herfjord et al: *"FSI-simulations of vortex induced vibration of offshore structures"*, Computational Methods for Fluid-Structure Interaction (editors: T. Kvamsdal et al), Tapir Akademisk Forlag, 2000

[10] R. H. J. Willden, J. M. R. Graham: *"Numerical prediction of VIV on long flexible circular cylinders"*, Journal of Fluids and Structures, vol. 15, pp. 659-669, 2001

[11] http://www.notur.no, homepage of NOTUR, the Norwegian High Performance Computing Consortium

[12] F.M. White: *"Viscous fluid flow"*, Second edition, McGraw-Hill International Editions, 1991

[13] F.M. White: *"Fluid mechanics"*, Fourth Edition, McGraw-Hill International Editions, 1999

[14] H. Schlichting: *"Boundary-Layer Theory"*, 7th Edition, McGraw-Hill, 1979

[15] J.F. Wendt (Ed.): *"Computational Fluid Dynamics -An Introduction"*, 2nd Edition, Springer Verlag, 1996

[16] H. Melbø, T. Kvamsdal: *"Goal oriented error estimators for Stokes equations based on variationally consistent postprocessing"*, Computational methods in applied mechanics and engineering, Vol. 192, pp. 613-633, 2003

[17] J.D. Anderson: *"A history of aerodynamics (and its impact on flying machines)"*, Cambridge University Press, 1997

[18] J.C. Tannehill, D.A. Anderson, R.H. Pletcher: *"Computational Fluid Mechanichs and Heat Transfer"*, Second ed., Taylor & Francis, 1997

[19] R.L. Panton: *"Incompressible flow"*, Second edition, John Wiley & Sons Inc., 1996

[20] A.J. Chorin: *"A Numerical Method for Solving Incompressible Viscous flow Problems"*, Journal of Computational Physics, Vol. 2, pp. 12-26, 1967

[21] T.J.R. Hughes, W.K. Liu, A. Brooks: *"Finite Element Analysis of Incompressible Viscous Flows by the Penalty Function Method"*, Journal of Computational Physics, Vol. 30, pp 1-60, 1979

[22] A.J. Chorin: *"Numerical Solution of the Navier-Stokes equations"*, Mathematics of Computation, Vol. 22, pp. 742-762, 1968

[23] K. Sørli: *"Introduction to Grid Generation"*, Lecture notes, SINTEF Applied Mathematics, 2002

[24] W. Cheney, D. Kincaid: *"Numerical Mathematics and Computing"*, 4th edition, Brooks/Cole Publishing Company, 1999

[25] H.K. Versteeg, W. Malalasekera: *"An Introduction to Computational Fluid Dynamics - The Finite Volume Method"*, Longman Group Ltd., 1995

[26] J.H. Ferziger, M. Peric: *"Computational Methods for Fluid Dynamics"*, 3rd edition, Springer Verlag, 2002

[27] O.C. Zienkiewicz, R.L. Taylor: *"The Finite Element Method - Volume 3: Fluid Dynamics"*, 5th edition, Butterworth-Heinemann, 2000

[28] P.M. Gresho, R.L. Sani: *"Incompressible Flow and the Finite Element Method"*, John Wiley & Sons Ltd., 1998

[29] G.E. Karniadakis, S.J. Sherwin: *"Spectral/hp element methods for CFD"*, Oxford University Press, 1999

[30] R. Löhner: *"Applied CFD Techniques - An Introduction Based on Finite Element Methods"*, John Wiley & Sons Ltd, 2001

[31] D. Greenspan, V. Casulli: *"Numerical analysis for applied mathematics, science and engineering"*, Addison-Wesley Publishing Company, Inc., 1988

[32] H.P. Langtangen: *"Computational Partial Differential Equations - Numerical Methods and Diffpack Programming"*, 2nd ed., Vol. 1, Springer-Verlag, 2003

[33] http://www.notur.no, homepage of NOTUR, the Norwegian High Performance Computing Consortium

[34] A.J. Chorin: *"Numerical solution of the Navier-Stokes equations"*, Mathematics of Computation, Vol. 22, pp. 742-762, 1968

[35] P.M. Gresho, R.L. Sani: *"Incompressible Flow and the Finite Element Method"*, John Wiley & Sons Ltd., 1998

[36] J. Holmen: *"CPM v.2.5 - Continous Projection Method"*, SINTEF Applied Mathematics, 2002

[37] C.H.K. Williamson: *"The existence of two stages in the transition to three-dimensionality of a cylinder wake"*, Phys. Fluids, vol. 31, pp. 3165-3168, 1988

[38] D. Barkley, R.D. Henderson: *" Three-dimensional Floquet stability analysis of the wake of a circular cylinder"*, J. Fluid Mech., vol. 322, pp. 215-241, 1996

[39] R.D. Henderson: *"Nonlinear dynamics and pattern formation in turbulent wake transition"*, J. Fluid Mech., vol. 352, pp. 65-112, 1997

[40] C.H.K. Williamson: *"Vortex dynamics in the cylinder wake"*, Annu. Rev. Fluid Mech., vol 28, pp. 477-539, 1996

[41] S.B. Pope: *"Turbulent Flows"*, Cambridge University Press, 2000

[42] K. Sørli: *"Griddler - A Modeler for Multidimensional Fields in Complex Geometries (Version 1.1 User's Guide)"*, SINTEF Applied Mathematics, 2003

[43] A.G. Kravchenko, P. Moin: *"Numerical studies of flow over a circular cylinder at Re_D = 3900"*, Phys. Fluids, vol. 12, pp. 403-417, 2000

[44] F. Tremblay et al: *"LES of flow around a circular cylinder at a subcritical Reynolds number with cartesian grids"*, Advances in LES of Complex Flows, pp. 133-150, Kluwer Academic Publishers, 2002

[45] L.M. Lourenco, C. Shih: *"Characteristics of of the plane turbulent near wake of a circular cylinder. A particle image velocimetry study"*, 1993 (unpublished, results cited in [43], [44])

[46] L. Ong, J. Wallace: *"The velocity field of the turbulent very near wake of a circular cylinder"*, J. Fluid Mech., vol. 20, p. 441, 1996

[47] M.M. Zdravkovich: *"Flow Around Circular Cylinders - Vol. 2: Applications"*, Oxford University Press, 2003

[48] T. Igarashi: *"Characteristics of the Flow around Two Circular Cylinders Arranged in Tandem (1st Report)"*, Bulletin of the JSME, Vol. 24, No. 188, 1981

[49] M.B. Bryndum, H. Andersen: *"Norwegian Deepwater Programme: 2D Model Testing of Risers"*, Vol. 1, 1999 (Confidential)

[50] S.R. Ransau: 2D simulation of flow around cylinders in tandem (Private communication)

[51] S.H. Rhee, T. Hino: *"Computational Investigation of 3D Turbulent Flow Separation around a Spheroid using an Unstructured grid Method"*, Journal of The Society of Naval Architects of Japan, Vol. 188, 2000

[52] G.S. Constantinescu et al: *"Numerical Investigation of Flow past a Prolate Spheroid"*, AIAA paper 2002-0588

[53] T.A. Johnson, V.C. Patel: *"Flow past a sphere up to a Reynolds number of 300"*, J. Fluid Mech, vol. 378, pp. 19-70, 1999

Appendix A

Drag and lift, single cylinder

A.1 $Re = 265$, $L = 0.822d$

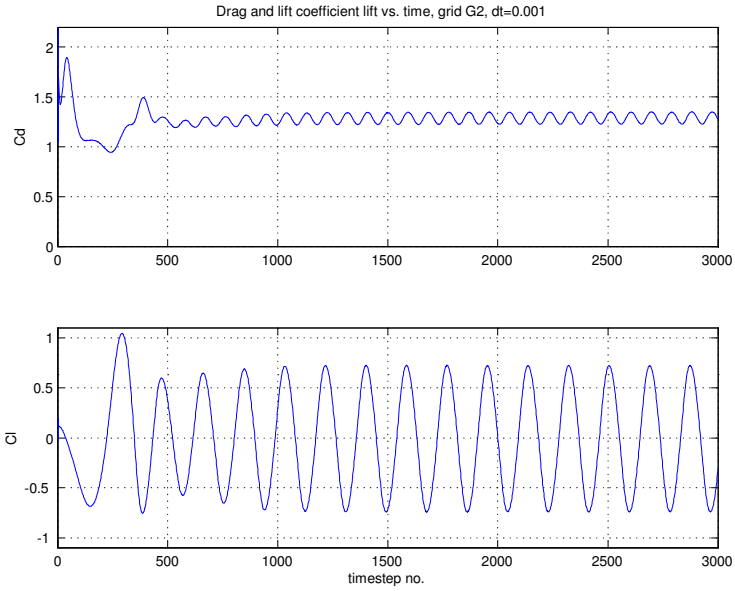

Drag and lift coefficient, grid G2, $\delta t = 0.001$.

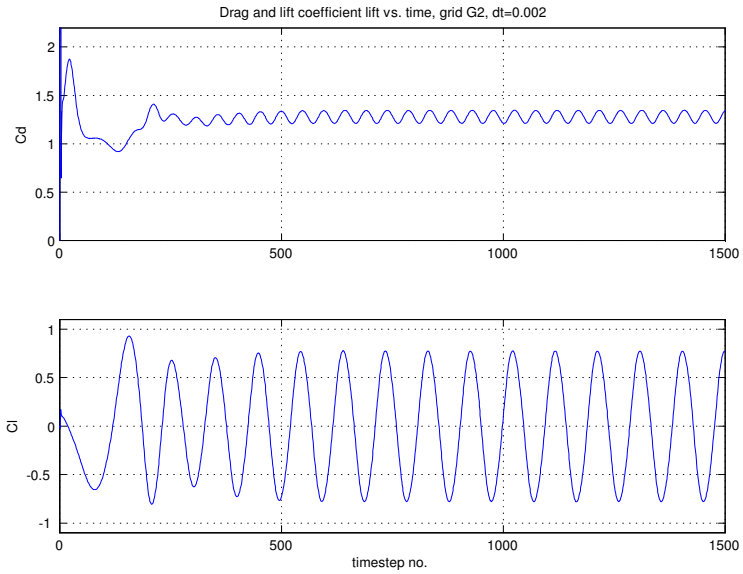

Drag and lift coefficient, grid G2, $\delta t = 0.002$.

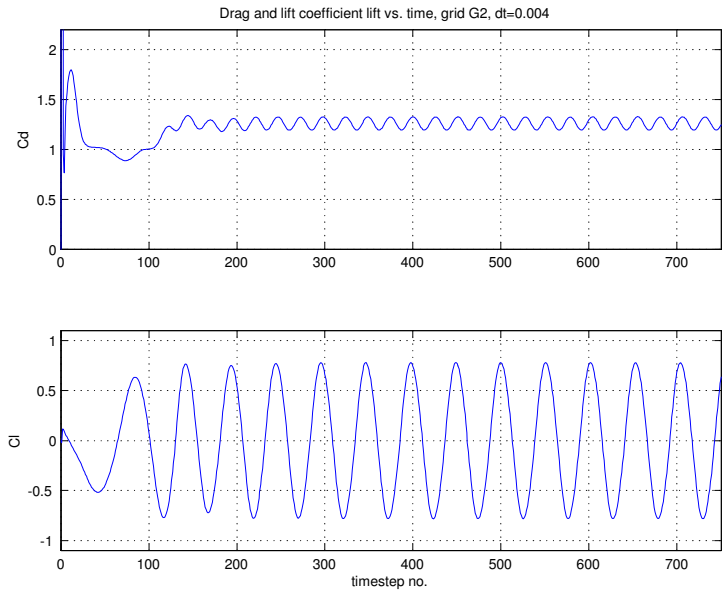

Drag and lift coefficient, grid G2, $\delta t = 0.004$.

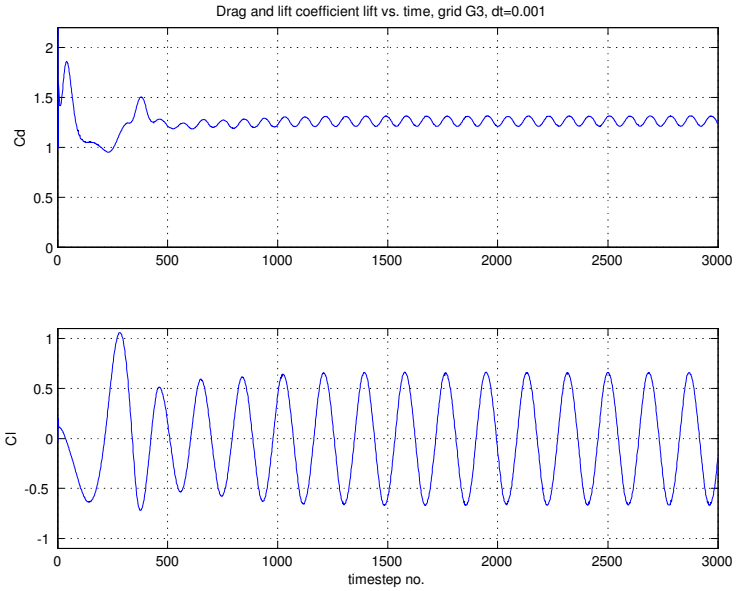

Drag and lift coefficient, grid G3, $\delta t = 0.001$.

A.2 $Re = 3900$, $L = 3.288d$

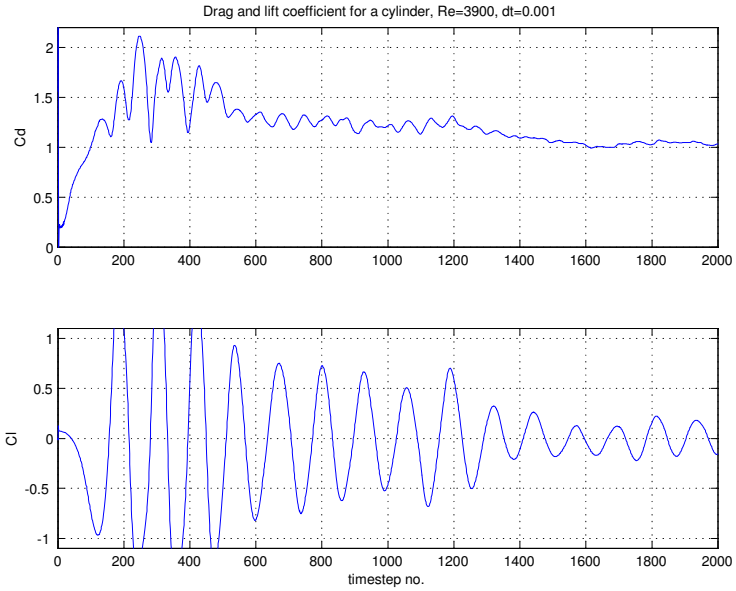

Drag and lift coefficient, backward Euler with van Driest wall damping (Case 2).

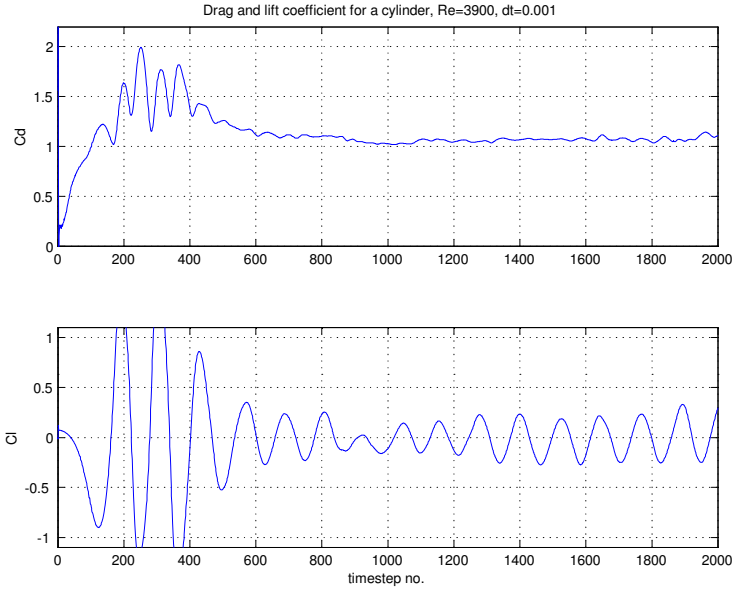

Drag and lift coefficient, backward Euler without wall damping (Case 3).

Appendix B

Drag and lift, two cylinders in tandem

B.1 $Re = 21600,\ S/d = 5,\ T/d = 0$

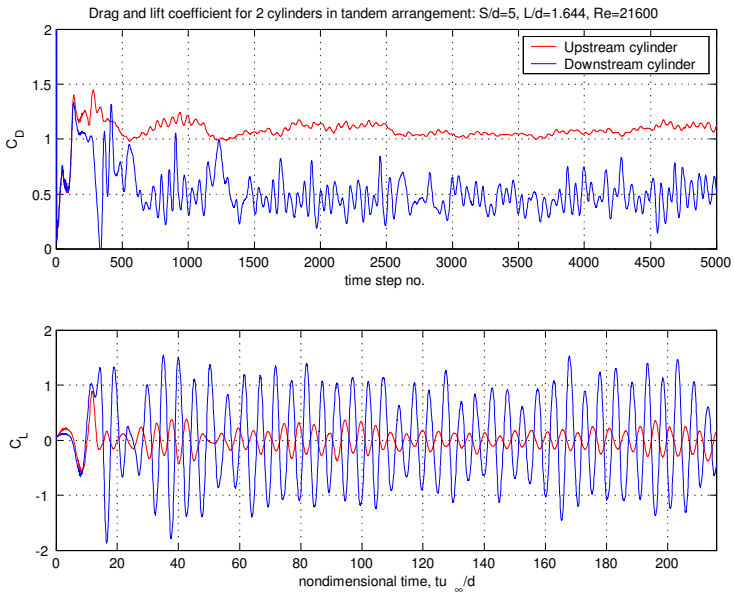

LES results: Time series of drag and lift, case MC (L/d=1.644)

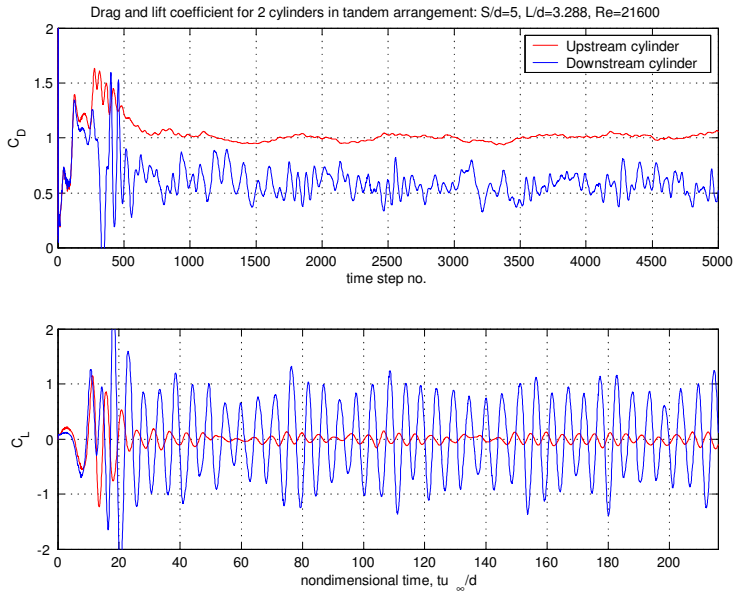

LES results: Time series of drag and lift, case LC (L/d=3.288)

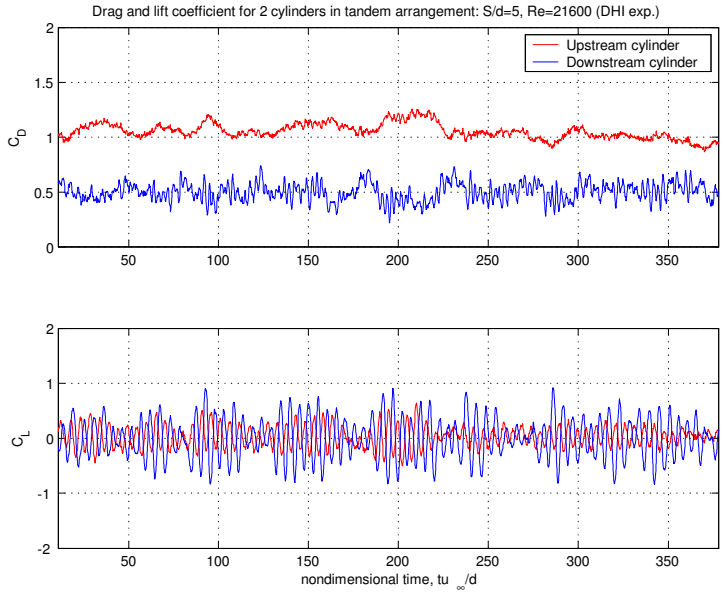

Experimental data, DHI: Time series of drag and lift